UNIVERSITY COLLEGE CORK

Techniques for Engineering Quantum States

by

Tadhg Morgan

A thesis submitted in partial fulfillment for the
degree of Doctor of Philosophy

in the
Faculty of Science
Department of Physics

November 2013

Declaration of Authorship

I, Tadhg Morgan, declare that this thesis titled, 'Techniques for Engineering Quantum States', and the work presented in it are my own. I confirm that:

- This work was done wholly or mainly while in candidature for a research degree at this University.
- Where any part of this thesis has previously been submitted for a degree or any other qualification at this University or any other institution, this has been clearly stated.
- Where I have consulted the published work of others, this is always clearly attributed.
- Where I have quoted from the work of others, the source is always given. With the exception of such quotations, this thesis is entirely my own work.
- I have acknowledged all main sources of help.
- Where the thesis is based on work done by myself jointly with others, I have made clear exactly what was done by others and what I have contributed myself.

Signed: _____

Date: _____

External Examiner
Dr. Simon Gardiner - University of Durham, United Kingdom

Internal Examiner
Dr. Emanuele Pelucchi - University College Cork, Ireland

Principle Supervisor
Prof. Thomas Busch - Okinawa Institute of Science and Technology, Japan

Secondary Supervisor
Prof. Stephen Fahy - University College Cork, Ireland

Eochair feasa foghlaim.

Seanfhocal

UNIVERSITY COLLEGE CORK

Abstract

Faculty of Science
Department of Physics

Doctor of Philosophy

by Tadhg Morgan

In this thesis I theoretically study quantum states of ultracold atoms. The majority of the Chapters focus on engineering specific quantum states of single atoms with high fidelity in experimentally realistic systems. In the sixth Chapter, I investigate the stability and dynamics of new multidimensional solitonic states that can be created in inhomogeneous atomic Bose-Einstein condensates.

The Chapters in this thesis are the papers produced over the course of my Ph.D. In the third Chapter of this thesis I present two papers in which I demonstrate how the coherent tunnelling by adiabatic passage (CTAP) process can be implemented in an experimentally realistic atom chip system, to coherently transfer the centre-of-mass of a single atom between two spatially distinct magnetic waveguides. In these works I also utilise GPU (Graphics Processing Unit) computing which offers a significant performance increase in the numerical simulation of the Schrödinger equation.

In the fourth Chapter I investigate the CTAP process for a linear arrangement of radio frequency traps where the centre-of-mass of both, single atoms and clouds of interacting atoms, can be coherently controlled. In Chapter five I present a theoretical study of adiabatic radio frequency potentials where I use Floquet theory to more accurately model situations where frequencies are close and/or field amplitudes are large. I also show how one can create highly versatile 2D adiabatic radio frequency potentials using multiple radio frequency fields with arbitrary field orientation and demonstrate their utility by simulating the creation of ring vortex solitons.

In the sixth Chapter I discuss the stability and dynamics of a family of multidimensional solitonic states created in a harmonically confined Bose-Einstein condensate. I demonstrate that these solitonic states have very interesting dynamical instabilities, where a continuous collapse and revival of the initial state occurs. Through Bogoliubov analysis, I determine the modes responsible for the observed instabilities of each solitonic state. From each mode, I also extract information related to the time at which instability can be observed.

Acknowledgements

First and foremost, I want to thank my parents for all their help and support throughout my years of study. Without them I would never have been able to undertake, or complete, a Ph.D. This thesis is dedicated to them.

I am extremely grateful and fortunate to have worked with my supervisor, Thomas Busch, from whom I received constant advice and guidance. I am also equally grateful to the members of the Ultra Cold Quantum Gases group, both past and present. In particular I have to thank Nico, Tara and Brian for mornings of scones and Mossy, Steve and Lee for nights of Nicolas Cage. I also want to thank Dave Rea for keeping the spirit of the group alive in room 202 and for many helpful discussions of both physics and philosophy.

Finally I want to thank Kate for getting me through these tough final months. You kept this physicist sane!

Contents

Chapter 1

Introduction

1.1 Background

The purpose of physics is to the describe the natural world. As such, the length scales which physics covers ranges from the massive, with astronomical phenomena such as black holes and supernovae, to the microscopic realm of single atoms and fundamental particles. It is for the description of the amazing physics observed at these atomic and sub-atomic length scales that quantum mechanics was initially developed.

Experimental progress in the observation of quantum phenomena was very difficult for many decades and the only observable and controllable quantum effects were the ones that manifested themselves on macroscopic scales, such as in solid state transistors or superconductors. The realisation of systems where quantum effects of single particles could be observed required a significant leap in experimental techniques with the pioneering combination of laser cooling and atomic trapping.

With the advent of laser cooling in laboratories around the world, atoms can be cooled to very low temperatures where magnetic and optical potentials can then be used to trap them so that single and few particle systems can be studied. Such techniques can be applied to a dilute gas of bosons where, due to Bose-Einstein statistics, they begin to macroscopically occupy the lowest single-particle state at finite temperature. This effect is called Bose-Einstein condensation and the resulting state of matter is called a Bose-Einstein condensate (BEC).

A BEC provides us with a system in which we can study quantum mechanics at mesoscopic scales and was first observed in 1995 when a cloud of ^{87}Rb atoms was laser cooled, confined by magnetic fields and then evaporatively cooled [1]. In 2001, the Nobel Prize for physics was award to E. Cornell, C. Wieman and W. Ketterle “For the achievement

of Bose-Einstein condensation in dilute gases of alkali atoms, and for early fundamental studies of the properties of the condensates". By today, we have even extended our reach to controlling the quantum states of single neutral atoms as demonstrated by the groups of I. Bloch and M. Greiner, where they can actually image and address individual cold, neutral atoms [2–4]. Similar progress has also been made in the area of cold ions [5].

Quantum mechanics is not only extending our understanding of the physical properties of our world, but is also becoming increasingly important in many engineering fields, where devices are fabricated on smaller and smaller length scales. This is most clearly highlighted by Moore's Law [6] which states that the number of transistors on integrated circuits doubles every 18 months. This ongoing trend to continuously miniaturise and integrate many technologies brings engineering closer and closer to the boundaries of the quantum world. Today, consumer CPUs (central processing unit) are manufactured using 22nm node technology, which means that half the distance between identical features in an array is 22nm. It is predicted that by 2017, CPUs will be manufactured using 10nm node technology where quantum effects will begin to play an important role [7]. The ultimate limit of Moore's Law is where a transistor will be made of a single atom, a purely quantum device. Amazingly, such a device has already been created [8].

While initially it appears that engineering at these length scales would make things much more complicated and harder to handle, working with such quantum devices will allow us to exploit the laws of quantum mechanics to create many amazing new technologies. Numerous such devices have already been proposed, the most famous of which is the quantum computer which has the potential to revolutionise computing [9]. In fact, we are already beginning to see the first signs of the shift to quantum technologies with companies offering commercial quantum key distribution [10, 11] and quantum annealing machines [12].

Cold atoms have been a precursor for many of these technologies as they provide clean, controllable systems which can be used as testbeds for quantum engineering. In particular, the engineering of the internal degrees of freedom of cold atoms has been one of the most successful fields of research, a fact highlighted by the awarding of the 2012 Nobel Prize for Physics to Serge Haroche and David J. Wineland "For ground-breaking experimental methods that enable measuring and manipulation of individual quantum systems". Highlights of their work include: non-destructive measurements of quantum states [13], good coupling between light and matter [14], long coherence times of trapped quantum states [14] and the creation of a CNOT gate with trapped ions [15].

It is on this area of engineering quantum states that this thesis focuses. Through the collections of works in this thesis, we aim to contribute to this field through three distinct avenues of research: new techniques for coherent control of quantum states in

realistic potentials, applications and improved theoretical descriptions of adiabatic radio frequency potentials and the study of phase engineered BECs to create novel solitonic states. In the following Sections of this Chapter, we will motivate each of these works separately.

1.2 Coherent Tunnelling by Adiabatic Passage on Atom Chips

As mentioned in the previous Section, the control of the internal degrees of freedom of quantum states is an advanced field [16]. However, control over external degrees of freedom has not received as much attention. As such, developing techniques to coherently control the external degrees of freedom at the same level as the internal ones is highly desirable. In particular, the development of techniques that would allow us to engineer the centre-of-mass of quantum states with high fidelity would be a significant advancement.

Implementing such techniques using cold atoms is a natural choice as trapping potentials can be made deep enough so that one can confine atoms with very low energies. As such, this already gives us good control over the stationary centre-of-mass. The challenge is now to find techniques to coherently transport these stationary centre-of-mass states with high fidelities. Many of the known techniques suffer drawbacks such as introducing unwanted heating effects stemming from an increased kinetic energy when the atom is moved through space. Other proposed techniques require direct coupling between two trapped states which has advantages in terms of the tunnelling coupling being a coherent process. However, tunnelling is exponentially sensitive to many of the system's parameters such as the position of the traps, strength of the trapping fields and the timing of the process. This makes the fidelity of the centre-of-mass transport sensitive to slight changes in the system parameters.

Both of these situations are far from ideal for many quantum operations one would like to perform such as quantum computing [17]. An instructive example is quantum computing with spatial qubits [18], where the computational basis states are defined by the presence of a neutral atom in the ground state of one out of two trapping potentials. When transferring an atom between the trapped states by direct tunnelling, slight variations in the systems parameters would lead to incomplete transfer to the target state. For spatial qubits, this would lead to errors and high computational overheads associated with error correction schemes.

Other suggestions for quantum computing architectures require the transport of atoms that are initially spatially well separated, such that they can be made interact directly with each other. In particular, in [19] it was suggested that optical tweezers could be used to transport atoms confined in an optical lattice. However, such techniques add unwanted heat to the system and again error correction must be performed to meet the requirements for fault-tolerant, scalable quantum computing.

Ideally, we desire a technique that offers high fidelity, does not heat, and allows the relaxation of many of the control requirements. One such family of techniques that can achieve are the so called adiabatic techniques, which allow to follow a single eigenstate throughout the process, thus avoiding influence from unwanted states. Therefore, adiabatic techniques can be extremely robust to experimental errors and noise. However, there is a price to pay as adiabatic following usually requires the system to change very slowly, which increases the overall time needed for the process. This increase has to be weighed against the time and overhead needed for error correction to decide if the use of adiabatic techniques to achieve a certain task is a viable option. However, the latter is not of any concern for the work presented in this thesis, which deals only with the questions of experimental observability.

In particular, a very promising adiabatic technique for controlling the quantised centre-of-mass state is coherent tunnelling by adiabatic passage (CTAP) [20]. The motivation behind CTAP is the removal of time dependence from the fidelity of transferring an atom from one trap to another via tunnelling. This time dependence is seen if one considers an atom confined to one of two traps which are initially well separated. By then decreasing the distance between two traps, the tunnel coupling increases exponentially which causes the atom to begin to tunnel from the initial trap to the target trap. However, as soon as the atom tunnels to the target trap it begins to tunnel back to the initial trap. This tunnelling dynamic, which will be detailed in Section 2.5.1, results in so-called Rabi oscillations of the centre-of-mass of the atom between the two traps which leads to the transfer fidelity being dependent on the total time of the process (the time at which the oscillations stop). We will show in Section 2.5.2, that by introducing a third, intermediate trap, the CTAP process provides us with a method of transitioning between two trapped states without any unwanted Rabi oscillations. In this way, the transfer fidelity to the target trap for CTAP is time-independent (provided the process is adiabatic) and robust to variations in system parameters [21].

While the CTAP process has had extensive theoretical study [20–24], experimental implementation of the scheme is not straightforward. In many realistic types of trapping potentials, bringing individual traps together, which is essential for CTAP, causes them to influence one another. This influence results in a modification to the overall geometry

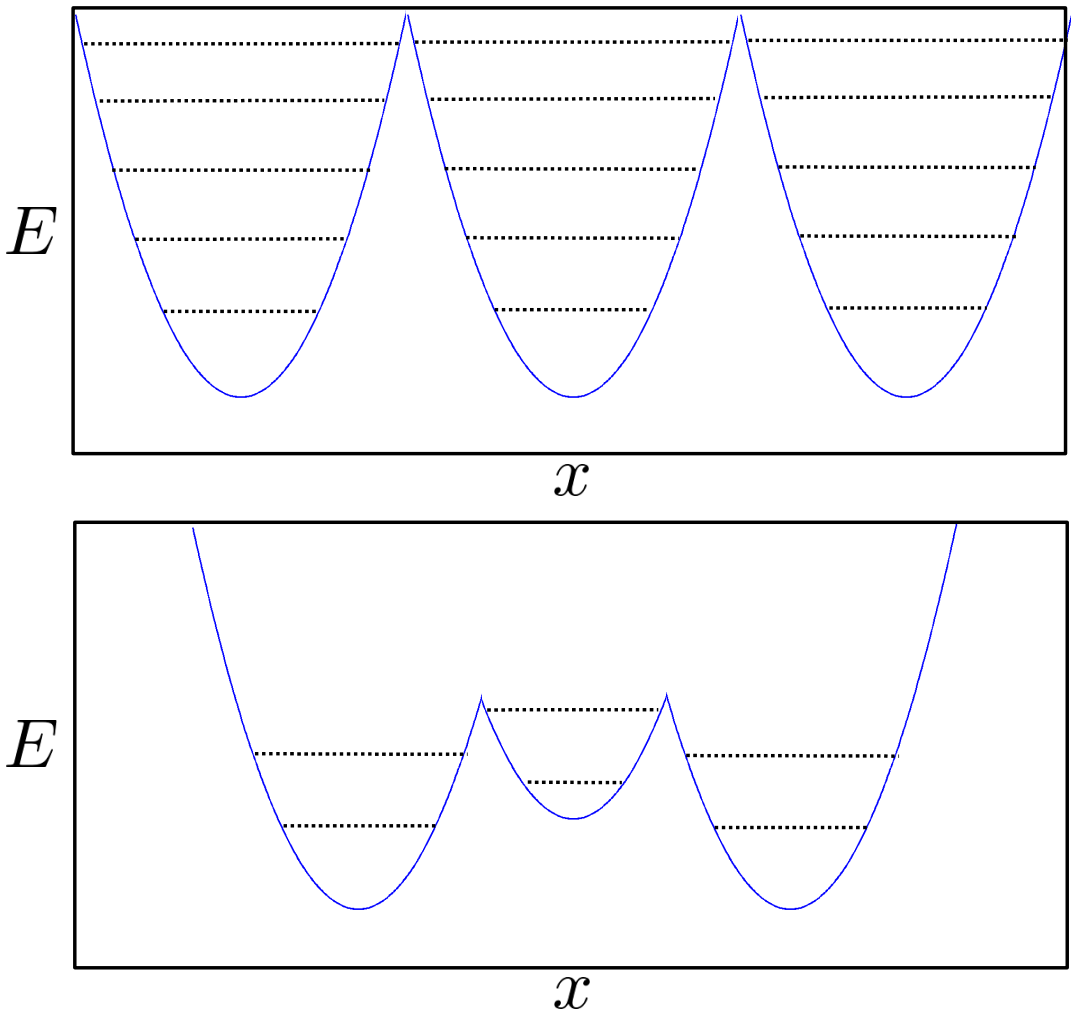

FIGURE 1.1: Schematic of the influence that previously resonant traps will have on each other when the distance between them in decreased. The black dashed lines represent the energy levels of the traps.

of the individual traps, which in turn changes their individual energy level structures. A schematic of this influence is shown in Fig. 1.1. This is further complicated when one considers that the positions of the traps are changed in a time-dependent fashion, therefore producing a time-dependent energy level structure. This is one of the largest problems facing the experimental realisation of the CTAP process as one of the requirement of the process is that the traps be resonant at all points in time.

While this resonance condition is important, the CTAP process can be successfully implemented with an approximate resonance, where high fidelity transfer can be assured for small detunings between the traps by increasing the adiabaticity of the process [21]. However, if the traps of a system significantly influence each other, the modification to the energy level structure will be too large to compensate for, and so violate the resonance condition. Indeed in [21] it was suggested that a system of optical waveguides would be a

good system for CTAP, but neighbouring optical waveguides have a significant effect on each other leading to non-negligible modification of the trapping potential. It is for this reason that almost all treatments assume unrealistic, piece-wise harmonic traps which do not influence each other and therefore remain in resonance at all times.

In this thesis we present two experimentally realistic systems in which we can compensate for the influence individual trapping potentials exert on each other and achieve approximate resonance. We then show that this is sufficient for the observation of CTAP. The two systems we suggest are atomic waveguides on atom chips and radio frequency traps. Both are well known experimental tools and are widely used in many experimental labs around the world today [25, 26].

In Chapter 3 we present two manuscripts in which we give a detailed treatment of an atom chip as a good candidate for an experimental system in which to implement CTAP with cold atoms. The focus of the first manuscript is the simulation of the atom chip system in two dimensions (2D) where the dispersion along the atom chip is neglected. In the second manuscript we then extend this work to simulating the CTAP process in a three dimensional (3D) atom chip system. These simulations take the complete spatial dynamics in all three dimensions into account.

1.3 Adiabatic Radio Frequency Potentials

Chapters 4 and 5 of this thesis focus on adiabatic radio frequency (rf) potentials as a tool for engineering quantum states. Radio frequency traps can be made in conjunction with atom chips and have recently become one of the most versatile tools for trapping cold atoms [27, 28]. When used in combination with the static trapping fields created on atom chips, they offer a way of changing the trapping geometry [26]. This makes them a promising candidate for engineering quantum states and, as we show in Chapter 4, offer another experimentally realistic system in which the CTAP process can be observed. We also show that the described rf system can be adjusted to use the CTAP process to coherently control a cloud of interacting atoms.

In dealing with an atom interacting with oscillating fields, such as an rf field, the theoretical treatment often relies on approximations to obtain information about the quantum state of the atom. In Chapter 4 we make three main approximations to obtain the adiabatic rf potential for the atom. First, we consider a purely one dimensional system by assuming the rf always oscillates in a direction orthogonal to the static (trapping) field. Second, we move to a rotating frame and make the rotating wave approximation by neglecting fast oscillating terms in the Hamiltonian. Finally, in order to deal with

multiple frequencies, we make a local frequency approximation where the potential at any point is governed by the frequency closest to resonance and the effect of all other frequencies is summed up as an effective Stark shift [29].

While our theoretical approach is appropriate for the system we deal with in Chapter 4, in Chapter 5 we extend the theory of adiabatic rf potentials past these approximations. To do this we turn to Floquet theory. Floquet theory, developed by Gaston Floquet [30], allows us to take a time-dependent, periodic, Hamiltonian and represent it as an infinite matrix [31]. The eigenvalues of this matrix produce an eigenenergy spectrum, from which the adiabatic rf potential can be extracted.

With this Floquet approach for generating adiabatic rf potentials, many new types of systems can be described. We can accurately describe situations where frequencies are very close together or have large Rabi frequencies, which are regimes where the piecewise resonance model of Chapter 4 breaks down. We can also create 2D adiabatic potentials using multiple rf fields with different frequencies and arbitrary field orientation. We show that these 2D potentials are highly controllable as we can adjust the frequency separation, amplitude and orientation of the rf fields independently from one another.

As a demonstration of their utility, we use our Floquet approach to examine a particular type of 2D adiabatic rf potential that allows us to create and examine ring vortex solitons. The stability of ring vortex solitons was investigated recently [32] but no suggestion was made about how to create these states. We propose that our 2D adiabatic rf potential would be a good candidate for an experimentally realistic system in which we can create and study these states and we demonstrate this by carrying out numerical simulations.

1.4 Solitons

While up to now we have mainly concentrated on describing quantum states of single particles, in Chapter 6 we discuss a phenomenon observable in a mesoscopic sample of ultracold atoms. In particular, we focus on describing the stability properties of novel, multidimensional solitonic states in a BEC.

BECs of neutral atoms provide very clean and controllable systems for studying many physical effects. Due to the interactions between the atoms, these systems are inherently non-linear, and the degree of this property can be experimentally controlled by using Feshbach resonances. One interesting class of possible non-linear excitations in these systems are so-called solitons. A soliton is a localised wavepacket that can propagate without dispersion due to a balance between non-linear and dispersive effect and emerge unchanged from a collision with another soliton (except for a phase shift).

Solitons occur in many different physical systems [33]. In particular, they have been widely studied in non-linear optics [34] and classical systems such as hydrodynamics [35]. In contrast, matter wave solitons which are created in purely quantum systems, are comparatively underdeveloped but have many possible applications such as interferometry [36], quantum entanglement [37] and quantum information processing [38].

Until now, much of the work done on matter wave solitons has concentrated on single solitons and soliton-soliton collisions [39]. However, due to the known instabilities in higher dimensions, such as the snake instability in 2D and ring vortex solitons in 3D, much of this work has been limited to 1D and quasi 1D (ring) [40, 41].

In Chapter 6, we discuss matter wave structures that are inherently two-dimensional. In this higher dimensionality, we can engineer the phase of BECs to create novel solitonic states in which several solitons overlay and intersect each other at different angles. We show that these multidimensional solitons exhibit interesting stability and dynamical properties. By using the Bogoliubov-de Gennes equation, we uncover unstable modes and demonstrate that they are responsible for the instability of our solitonic states and also predict the time at which the instability occurs.

Chapter 2

Background Theory

In this Chapter, we will summarise the theory of a Bose gas at low temperature as it is the common background system for all works presented in this thesis. After this we will outline the core, theoretical, ideas of the papers contained in this thesis.

2.1 Bose-Einstein Condensates

To review the theory of an ideal Bose gas we will follow the treatment in [42] and [43]. This Section is by no means comprehensive, but instead gives a broad overview of the formalism and relevant formulae.

Let us start by describing an ideal Bose gas in the grand canonical ensemble. The average occupation number for each of the single-particle states is given by the Bose distribution function and can be written as

$$\bar{n}_i = \frac{1}{e^{\beta(\epsilon_i - \mu)} - 1} \ , \tag{2.1}$$

where μ is the chemical potential of the gas, the ϵ_i are the single-particle eigenenergies and $\beta = \frac{1}{k_B T}$, where k_B is the Boltzmann constant and T is the temperature. The inclusion of the chemical potential μ in this Bose distribution ensures that the total number of particles N,

$$N = \sum \bar{n}_i \ , \tag{2.2}$$

is conserved.

For a Bose gas, an important physical constraint is that the chemical potential μ, may not exceed the lowest single particle eigenenergy ϵ_0. If this were not the case, eq. (2.1)

would give a negative value for the occupation of states with energy smaller than μ. This is, of course, non-physical.

At high temperatures the chemical potential is much less than the eigenenergy of the lowest occupied eigenstate, ϵ_{min}. In this regime, the mean occupation of any state is much less than 1. However, when $\mu \to \epsilon_0$, the occupation of the lowest energy state $N_0 = \frac{1}{e^{\beta(\epsilon_0-\mu)}-1}$ becomes very large and one can write the total number of particles as the sum of the occupation of the lowest energy state $N_0 = \frac{1}{e^{\beta(\epsilon_0-\mu)}-1}$ and the occupation of all other states N_T

$$N = N_0 + N_T \ , \tag{2.3}$$

where $N_T = \sum_{i\neq 0} \bar{n}_i(T)$ is referred to as the thermal component of the gas.

We can now define the critical temperature T_c as the temperature above which the thermal component of the gas dominates and N_0 is negligible,

$$N_T(T_c) = N \ . \tag{2.4}$$

Below this critical temperature the value of μ will approach ϵ_0 in the thermodynamic limit (large N). Therefore, for temperatures lower that T_c, N_0 dominates and we get macroscopic occupation of the lowest single particle state of eigenenergy ϵ_0. This effect is known as Bose-Einstein condensation.

To develop the mathematical formalism to describe the state of a Bose-Einstein Condensate (BEC), our approach is to write down the Hamiltonian of an ideal Bose gas in terms of the field operators $\hat{\Psi}(\mathbf{r})$. First, suppose there are n_α bosons in the single particle eigenstate α. We choose to denote this state $|n_\alpha\rangle$ and define $\hat{a}^\dagger_\alpha$ and $\hat{a}_\alpha$ as the creation and annihilation operators of a boson in the single particle eigenstate α,

$$\begin{aligned} \hat{a}^\dagger_\alpha |n_0, n_1, n_2, ..., n_\alpha, ...\rangle &= \sqrt{n_\alpha + 1}|n_0, n_1, n_2, ..., n_\alpha + 1, ...\rangle \ , \\ \hat{a}_\alpha |n_0, n_1, n_2, ..., n_\alpha, ...\rangle &= \sqrt{n_\alpha}|n_0, n_1, n_2, ..., n_\alpha - 1, ...\rangle \ , \end{aligned} \tag{2.5}$$

such that they satisfy the bosonic commutation relations

$$\begin{aligned} \left[\hat{a}_\alpha, \hat{a}^\dagger_\beta\right] &= \delta_{\alpha,\beta} \\ \left[\hat{a}^\dagger_\alpha, \hat{a}^\dagger_\beta\right] &= [\hat{a}_\alpha, \hat{a}_\beta] = 0 \ . \end{aligned} \tag{2.6}$$

The operators $\hat{a}_\alpha^\dagger$ and $\hat{a}_\alpha$ are now used to define the field operators,

$$\begin{aligned}\hat{\Psi}^\dagger(\mathbf{r}) &= \sum_{\alpha=0} \Psi_\alpha(\mathbf{r})\hat{a}_\alpha^\dagger \ , \\ \hat{\Psi}(\mathbf{r}) &= \sum_{\alpha=0} \Psi_\alpha(\mathbf{r})\hat{a}_\alpha \ ,\end{aligned} \tag{2.7}$$

where $\Psi_\alpha(\mathbf{r})$ is the wave function of the single particle state α. With the use of eqs. (2.6) it can be shown that these field operators satisfy the following commutation rules,

$$\begin{aligned}\left[\hat{\Psi}(\mathbf{r}'), \hat{\Psi}^\dagger(\mathbf{r})\right] &= \delta(\mathbf{r}' - \mathbf{r}) \ , \\ \left[\hat{\Psi}^\dagger(\mathbf{r}'), \hat{\Psi}^\dagger(\mathbf{r})\right] &= \left[\hat{\Psi}(\mathbf{r}'), \hat{\Psi}(\mathbf{r})\right] = 0 \ .\end{aligned} \tag{2.8}$$

This allows one to write the Hamiltonian of an ideal Bose gas in terms of these field operators as

$$\hat{H} = \int \left(\frac{\hbar^2}{2m} \nabla\hat{\Psi}^\dagger(\mathbf{r}) \nabla\hat{\Psi}(\mathbf{r}) + V_{ext}(\mathbf{r})\hat{\Psi}^\dagger(\mathbf{r})\hat{\Psi}(\mathbf{r}) \right) d\mathbf{r} \ , \tag{2.9}$$

where m is the mass of the boson and V_{ext} is the external potential.

The formalism thus far has dealt with an ideal Bose gas where the individual particles of the gas do not interact. However, this idealised model is not sufficient for a real Bose gas where interaction plays a vital role in its properties. As such, the Hamiltonian (2.9) must be extended with an extra term which accounts for interaction between the bosons. As the Bose gases we consider are dilute, the range of inter-atomic forces is much smaller than the average distance between bosons therefore allowing us to safely neglect all but two-body interactions. This leads to a Hamiltonian of the form

$$\hat{H} = \int \hat{\Psi}^\dagger(\mathbf{r})\hat{H}_0\hat{\Psi}(\mathbf{r})d\mathbf{r} + \frac{1}{2}\int \hat{\Psi}^\dagger(\mathbf{r})\hat{\Psi}^\dagger(\mathbf{r}')V_{int}(\mathbf{r},\mathbf{r}')\hat{\Psi}(\mathbf{r})\hat{\Psi}(\mathbf{r}')d\mathbf{r}d\mathbf{r}' \ , \tag{2.10}$$

where $V_{int}(\mathbf{r},\mathbf{r}')$ is the two-body interaction potential and $\hat{H}_0 = \hbar^2/2m\nabla^2 + V_{ext}$. Furthermore, we can assume that the gas is sufficiently dilute and cold that the atomic interactions are dominated by low energy, two-body, s-wave collisions. As such, the exact form of the two-body interaction potential is not important to describe the macroscopic properties of the gas, but instead the scattering is characterised by the s-wave scattering length, a_s. We therefore can replace the two body interaction potential with a pseudo-potential,

$$V_{int}(\mathbf{r},\mathbf{r}') = g\delta(\mathbf{r}' - \mathbf{r}) \ , \tag{2.11}$$

where $g = 4\pi\hbar^2 a_s/m$. A more detailed description and derivation of the pseudo-potential approximation can be found in [43].

Inserting (2.11) into the Hamiltonian (2.10) and integrating over $\mathbf{r}'$ gives

$$\hat{H} = \int \hat{\Psi}^\dagger(\mathbf{r})\hat{H}_0\hat{\Psi}(\mathbf{r})d\mathbf{r} + \frac{g}{2}\int \hat{\Psi}^\dagger(\mathbf{r})\hat{\Psi}^\dagger(\mathbf{r})\hat{\Psi}(\mathbf{r})\hat{\Psi}(\mathbf{r})d\mathbf{r} \; . \tag{2.12}$$

In the Heisenberg picture the time evolution of the field operators is given by

$$\begin{aligned} i\hbar\frac{\partial}{\partial t}\hat{\Psi}(\mathbf{r}',t) = \left[\hat{\Psi}(\mathbf{r}',t),\hat{H}\right] = \hat{\Psi}(\mathbf{r}',t)\hat{H} - \int \hat{\Psi}^\dagger(\mathbf{r},t)\hat{H}_0\hat{\Psi}(\mathbf{r},t)\hat{\Psi}(\mathbf{r}',t) \\ - \frac{g}{2}\int \hat{\Psi}^\dagger(\mathbf{r},t)\hat{\Psi}^\dagger(\mathbf{r},t)\hat{\Psi}(\mathbf{r},t)\hat{\Psi}(\mathbf{r},t)\hat{\Psi}(\mathbf{r}',t) \; . \end{aligned} \tag{2.13}$$

This equation can be rewritten using the bosonic commutation rules from eq. (2.8) as

$$\begin{aligned} i\hbar\frac{\partial}{\partial t}\hat{\Psi}(\mathbf{r}',t) =& \hat{\Psi}(\mathbf{r}',t)\hat{H} - \int \left[\hat{\Psi}(\mathbf{r}',t)\hat{\Psi}^\dagger(\mathbf{r},t) - \delta(\mathbf{r}'-\mathbf{r})\right]\hat{H}_0\hat{\Psi}(\mathbf{r},t) \\ & - \frac{g}{2}\int \left[\hat{\Psi}(\mathbf{r}',t)\hat{\Psi}^\dagger(\mathbf{r},t) - 2\delta(r'-r)\right]\hat{\Psi}^\dagger(\mathbf{r},t)\hat{\Psi}(\mathbf{r},t)\hat{\Psi}(\mathbf{r},t)d\mathbf{r} \\ =& \hat{\Psi}(\mathbf{r}',t)\hat{H} - \int \hat{\Psi}(\mathbf{r}',t)\hat{\Psi}^\dagger(\mathbf{r},t)\hat{H}_0\hat{\Psi}(\mathbf{r},t) + \int \hat{H}_0\hat{\Psi}(\mathbf{r},t)\delta(\mathbf{r}'-\mathbf{r})d\mathbf{r} \\ & - \frac{g}{2}\int \hat{\Psi}(\mathbf{r}',t)\hat{\Psi}^\dagger(\mathbf{r},t)\hat{\Psi}^\dagger(\mathbf{r},t)\hat{\Psi}(\mathbf{r},t)\hat{\Psi}(\mathbf{r},t)d\mathbf{r} \\ & + g\int \hat{\Psi}^\dagger(\mathbf{r},t)\hat{\Psi}(\mathbf{r},t)\hat{\Psi}(\mathbf{r},t)\delta(\mathbf{r}'-\mathbf{r})d\mathbf{r} \\ =& \int \hat{H}_0\hat{\Psi}(\mathbf{r},t)\delta(\mathbf{r}'-\mathbf{r})d\mathbf{r} + g\int \hat{\Psi}^\dagger(\mathbf{r},t)\hat{\Psi}(\mathbf{r},t)\hat{\Psi}(\mathbf{r},t)\delta(\mathbf{r}'-\mathbf{r})d\mathbf{r} \\ =& \left[\hat{H}_0 + g\hat{\Psi}^\dagger(\mathbf{r}',t)\hat{\Psi}(\mathbf{r}',t)\right]\hat{\Psi}(\mathbf{r}',t) \; . \end{aligned} \tag{2.14}$$

Considering the fact that in a BEC, the lowest single particle eigenstate is macroscopically occupied we make the approximation $n_0 \pm 1 \approx n_0$ and from eq. (2.5) it follows that

$$\hat{a}_0^\dagger = \hat{a}_0 = \sqrt{n_0}. \tag{2.15}$$

The field operator can therefore be approximated using a classical field for the ground state and keeping the quantised character of the (small) thermal and quantum fluctuations around it as

$$\hat{\Psi}(\mathbf{r}',t) = \sqrt{n_0}\psi_0(\mathbf{r}',t) + \delta\hat{\psi}(\mathbf{r}',t) \; . \tag{2.16}$$

If we assume the limit of zero temperature, the majority of all the bosons are in the lowest single particle eigenstate, $n_0 \approx N$. In this case the fluctuation term $\delta\hat{\psi}(\mathbf{r}',t)$ can be neglected such that $\hat{\Psi}(\mathbf{r}',t) \to \sqrt{N}\psi_0(\mathbf{r}',t)$ and equation (2.14) can be written as

$$i\hbar\frac{\partial}{\partial t}\psi_0(\mathbf{r},t) = \left[-\frac{\hbar^2}{2m}\nabla^2 + V_{ext}(\mathbf{r},t) + gN|\psi_0(\mathbf{r},t)|^2\right]\psi_0(\mathbf{r},t) \; , \tag{2.17}$$

where the dash on the spatial variable has been dropped for ease of notation. This is the time-dependent Gross-Pitaeskii equation (GPE) and has the basic form of the Schrödinger equation, but with an added term that is non-linear and stems from the interactions between the bosons of the BEC. This mean field equation is used extensively in this thesis to study the dynamics of interacting BECs and we will make use of it in Chapter 4 and Chapter 6 in particular.

A time-independent version of the GPE can be obtained by considering that, as the wave function evolves in time, it acquires a phase of $e^{-i\mu t/\hbar}$, such that

$$\psi_0(\mathbf{r}, t) = \psi_0(\mathbf{r}) e^{-i\mu t/\hbar} \, . \tag{2.18}$$

Substituting this into the time-dependent GPE (2.17) gives,

$$\mu\psi_0(\mathbf{r}) = -\frac{\hbar^2}{2m}\nabla^2\psi_0(\mathbf{r}) + V(\mathbf{r})\psi_0(\mathbf{r}) + gN|\psi_0(\mathbf{r})|^2\psi_0(\mathbf{r}) \, . \tag{2.19}$$

2.2 Small Scale Excitations: Bogoliubov-de Gennes Equations

In this section we will consider solutions to the GPE (2.17) which represent small amplitude oscillations around the equilibrium state of the system.

As discussed in the previous Section, the fact that at low temperatures, all atoms in a BEC are condensed to the lowest single particle state allows us to replace the field operator $\hat{\Psi}(\mathbf{r}, t)$ with a classical field $\psi_0(\mathbf{r}, t)$. To study small excitations about $\psi_0(\mathbf{r}, t)$, one can consider the state $\Psi(\mathbf{r}, t)$ which includes a small, linear perturbation $\delta\psi(\mathbf{r}, t)$ such that

$$\Psi(\mathbf{r}, t) = \sqrt{N}\psi_0(\mathbf{r}, t) + \delta\psi(\mathbf{r}, t) \, , \tag{2.20}$$

which, following (2.18), can be written as,

$$\Psi(\mathbf{r}, t) = [\sqrt{N}\psi_0(\mathbf{r}) + \delta\psi(\mathbf{r}, t)]e^{-i\mu t/\hbar} \, . \tag{2.21}$$

As we are dealing with small amplitude oscillations, we expect that the excitations will have the form of plane waves with frequency ω_j, such that $\delta\psi(\mathbf{r}, t)$ can be written as,

$$\delta\Psi(\mathbf{r}, t) = \sum_j [u_j(\mathbf{r})e^{-i\omega_j t} + v_j^*(\mathbf{r})e^{i\omega_j t}] \, , \tag{2.22}$$

where the $u_j(\mathbf{r})$ and $v_j(\mathbf{r})$ are complex amplitude functions. To find the j-th solution, we drop the sum from eq.(2.22) and combine with eq.(2.21) to give the following trial wave function,

$$\Psi(\mathbf{r},t) = [\sqrt{N}\psi_0(\mathbf{r}) + u_j(\mathbf{r})e^{-i\omega_j t} + v_j^*(\mathbf{r})e^{i\omega_j t}]e^{-i\mu t/\hbar} \,. \tag{2.23}$$

Substituting this into the field operator representation of the GPE (2.17) we have,

$$\begin{aligned} i\hbar\frac{\partial\Psi(\mathbf{r},t)}{\partial t} =& e^{-i\mu t/\hbar}\left(\mu\sqrt{N}\psi_0(\mathbf{r}) + \sum_j \left[(\mu+\hbar\omega_j)u_j(\mathbf{r})e^{-i\omega_j t} + (\mu-\hbar\omega_j)v_j^*(\mathbf{r})e^{i\omega_j t}\right]\right) \\ =& H_0\Psi(\mathbf{r},t) + g|\Psi(\mathbf{r},t)|^2\Psi(\mathbf{r},t) \,, \end{aligned} \tag{2.24}$$

where $H_0 = -\frac{\hbar^2}{2m}\nabla^2 + V_{\text{ext}}(\mathbf{r},t)$. To evaluate this equation, we begin by expanding the non-linear term of the right hand side of eq.(2.24) in terms of $u_j(\mathbf{r})$ and $v_j(\mathbf{r})$. However, since most of the particles are in ground state by definition, we expect that the excitations will be small and only terms linear in $u_j(\mathbf{r})$ and $v_j(\mathbf{r})$ are important;

$$\begin{aligned} |\Psi(\mathbf{r},t)|^2\Psi(\mathbf{r},t) = e^{-i\mu t/\hbar}\Big\{ & N|\psi_0(\mathbf{r})|^2\left[\sqrt{N}\psi_0(\mathbf{r}) + 2u_j(\mathbf{r})e^{-i\omega_j t} + 2v_j^*(\mathbf{r})e^{i\omega_j t}\right] \\ & + N\psi_0^2(\mathbf{r})\left[u_j^*(\mathbf{r})e^{i\omega_j t} + v_j(\mathbf{r})e^{-i\omega_j t}\right]\Big\} \,. \end{aligned} \tag{2.25}$$

We now have both sides of the GPE expressed in terms of $e^{-i(\mu+n\omega)t/\hbar}$ with $n = [-1, 0, 1]$ and so we equate the powers with equal values of n.

For $n = 0$ we have

$$\mu\psi_0(\mathbf{r}) = H_0\psi_0(\mathbf{r}) + gN|\psi_0(\mathbf{r})|^2\psi_0(\mathbf{r}) \,. \tag{2.26}$$

For $n = 1$ we have

$$(\mu+\hbar\omega_j)u_j(\mathbf{r}) = \left[H_0 + 2gN|\psi_0(\mathbf{r})|^2\right]u_j(\mathbf{r}) + gN\psi_0^2(\mathbf{r})v_j(\mathbf{r}) \,. \tag{2.27}$$

And finally, for $n = -1$ we have

$$(\mu-\hbar\omega_j)v_j^*(\mathbf{r}) = \left[H_0 + 2gN|\psi_0(\mathbf{r})|^2\right]v_j^*(\mathbf{r}) + gN\psi_0^2(\mathbf{r})u_j^*(\mathbf{r}) \,. \tag{2.28}$$

Equations (2.27) and (2.28) can be rewritten,

$$\left[H_0 + 2g|\psi_0(\mathbf{r})| - \mu\right]u_j(\mathbf{r}) + gN\psi_0^2(\mathbf{r})v_j(\mathbf{r}) = \hbar\omega u_j(\mathbf{r}) \,, \tag{2.29}$$

$$\left[H_0 + 2g|\psi_0(\mathbf{r})| - \mu\right]v_j(\mathbf{r}) + gN\psi_0^{*2}(\mathbf{r})u_j(\mathbf{r}) = -\hbar\omega v_j(\mathbf{r}) \,, \tag{2.30}$$

and form the so-called Bogoliubov-de Gennes equations. It is convenient to combine them using matrix notation,

$$\begin{pmatrix} L & M \\ M^* & L \end{pmatrix} \begin{pmatrix} u_j(\mathbf{r}) \\ v_j(\mathbf{r}) \end{pmatrix} = \hbar\omega_j \begin{pmatrix} u_j(\mathbf{r}) \\ -v_j(\mathbf{r}) \end{pmatrix} , \tag{2.31}$$

where $L = H_0 + 2gN|\psi_0(\mathbf{r})| - \mu$ and $M = g\psi_0^2(\mathbf{r})$. By diagonalising this matrix one can obtain the spectrum of eigenfrequencies ω_j and corresponding eigenvectors $u_j(\mathbf{r})$ and $v_j(\mathbf{r})$.

These eigenfrequencies and eigenvectors, which are the solutions of the Bogoliubov-de Gennes equations, provide information on the stability properties of the state $\Psi(\mathbf{r}, t)$. A small positive ω_j with a positive norm $n_j = \int(|u_j(\mathbf{r})|^2 - |v_j(\mathbf{r})|^2)d\mathbf{r}$ corresponds to small oscillations about the state and indicates that the state is stable. A negative ω_j with a positive norm n_j is called an anomolous mode and indicates that the initial state will continuously transform into a lower energy state. Finally, complex and purely imaginary eigenfrequencies ω_j with $n_j = 0$ indicate the presence of a dynamical instability [43].

2.3 Trapping and Cooling

In this Section I will provide a brief overview of some of the experimental techniques used to trap and cool neutral atoms, namely the Magneto-Optical Trap (MOT) and the atom chip. A MOT is one of the most common experimental setups for trapping and cooling atoms and is often used in conjunction with atom chips to prepare the atomic cloud before it is loaded onto the atom chip. It relies on using a combination of laser cooling and magnetic trapping, both of which we will review in this Section.

I will also cover, in more detail, the basics of atom chips which are very central to this thesis. They are extremely powerful experimental devices that allow to trap, guide and manipulate cold atoms with a very high degree of flexibility.

This Section is by no means an exhaustive discussion of the experimental techniques involved and greater detail can be found in [44].

2.3.1 Optical Cooling

The main idea behind optical cooling of neutral atoms is the utilisation of the scattering force the atom feels when irradiated by a laser. The force that radiation of intensity I exerts on an area A is given by

$$F_{\text{rad}} = \frac{IA}{c} . \tag{2.32}$$

It can have a large effect on an atom, as the peak absorption cross-section $\sigma(\omega_0)$ is much greater than the physical size of the atom and can be used to change the momentum of atoms and slow them, i.e. cool them. A counter propagating laser beam will exert a force of

$$F_{\text{rad}} = -\frac{I\sigma}{c} \,, \tag{2.33}$$

where the minus sign indicates a force in the opposite direction of the atom's motion. If this is thought of in terms of photons, the atom is absorbing a photon which results in a momentum kick in the direction opposite to its motion. It then spontaneously emits a photon in a random direction which also imparts momentum but in a random direction. If this is averaged over many photons being absorbed and emitted, the net contribution of momentum due to emission averages to zero. This leaves only the momentum kick due to absorption which is opposite to the direction of the atom's motion. In this way, the average velocity of the atom, and therefore the kinetic energy of the atom, will be reduced. As this loss in kinetic energy is related to temperature by the equipartition theorem,

$$\frac{1}{2}m\overline{v^2} = \frac{1}{2}k_B T \,, \tag{2.34}$$

the net result of this process is cooling of the atom.

For this absorption process to happen, the frequency of the counter propagating laser must be detuned to account for the Doppler shift in the absorption frequency of the atom due to its motion relative to the laser. However, once the atom has been slowed, its change in velocity causes it to be taken out of resonance with the laser once again. There are many techniques for solving this problem but here, we focus on Zeeman cooling which is common in many experimental labs.

Zeeman cooling makes use of the fact that a spatially varying magnetic field changes the atomic energy levels, the Zeeman effect. This change in atomic energy levels in turn changes the absorption frequency and so it can be made match the frequency of a constant laser frequency.

To work out the form of the magnetic field which we must use to slow the atoms, let us first consider the maximum deceleration a_{max} the radiation force will produce. This deceleration can be written in terms of the recoil velocity v_r and the life time of the excited state τ

$$a_{\text{max}} = \frac{v_r}{2\tau} \,. \tag{2.35}$$

The recoil velocity is the change in the atom's velocity when a photon of wavelength Λ is absorbed or emitted,

$$v_r = \frac{h}{\Lambda m} \,, \tag{2.36}$$

where m is the mass of the atom.

If we now define the z-axis as being parallel to the direction of the beam, assume a constant deceleration a and an initial velocity v_0 we have,

$$ {v_0}^2 - v^2 = 2az \ . \tag{2.37} $$

The deceleration is usually half the maximum value to ensure that atoms are not left behind as a result of fluctuations of the optical force F_{rad} about its average value, i.e. $a = a_{\max}/2$. Therefore we can easily find that the stopping distance is

$$ L_0 = \frac{{v_0}^2}{a_{\max}} \ . \tag{2.38} $$

By combining equations (2.37) and (2.38) the atoms velocity v at a distance z from the starting point is found to be

$$ v = v_0 \left(1 - \frac{z}{L_0} \right) \ . \tag{2.39} $$

To compensate for the Doppler shift as this velocity v decreases to v_0, we now add a spatially varying magnetic field along the z-axis, $B(z)$. The frequency shift of the atomic transition caused by the Zeeman field as a result of this magnetic field must obey the following relation,

$$ \hbar\omega_0 + \mu_B B(z) = \hbar\omega + \hbar k v \ , \tag{2.40} $$

where μ_B is the Bohr magneton, ω is the laser frequency and k is the wave number. Combining eqs. (2.39) and (2.40) we find the required form of the magnetic field,

$$ B(z) = B_0 \left(1 - \frac{z}{L_0} \right)^2 + B_b \ , \tag{2.41} $$

where $B_0 = \frac{h v_0}{\Lambda \mu_B}$ and B_b is an added bias field. The value of B_b sets the velocity of the atoms at the end of the field. If $\mu_B B_b \approx \hbar\omega - \hbar\omega_0$ then the atoms will come to a complete stop.

With Zeeman cooling, and other optical cooling techniques, there is a limit on the lowest temperature achievable, the Doppler cooling limit. This limit arises because the atom does not always absorb the same number of photons in a time period t and so the absorption and emission times are not always the same. These fluctuations lead to the atom performing a random walk of velocity along the laser beam. This increase in the velocity spread v_z for a single laser beam (along the z-axis) is characterised by the equation,

$$ \overline{v_z^2} = v_r^2 R_{\text{scatt}} t \ , \tag{2.42} $$

where R_{scatt} is the scattering rate. However, this velocity spread is different for other laser configurations [44].

If we consider a six beam optical molasses setup the spread in velocity is again related to the temperature T by the equipartition theorem,

$$\frac{1}{2}m(\overline{v_x^2} + \overline{v_y^2} + \overline{v_z^2}) = \frac{1}{2}k_B T \ . \tag{2.43}$$

Once the velocity spread is calculated the minimum temperature T_D can be found,

$$T_D = \frac{\hbar\Gamma}{2k_B} \ , \tag{2.44}$$

where Γ is the excited state decay rate. This is the Doppler cooling limit.

To progress past this limit other cooling techniques are needed. One such technique is Sisyphus cooling which is based on the transfer of population between different sublevels in the Zeeman structure of alkali atoms. Within this richer potential landscape, the kinetic energy of the atom is converted to potential energy and then lost through spontaneous emission. This allows cooling beyond the Doppler limit [44].

2.3.2 Optical Trapping

When a neutral atom is subject to an external electric field it acquires an electric dipole moment. When the electric field is spatially uniform on the scale of the atom, this interaction between the atom and the electric field can be described by the dipole approximation,

$$H' = -\hat{\mu} \cdot \mathbf{E} \ , \tag{2.45}$$

where $\hat{\mu}$ is the electrical dipole operator and $\mathbf{E}$ is the external electric field.

In the case of a static electric field, this leads to a shift in the ground state energy of the atom which is given to second order by,

$$\Delta E = -\frac{1}{2}\alpha|\mathbf{E}|^2 \ , \tag{2.46}$$

where α is the atomic polarisability.

To describe the interaction between an atom and a time-dependent electric field $\mathbf{E}(\mathbf{r},\mathrm{t})$ of frequency ω, such as a laser, the energy shifts to the atom may be viewed as an effective potential seen by the atom. This is the so-called *dressed state picture*. In this

picture, the effective potential $V(\mathbf{r})$ is given as,

$$V(\mathbf{r}) = -\frac{1}{2}\alpha(\omega)\langle|\mathbf{E}(\mathbf{r},t)|^2\rangle \ , \tag{2.47}$$

where $\langle|\mathbf{E}(\mathbf{r},t)|^2\rangle$ is the time average of the electric field and $\alpha(\omega)$ is the dynamical polarisability. These shifts in the energy are sometimes referred to as the ac Stark shift, as they are the same as the usual Stark effect, but for a time-dependent electric field.

One of the main advantages in optical trapping is that the effective potential the atoms see is independent of their spin. As a result, multiple atoms from the same atomic species, with different magnetic states, can be confined in the same trap. The highly controllable nature of lasers also allows the creation of many different types of trap geometries and, for example, the combination of two counter-propagating laser beams can be used to create optical lattices. Optical traps also allow us to add magnetic fields to the system so that we can adjust the strength of the interaction between the trapped atoms via Feshbach resonances [45, 46] which occur when the energy of a bound state of an inter-atomic potential is coupled to the open state associated with collisions between the atoms. By applying an external magnetic field the energy of the different hyperfine levels can be modified and so the strength of the coupling at the resonance point can be controlled.

2.3.3 Magnetic Trapping

One of the most common and successful approaches to trapping and controlling atoms is the use of magnetic fields. When an atom is placed in a static magnetic field $\mathbf{B}$, it's energy levels are shifted, which is known as the Zeeman effect. This can be understood if we examine the Hamiltonian of an atom in an static magnetic field,

$$H = H_0 + V_{\text{mag}} \ , \tag{2.48}$$

where H_0 is the unperturbed Hamiltonian and V_{mag} is the perturbation due to the magnetic field. We write V_{mag} as

$$V_{\text{mag}} = -\hat{\mu} \cdot \mathbf{B} \ . \tag{2.49}$$

where $\hat{\mu}$ is the magnetic moment of the atom and work in a frame where the static magnetic field is aligned along the $\hat{z}$ direction, $\mathbf{B} = B\hat{z}$.

The magnetic momentum of the atom has both electronic and nuclear components

$$\hat{\mu} = -g_J\mu_B\mathbf{J} + g_I\mu_N\mathbf{I} \ , \tag{2.50}$$

where g_J and g_I are the electronic and nuclear g-factors, respectively, $\mathbf{J} = \mathbf{L} + \mathbf{S}$ is the total electronic angular momentum (the sum of total orbital angular momentum and total spin angular momentum) and $\mathbf{I}$ is the nuclear spin. We also have μ_B and μ_N, the Bohr and nuclear magneton, respectively. These are defined as

$$\begin{aligned} \mu_B &= \frac{e\hbar}{2m_e} , \\ \mu_N &= \frac{e\hbar}{2m_p} , \end{aligned} \tag{2.51}$$

where e is the elementary charge, m_e is the electron mass and m_p is the proton mass.

However, since the mass of the proton is four orders of magnitude larger than that of the electron we have $\mu_N \ll \mu_B$, and we can therefore approximate $\hat{\mu} \approx -g_J \mu_B \mathbf{J}$. It then follows that

$$V_{\text{mag}} = g_J \mu_B \mathbf{J} \cdot \mathbf{B} . \tag{2.52}$$

We now define the total angular momentum of the atom $\mathbf{F} = \mathbf{I} + \mathbf{J}$. In the case where the external magnetic field is weaker than the hyperfine interaction ($\mathbf{I} \cdot \mathbf{J}$) the procession of $\mathbf{I}$ and $\mathbf{J}$ around their resultant $\mathbf{F}$ is very rapid compared to the procession of $\mathbf{F}$ around the magnetic field on the z-axis. Therefore the quantum numbers m_I and m_J are not good quantum numbers, but F and m_F are. We now take a time average projection of $\mathbf{J}$ onto $\mathbf{F}$ given by

$$\mathbf{J}_{\text{avg}} = \frac{(\mathbf{J} \cdot \mathbf{F})}{F(F+1)} \mathbf{F} . \tag{2.53}$$

Replacing $\mathbf{J}$ with $\mathbf{J}_{\text{avg}}$ in equation (2.52) gives

$$V_{\text{mag}} = g_J \mu_B \frac{(\mathbf{J} \cdot \mathbf{F})}{F(F+1)} \mathbf{F} \cdot \mathbf{B} = g_F \mu_B \mathbf{F} \cdot \mathbf{B} = g_F \mu_B F z B , \tag{2.54}$$

where

$$g_F = g_J \mathbf{J} \cdot \mathbf{F} . \tag{2.55}$$

To evaluate this g-factor we need the two following inner products,

$$\mathbf{J} \cdot \mathbf{F} = \mathbf{J} \cdot \mathbf{I} + J^2 , \tag{2.56}$$

$$\mathbf{F} \cdot \mathbf{F} = F^2 = 2\mathbf{J} \cdot \mathbf{I} + J^2 + I^2 , \tag{2.57}$$

which given when combined

$$\mathbf{J} \cdot \mathbf{F} = \frac{F^2 + J^2 - I^2}{2} . \tag{2.58}$$

Given that $F^2|F, m_F\rangle = F(F+1)$, $J^2|J, m_J\rangle = J(J+1)$ and $I^2|I, m_I\rangle = I(I+1)$ we find that equation (2.55) evaluates to,

$$g_F = \frac{F(F+1) + J(J+1) - I(I+1)}{2F(F+1)} g_J \ . \tag{2.59}$$

This is the so-called, Landé g-factor and the energy shift due to the external magnetic field, the Zeeman energy, is therefore

$$V_{\text{mag}} = \mu_B g_F m_F B \ . \tag{2.60}$$

This energy shift is seen as a potential by the atom and can be used to trap the atom if it is spatially inhomogeneous. We can see that depending on the sign of spin of the atom m_F, it can be trapped by either a local minimum (weak field seeking states) or a local maximum (strong field seeking states). However, from the Earnshaw theorem [47] it can be shown that a magnetic local maximum is forbidden in free space without the source at the maximum and therefore high field seeking states cannot be trapped. It is for this reason that we only trap weak field seeking states with magnetic fields.

2.4 Atom Chips

Atom chips are powerful devices that are quite common in many laboratories around the world. In its simplest form, an atom chip is a series of current carrying micro/nano wires mounted on a substrate to create magnetic potentials for trapping neutral atoms above the surface of the atom chip. Due to their small size, these traps are referred to as microtraps and they provide very strong magnetic confinement for very low values of current. These low currents at which atom chips operate make them experimentally easier to work with and also allow the microtraps to be quickly turned on and off. Some of the early achievements with atom chips have been the guiding of neutral atoms with a single wire [48], the creation BECs [49] and matter wave interferometry [28]. Today, multilayer atom chips exist [50] which provide even more possibilities for potential shaping and control.

Another reason for the popularity of atom chips is that the use of chip technology allows the integration of various other experimental tools on-chip. This gives atom chips a much wider range of applications. For example, this has led to the creation of radio frequency traps [28] and the integration of optical devices [51]. Other applications of atom chips include quantum information processing [52], the study of disordered systems and atom surface interactions [53], matter-wave interferometry [28] and quantum metrology [54].

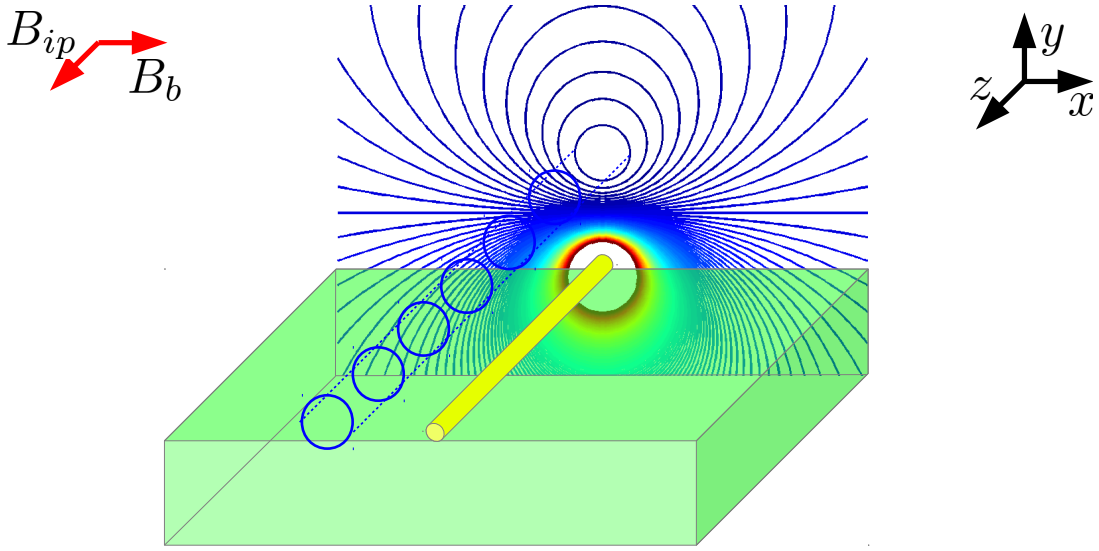

FIGURE 2.1: A schematic diagram the magnetic field created by a single straight wire (shown in yellow) parallel to the z-axis, mounted on an atom chip substrate (shown in green). The connected blue lines above the wire indicate the magnetic waveguide which can be used to guide neutral atoms. The red arrows show the direction of both the bias field B_b and the applied field B_{ip}

In the remainder of this Section we will outline how we model the atom chip potentials that we use extensively in this thesis. A more comprehensive overview of many aspects of atom chips, both experimental and theoretical, from which our description follows can be found in [25].

Atom chips rely on magnetic interaction to trap and control BECs and neutral atoms. As discussed in Section 2.3.3, when a particle with total spin F and a magnetic moment $\hat{\mu}$ is placed in an external magnetic field B, it experiences the potential

$$V_{\text{mag}} = -\hat{\mu} \cdot \mathbf{B} = -\mu_B g_F m_F B \, . \tag{2.61}$$

One of the main requirements for any from of magnetic trapping would be that the atoms follow the magnetic field. For this to happen, atoms have to retain their spin orientation relative to the magnetic field. This can be achieved by ensuring that the Larmor precession frequency ($\omega_L = \mu_B B/\hbar$) of the magnetic moment is much faster than the rate of change of the magnetic field. We can then say that the magnetic momentum adiabatically follows the direction of the field.

From Ampere's law, the magnetic field created by a straight wire carrying a current I_w in the $\hat{z}$ direction, as shown schematically in Fig. 2.1, is

$$\mathbf{B} = -\frac{\mu_0 I_w y}{2\pi(x^2+y^2)}\hat{x} + \frac{\mu_0 I_w x}{2\pi(x^2+y^2)}\hat{y} \, . \tag{2.62}$$

In this field the magnetic field lines wrap around the wire with the minimum of the field at $x = y = 0$, the centre of the wire. To trap neutral atoms in a weak field seeking state (see Section 2.3.3) we need to lift this minimum away from the centre of the wire. This can be achieved by adding a homogeneous bias field B_b orthogonal direction to the wire (see Fig. 2.1). In the case where this bias field is added in the $\hat{x}$ direction, (2.62) becomes,

$$\mathbf{B} = \left[B_b - \frac{\mu_0 I_w y}{2\pi(x^2+y^2)}\right]\hat{x} + \frac{\mu_0 I_w x}{2\pi(x^2+y^2)}\hat{y}\ , \tag{2.63}$$

and one can see that there is a point at which this magnetic field is zero along $x = 0$ and a finite value of y given by,

$$y = r_0 = \left(\frac{\mu_0}{2\pi}\right)\frac{I_w}{B_b}\ . \tag{2.64}$$

Inserting this into equation (2.63) one finds

$$\mathbf{B} = \frac{\mu_0 I_w}{2\pi}\left\{\left(\frac{1}{r_0} - \frac{y}{(x^2+y^2)}\right)\hat{x} + \frac{x}{(x^2+y^2)}\hat{y}\right\}\ . \tag{2.65}$$

It is important to consider what physically happens to the atom around r_0, where the magnetic field and the bias field cancel. At and around this point, the Larmor precession frequency becomes small near zeros of the trap. Physically this means that the spin of the atom no longer follows the field and so the spin can freely precess and flip. These spin flips lead to the atoms transitioning between trapped and untrapped states and they can therefore fall out of the trap. Such losses near the zeros of magnetic fields are referred to as Majorana losses [55].

To prevent such losses we remove the zero of the field by applying another homogeneous magnetic field B_{ip} parallel to the direction of the wire ($\hat{z}$ direction, see Fig. 2.1) to lift the zero. This type of potential is called an Ioffe-Pritchard trap [56].

With the extra applied field added along the $\hat{z}$ direction, the overall field can be written as

$$\mathbf{B} = \frac{\mu_0 I_w}{2\pi}\left\{\left(\frac{1}{r_0} - \frac{y}{(x^2+y^2)}\right)\hat{x} + \frac{x}{(x^2+y^2)}\hat{y}\right\} + B_{ip}\hat{z}\ . \tag{2.66}$$

For the proceeding analysis it is convenient to rewrite (2.66) in cylindrical co-ordinates,

$$\mathbf{B} = \frac{\mu_0 I_w}{2\pi}\left[\left(\frac{1}{r_0} - \frac{\cos\theta}{r}\right)\hat{x} + \frac{\sin\theta}{r}\hat{y}\right] + B_{ip}\hat{z}\ , \tag{2.67}$$

but, as highlighted by (2.61), only the magnitude of the magnetic field is required to find the potential V_{mag},

$$|\mathbf{B}| = \left[\left(\frac{\mu_0 I_w}{2\pi} \right)^2 \frac{r^2 + r_0^2 - 2rr_0 \cos\theta}{r^2 r_0^2} + B_{ip}^2 \right]^{1/2} . \tag{2.68}$$

If we now consider the magnetic field as we approach the trap minimum ($r \to r_0$), we have $r^2 r_0^2 \approx r_0^4$ and $\cos\theta \approx 1$. Therefore, in this limit, (2.68) reduces to

$$|\mathbf{B}| = \left[\left(\frac{\mu_0 I_w}{2\pi} \right)^2 \frac{(r - r_0)^2}{r_0^4} + B_{ip}^2 \right]^{1/2} = B_{ip} \left[1 + \frac{B_b^2 (r - r_0)^2}{r_0^2 B_{ip}^2} \right]^{1/2} . \tag{2.69}$$

Finally we take the second order Taylor expansion to find,

$$|\mathbf{B}| = B_{ip} + \frac{B_b^2 (r - r_0)^2}{2 r_0^2 B_{ip}} , \tag{2.70}$$

and substitute this expression into (2.61) to produce the magnetic potential seen by the atom,

$$V_{\text{mag}} = \mu_B g_F m_F B_{ip} + \frac{1}{2} \frac{\mu_B g_F m_F B_b^2}{r_0^2 B_{ip}} (r - r_0)^2 . \tag{2.71}$$

As indicated by this expression, the potential close to the minimum can be viewed as a harmonic oscillator offset by $\mu_B g_F m_F B_{ip}$. We can write the trap frequency of this harmonic oscillator as

$$\omega = \frac{B_b}{r_0} \sqrt{\frac{\mu_B g_F m_F}{m B_{ip}}} , \tag{2.72}$$

where m is the mass of the atom. From this expression we can see that we can control the trapping frequency of the magnetic waveguide by adjusting either B_b or B_{ip}. When also considering the expression for r_0 (2.64), the height of the waveguide above the surface of the chip, the ability to adjust I_w, B_b and B_{ip} separately from each other allows us to easily modify the waveguide.

This covers the basics of what the magnetic trapping potentials on atoms chips look like and how to treat them mathematically. We will make extensive use of these powerful tools to study the CTAP process in Chapter 3, where more details on the atom chip we consider are given. The values of various system parameters are closely related to possible experiments.

2.5 CTAP: Coherent Tunnelling by Adiabatic Passage

In this section we will give an overview of the CTAP process which is used extensively in this thesis. The motivation behind the development of CTAP is that the fidelity of direct tunnelling between traps is time-dependent (this is detailed in Section 2.5.1) and therefore a controllable mechanism for transferring particles from one trap to another is a difficult experimental task. As we will see in this section, CTAP provides a method of transitioning between trapped states in a manner that is time-independent (provided the process is adiabatic) and robust to variations in system parameters.

2.5.1 Two Level System: Direct Coupling

To understand our interest in the CTAP technique we first look at a system consisting of two states $|1\rangle$ and $|2\rangle$.

In the absence of any driving field (coupling), our bare Hamiltonian is

$$\hat{H}_0 = \hbar \begin{pmatrix} 0 & 0 \\ 0 & \omega_0 \end{pmatrix} , \tag{2.73}$$

where ω_0 is the resonant transition frequency between $|1\rangle \rightarrow |2\rangle$. The energy eigenstates of the Hamiltonian (2.73) are by construction the states $|1\rangle$ and $|2\rangle$, with eigenenergies $E_1 = 0$ amd $E_2 = \hbar\omega_0$.

Let us now consider the time evolution of the state of the system $|\Psi(t)\rangle$ as described by the Schrödinger equation,

$$i\hbar \frac{\partial |\Psi(t)\rangle}{\partial t} = \hat{H}_0 |\Psi(t)\rangle \ . \tag{2.74}$$

With a time-independent Hamiltonian we can write $\hat{H}_0|\Psi(t)\rangle = E|\Psi(t)\rangle$, i.e. the energy is conserved and so we have

$$i\hbar \frac{\partial |\Psi(t)\rangle}{\partial t} = E|\Psi(t)\rangle \ . \tag{2.75}$$

Integration gives,

$$|\Psi(t)\rangle = e^{-iEt/\hbar}|\Psi(0)\rangle \ . \tag{2.76}$$

As we can see from this expression, if the quantum state of the system $|\Psi\rangle$, begins in an energy eigenstate, it only acquires a phase as it evolves in time. More explicitly if $|\Psi(0)\rangle = |j\rangle$, then $|\Psi(t)\rangle = e^{-iE_j t/\hbar}|j\rangle$ where $j \in [1, 2]$.

We now introduce a driving field of the form $\Omega \cos(\omega t)$ which continuously perturbs the system. Here, the amplitude of this perturbation Ω is called the Rabi frequency. This

perturbation is represented by the operator,

$$\hat{H}_{\text{int}}(t) = \hbar \begin{pmatrix} 0 & \Omega\cos(\omega t) \\ \Omega^* \cos(\omega t) & 0 \end{pmatrix} . \tag{2.77}$$

The total Hamiltonian for our system is $\hat{H} = \hat{H}_0 + \hat{H}_{\text{int}}(t)$,

$$\hat{H} = \hbar \begin{pmatrix} 0 & \Omega\cos(\omega t) \\ \Omega^* \cos(\omega t) & \omega_0 \end{pmatrix} . \tag{2.78}$$

With this time-dependent Hamiltonian, the energy eigenstates no longer just acquire a phase as they evolve, $\hat{H}|j\rangle \neq A|j\rangle$ where A is a constant, i.e. the driving field couples the levels.

To derive the solutions to the Schrödinger equation as above we must remove the time dependence from the Hamiltonian. The first step in doing so is moving to a frame which rotates with the frequency ω, the frequency of the driving field. To move to a rotating frame we must apply a unitary transformation $\hat{U}$ of the form,

$$\hat{U} = \exp\left(\frac{-i\hat{A}t}{\hbar}\right) , \tag{2.79}$$

where $\hat{A}$ is a Hermitian operator. Applying this to a wavefunction $|\Psi\rangle$ and then inserting it into the Schrödinger equation we get

$$\begin{aligned} i\hbar\frac{d\hat{U}^\dagger|\Psi\rangle}{dt} &= i\hbar\hat{U}^\dagger\frac{\partial|\Psi\rangle}{\partial t} + i\hbar\frac{\partial\hat{U}^\dagger}{\partial t}|\Psi\rangle \\ &= \hat{U}^\dagger\hat{H}|\Psi\rangle - \hat{A}\hat{U}^\dagger|\Psi\rangle \\ &= (\hat{U}^\dagger\hat{H}\hat{U} - \hat{A})\hat{U}^\dagger|\Psi\rangle . \end{aligned} \tag{2.80}$$

Therefore the Hamiltonian in a rotating frame, $\hat{H}'$, is

$$\hat{H}' = \hat{U}^\dagger\hat{H}\hat{U} - \hat{A} . \tag{2.81}$$

For our specific system we wish to move to a frame which rotates with the frequency ω. The form of $\hat{A}$ which is required is,

$$\hat{A} = \hbar \begin{pmatrix} 0 & 0 \\ 0 & \omega \end{pmatrix} . \tag{2.82}$$

With this operator, the Hamiltonian (2.78) under rotation becomes $\hat{H}'$,

$$\hat{H}' = e^{-i\hat{A}t/\hbar}\hat{H}e^{-i\hat{A}t/\hbar} - \hat{A}\,. \tag{2.83}$$

To evaluate this expression we use the identity $\cos(\omega t) = \frac{e^{i\omega t}+e^{-i\omega t}}{2}$, so that (2.83) becomes

$$\hat{H}' = \frac{\hbar}{2}\begin{pmatrix}1 & 0\\ 0 & e^{i\omega t}\end{pmatrix}\begin{pmatrix}0 & \Omega(e^{i\omega t}+e^{-i\omega t})\\ \Omega^*(e^{i\omega t}+e^{-i\omega t}) & 2(\omega_0-\omega)\end{pmatrix}\begin{pmatrix}1 & 0\\ 0 & e^{-i\omega t}\end{pmatrix}\,. \tag{2.84}$$

Multiplying this expression out leads to only exponentials with powers of $-i2\omega t$ being left;

$$\hat{H}' = \frac{\hbar}{2}\begin{pmatrix}0 & \Omega(1+e^{-i2\omega t})\\ \Omega^*(1+e^{-i2\omega t}) & -2\Delta\end{pmatrix}\,, \tag{2.85}$$

where $\Delta = \omega - \omega_0$.

In the case of $\omega \approx \omega_0$ (the driving field is near resonance) the complex exponential terms are oscillating at twice the transition frequency and therefore, the oscillations will quickly time average to zero. The *rotating wave approximation* (RWA) is the claim that these terms may be neglected and the Hamiltonian (2.85)can be written as

$$\hat{H}_{\mathrm{RWA}} = \frac{\hbar}{2}\begin{pmatrix}0 & \Omega\\ \Omega^* & -2\Delta\end{pmatrix}\,. \tag{2.86}$$

At this point the state of this two level system at any point in time can be described as

$$|\Psi(t)\rangle = c_1(t)|1\rangle + c_2(t)|2\rangle\,, \tag{2.87}$$

where $c_1(t)$ and $c_2(t)$ are complex state amplitudes with the requirement that $|c_1(t)|^2 + |c_2(t)|^2 = 1$. It follows that the probability of finding the system in the state $|j\rangle$ at time t is $|\langle j|\Psi(t)\rangle|^2 = |c_j(t)|^2$.

To find the expression for how the state amplitudes $c_1(t)$ and $c_2(t)$ evolve in time we solve the Schrödinger equation with this RWA Hamiltonian (2.86):

$$i\hbar\frac{d|\Psi(t)\rangle}{dt} = \hat{H}_{\mathrm{RWA}}|\Psi(t)\rangle\,, \tag{2.88}$$

which can be represented in matrix form as

$$i\begin{pmatrix}\dot{c_1}(t)\\ \dot{c_2}(t)\end{pmatrix} = \frac{1}{2}\begin{pmatrix}0 & \Omega\\ \Omega^* & -2\Delta\end{pmatrix}\begin{pmatrix}c_1(t)\\ c_2(t)\end{pmatrix}\,. \tag{2.89}$$

By multiplying out this equation the following differential equations are obtained,

$$\begin{aligned}\dot{c_1}(t) &= -\frac{i}{2}\Omega c_2(t)\ ,\\ \dot{c_2}(t) &= -\frac{i}{2}\Omega^* c_1(t) + i\Delta c_2(t)\ .\end{aligned} \tag{2.90}$$

To explicitly solve this set of differential equations we require initial conditions which are obtained by considering that the system is initially in state $|1\rangle$. This implies that $c_1(0) = 1$ and $c_2(0) = 0$ and so the total system of equations to solve is

$$\begin{aligned}\dot{c_1}(t) &= -\frac{i}{2}\Omega c_2(t)\\ \dot{c_2}(t) &= -\frac{i}{2}\Omega^* c_1(t) + i\Delta c_2(t)\\ c_1(0) &= 1\\ c_2(0) &= 0\ .\end{aligned} \tag{2.91}$$

If we now require that the phase of the field is zero, i.e. $\Omega^* = \Omega$, the solution of (2.91) can be written as,

$$\begin{pmatrix} c_1(t) \\ c_2(t) \end{pmatrix} = e^{\frac{it\Delta}{2}} \begin{pmatrix} \cos\left(\frac{\Omega_R t}{2}\right) - i\frac{\Delta}{\Omega_R}\sin\left(\frac{\Omega_R t}{2}\right) \\ -i\frac{\Omega}{\Omega_R}\sin\left(\frac{\Omega_R t}{2}\right) \end{pmatrix}\ , \tag{2.92}$$

where $\Omega_R^2 = \Omega^2 + \Delta^2$ and is referred to as the total Rabi frequency. Therefore, assuming the system begins in state $|1\rangle$, the state amplitudes $|c_1(t)|^2$ and $|c_2(t)|^2$ evolve according to

$$|c_1(t)|^2 = \frac{\Omega^2}{\Omega_R^2}\sin^2\left(\frac{\Omega_R t}{2}\right)\ , \tag{2.93a}$$

$$|c_2(t)|^2 = \frac{\Delta^2}{\Omega_R^2} + \frac{\Omega^2}{\Omega_R^2}\cos^2\left(\frac{\Omega_R t}{2}\right)\ . \tag{2.93b}$$

From (2.93) we can see that the probability to be in state $|1\rangle$ or $|2\rangle$ oscillates with frequency Ω_R. These oscillations between the two levels of the system are the so-called Rabi oscillations, and are at the core of the problem CTAP tries to solve.

More explicitly, this result shows that if one attempts to perform population transfer between the two states of a two level system via direct coupling, the presence of Rabi oscillations makes the population in the target state time-dependent. So while high fidelity transport of the population from one state to the other is possible, it would

require precise control over the timing of the process and the strength of the driving field.

2.5.2 Three Level System

Now that we have illustrated how population transfer in a two level system by direct coupling induces Rabi oscillations, we show how introducing a third, intermediate level and using time-dependent Rabi frequencies, can remove these unwanted Rabi oscillations. This type of scheme was first suggested as a way of making coherent transitions in internal atomic states where the motivation was to get rid of the spontaneous emissions from the intermediate excited state. In this optical context it is referred to as stimulated Raman adiabatic passage (STIRAP).

2.5.2.1 STIRAP

First consider two atomic hyperfine states which we label $|1\rangle$ and $|3\rangle$ with energies E_1 and E_3 respectively. Both of these atomic states will be taken to be stable, as one-photon transitions between them are forbidden since a single photon would produce a change in angular momentum of either $+1$ or -1. As such, to make a transition between $|1\rangle$ and $|3\rangle$, a two-photon Raman process is required in order not to add angular momentum.

However, such a transition introduces a third intermediate excited state which we label $|2\rangle$ with energy E_2. When the atom occupies this excited state it has a chance to spontaneously emit a photon and decay into a different state outside the defined three level system. As such, using this two-photon Raman process will suffer from losses because of this intermediate excited state. The purpose of the STIRAP process is to prevent such losses from occurring.

We now introduce a pair of driving fields to couple the levels in the form of two laser fields, pump field and Stokes field, with time-dependent Rabi frequencies $\Omega_P(t)$ and $\Omega_S(t)$ respectively. The pump field with Rabi frequency Ω_P couples $|1\rangle \rightarrow |2\rangle$ and a Stokes pulse with Rabi frequency Ω_S couples $|2\rangle \rightarrow |3\rangle$. Fig. 2.2 (a) gives a schematic of the system.

The Hamiltonian of this system within the RWA is

$$\hat{H} = \frac{\hbar}{2} \begin{pmatrix} 0 & \Omega_P(t) & 0 \\ \Omega_P(t) & 2\Delta_P & \Omega_S(t) \\ 0 & \Omega_S(t) & 2(\Delta_P - \Delta_S) \end{pmatrix} . \tag{2.94}$$

We write the detuning of the pump laser from resonance with the $|1\rangle \rightarrow |2\rangle$ transition as $\hbar\Delta_P = (E_2 - E_1) - \hbar\omega_P$ and the detuning of the Stokes laser from resonance with the $|2\rangle \rightarrow |3\rangle$ transition as $\hbar\Delta_S = (E_2 - E_3) - \hbar\omega_S$. Diagonalizing the Hamiltonian (2.94) leads to three eigenstates [57]

$$\begin{aligned} |a^+\rangle &= \sin\theta \sin\Phi|1\rangle + \cos\Phi|2\rangle + \cos\theta \sin\Phi|3\rangle \ , \\ |a^-\rangle &= \sin\theta \cos\Phi|1\rangle - \sin\Phi|2\rangle + \cos\theta \sin\Phi|3\rangle \ , \\ |d\rangle &= \cos\theta|1\rangle + \sin\theta|3\rangle \ , \end{aligned} \tag{2.95}$$

with corresponding eigenvalues

$$\begin{aligned} \omega^+ &= \Delta_P + \sqrt{{\Delta_P}^2 + {\Omega_P}^2 + {\Omega_S}^2} \ , \\ \omega^- &= \Delta_P - \sqrt{{\Delta_P}^2 + {\Omega_P}^2 + {\Omega_S}^2} \ , \\ \omega^d &= 0 \ . \end{aligned} \tag{2.96}$$

Here the time varying mixing angle θ is defined by the ratios of the Rabi frequencies,

$$\tan\theta = \frac{\Omega_P(t)}{\Omega_S(t)} \ , \tag{2.97}$$

and the second angle Φ is given as [57]

$$\tan\Phi = \frac{\left[\Omega_P(t)^2 + \Omega_S(t)^2\right]^{\frac{1}{2}}}{\left[\Omega_P(t)^2 + \Omega_S(t)^2 + {\Delta_P}^2\right]^{\frac{1}{2}} + \Delta_P} \ . \tag{2.98}$$

For our purposes the most important of these eigenstates is $|d\rangle$, the so called dark state as it does not occupy the excited state at any time and therefore does not include the possibility of spontaneous emission. The utility of this state for population transfer comes from how we change the mixing angle θ in time. It also has no dependence on Φ.

Consider the case where both lasers are tuned to their respective transition frequencies, $\Delta_S = \Delta_P = 0$, and the population is initially in $|1\rangle$. Before the pulses are applied, all three eigenvalues are degenerate. If we first apply the Stokes pulse $\Omega_s(t)$ and then after a time delay of τ, apply the pump pulse $\Omega_p(t)$, this causes the mixing angle to move through $\theta = 0 \rightarrow \frac{\pi}{2}$. Moving the mixing angle in this way causes the population of $|d\rangle$ to transfer from $|1\rangle \rightarrow |3\rangle$ without ever occupying the excited state $|2\rangle$. Fig. 2.2 (b) gives a schematic of the counter-intuitive arrangement of pump and Stokes pulses.

If we wish to utilise state $|d\rangle$ for population transfer, our system needs to remain in state $|d\rangle$ at all times during the process. This is done by ensuring that the process is adiabatic.

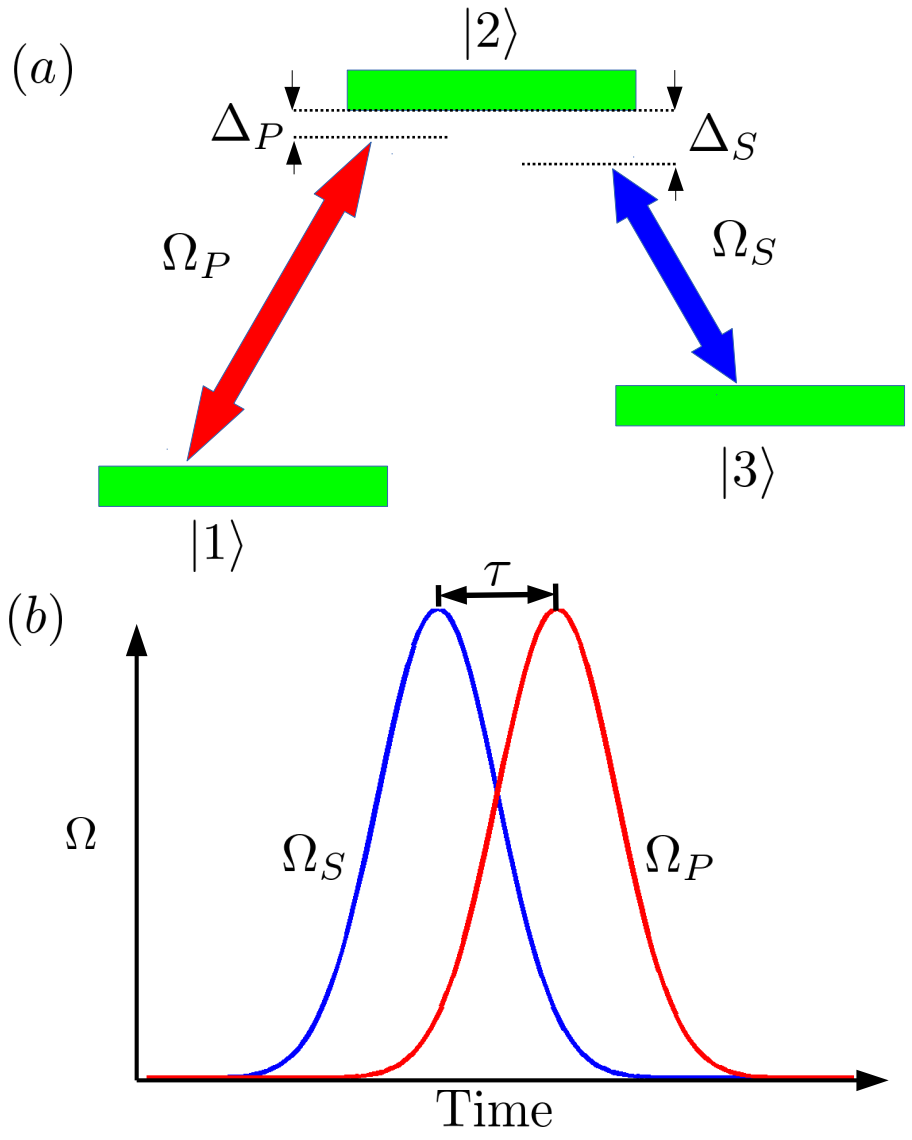

FIGURE 2.2: Schematic of the STIRAP process. (a) The two stable states $|1\rangle$ and $|3\rangle$ are coupled to the excited state $|2\rangle$ by a pump (red arrow) and Stokes laser (blue arrow) with time-dependent Rabi frequencies $\Omega_P(t)$ and $\Omega_S(t)$ respectively. The detunings of the pump and Stokes lasers from the transition frequency are Δ_P and Δ_S, respectively. (b) The counter-intuitive application of the laser pulses. Note the time delay τ in the application of the pump pulse (red line) after the Stokes pulse (blue line).

We note from (2.96) that any pulse application lifts the degeneracy of the eigenvalues with only ω^d remaining unchanged at zero. Therefore if the system is prepared in state $|d\rangle$, an adiabatic application of the counter-intuitive arrangement of pump and Stokes pulses will prevent any energy change, forcing the system to remain in state $|d\rangle$, and therefore transfer the population from $|1\rangle \rightarrow |3\rangle$. Non-adiabatic behaviour can lead to transitions between the eigenstates (2.95).

The advantage of utilising the STIRAP technique in this more complicated three-level

system, instead of direct coupling between consecutive levels in the three level system, is that the Rabi oscillations between the directly coupled states are removed. In direct coupling, the presence of Rabi oscillations mean that the population in the target state is time-dependent, and so, if one wishes to achieve high fidelities one must have precise control over the timing of the process. By using the STIRAP technique these Rabi oscillations are eliminated and so, as long as the process is adiabatic, the population in the target state is time-independent and high fidelity population transfer is achievable in a robust manner.

2.5.2.2 CTAP

While the STIRAP process has been known and extensively used in the realm of optics, it was only recently shown by Eckert *et al.* [20] that it has an atom optical analogue dubbed Coherent Tunnelling by Adiabatic Passage (CTAP). The basic idea is that instead of a three level optical system, one can consider a 1D system of three identical traps in a linear arrangement, with an atom initially confined to the left-most trap as shown in Fig. 2.3.

We describe the centre-of-mass state of the atom in this system using the ground state of each of the traps as a basis labelled $|L\rangle$, $|M\rangle$ and $|R\rangle$ for the left, middle and right trap respectively. For this to be valid our atom must have a well defined energy (no thermal fluctuations) so that it can be considered to be in a linear combination of the ground states of our traps at all times. This makes cold atoms an ideal candidate.

In this basis our state $|\Psi\rangle$ is given as

$$|\Psi\rangle = c_L|L\rangle + c_M|M\rangle + c_R|R\rangle \ . \tag{2.99}$$

In this system the time-dependent optical coupling of the pump and Stokes pulses is replaced by the time-dependent tunnel coupling between the traps. Like the Rabi frequencies $\Omega_P(t)$ and $\Omega_S(t)$ of our laser, we define $J_{LM}(t)$ as the tunnelling strength between $|L\rangle$ and $|M\rangle$ while $J_{MR}(t)$ as the tunnelling strength between $|M\rangle$ and $|R\rangle$. As the tunnelling strength depends exponentially on the distance between the states, the linear arrangement of our traps means that there is no significant coupling between $|L\rangle$ and $|R\rangle$.

With three identical traps that are well separated, we can consider them to be in resonance to a high degree of accuracy. However, when the traps are then brought closer together so that they begin to overlap, this resonance is no longer guaranteed. Solving this issue is one of the central problems in this thesis and will be discussed in more

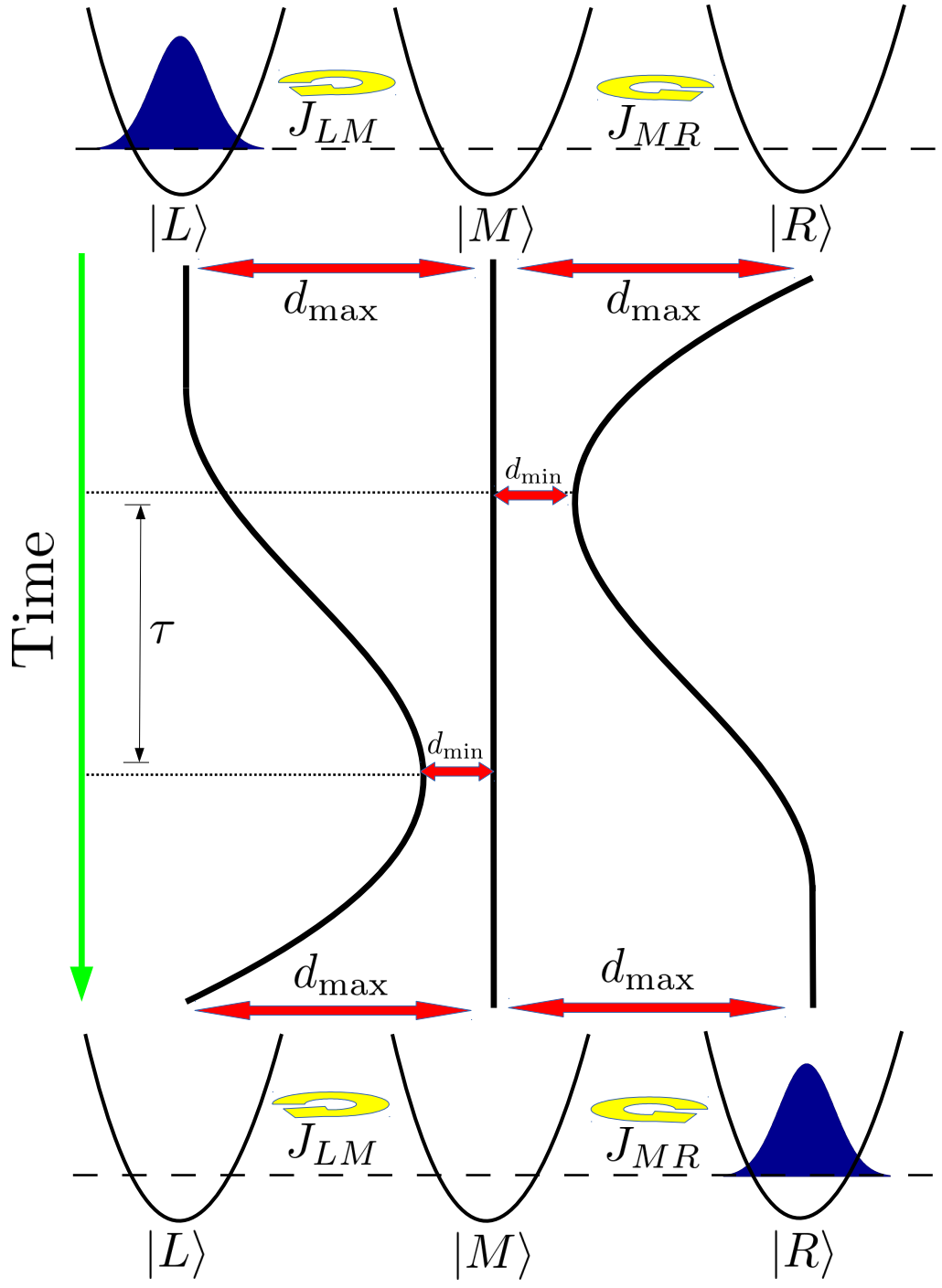

FIGURE 2.3: Schematic of the CTAP process for an atom in the left trap $|L\rangle$. Changing the distance between the middle and outer traps in time from a maximum value d_{max} to a minimum value d_{min} as indicated by the solid black lines leads to the counter-intuitive change in tunnelling strengths (J_{LM} and J_{RM}) needed for CTAP. In this scheme we have exaggerated the time delay (τ) in the movement of the traps.

detail in the following Chapters. For now, to demonstrate the basic CTAP process, we assume that the traps do not influence each other and we consider them to be piecewise harmonic.

The Hamiltonian of this system is

$$\hat{H} = \hbar \begin{pmatrix} 0 & -J_{LM}(t) & 0 \\ -J_{LM}(t) & 0 & -J_{MR}(t) \\ 0 & -J_{MR}(t) & 0 \end{pmatrix} , \tag{2.100}$$

where we have scaled the ground state energy of each trap to be zero. We note that this Hamiltonian is the same as the Hamiltonian for STIRAP (2.94) with no detuning (all trapped states are resonant). Diagonalisation of this Hamiltonian results in the same eigenstates and one can expect similar physics. In particular, diagonalising produces the atom optical analogue of the dark state $|d\rangle$ as one of the eigenstates,

$$|d\rangle = \cos\theta|L\rangle - \sin\theta|R\rangle , \tag{2.101}$$

and its associated mixing angle

$$\tan\theta = \frac{J_{LM}(t)}{J_{MR}(t)} . \tag{2.102}$$

As we can see, this dark state $|d\rangle$ has no contribution from $|M\rangle$, the middle trap. Therefore if the state of the atom adiabatically follows $|d\rangle$, at no point in time will it occupy the middle trap.

To perform population transfer from $|L\rangle$ to $|R\rangle$ by exploiting this dark state, we must adjust the tunnel couplings $J_{LM}(t)$ and $J_{MR}(t)$ in order to control the mixing angle θ. This is achieved by controlling the position of the traps in time and, like STIRAP, must be done in a counter-intuitive fashion. First, we assume our atom is localised in the left trap initially and that all traps are equidistant from each other at a distance of d_{max}. We then bring the right trap close to the middle trap first and then, after a time delay τ, bring the left trap close to the middle trap. Once the right trap has reached the minimum distance from the middle trap d_{min} we then move it back to its starting position. Finally the left trap is returned to its starting position, but again after a time delay τ. A schematic of this process is shown in Fig. 2.3.

If this counter intuitive movement of the traps is done adiabatically we find that the trap population moves from $|L\rangle \rightarrow |R\rangle$ without ever occupying $|M\rangle$. CTAP has the same advantages over direct tunnelling that we highlighted in the STIRAP case. Direct tunnelling between two traps will have Rabi oscillations between the traps. This again makes the process time-dependent and we not only need good control over the timing of

the process, we also must have good control over the positions on the traps. With CTAP these restrictions are relaxed and we can achieve robust, high fidelity population transfer as long the process is adiabatic and our traps are kept in resonance with each other. However, for CTAP to be a viable option for a system in which we wish to transport the centre-of-mass state of an atom, the process must be faster than the lifetime of the atom.

2.6 Radio Frequency Trapping

In this Section we give an overview of the two approaches used in this thesis for describing adiabatic rf potentials. The first approach, which will be referred to as the piecewise resonance model, uses a local frequency approximation to evaluate the adiabatic eigenvalues of the system. This is the method used in Chapter 4 of this thesis. The second approach uses Floquet theory [30] to obtain the adiabatic eigenvalues, which is the focus of Chapter 5.

Before each approach is described in detail, I will first derive the general Hamiltonian for a magnetically trapped atom interacting with an rf field. The two approaches then differ in their way of treating the time-dependence and will be discussed separately.

2.6.1 General Hamiltonian

Consider an atomic hyperfine ground state of an alkali atom interacting with a magnetic field $\mathbf{B}(\mathbf{r},t)$. The Hamiltonian that describes its dynamics is given by

$$H(\mathbf{r},t) = \mu_B g_F \mathbf{B}(\mathbf{r},t)\cdot\mathbf{F}\ . \tag{2.103}$$

Here μ_B is the Bohr magneton, g_F is the g-factor of the hyperfine level and $\mathbf{F}=\mathbf{J}+\mathbf{I}$ is the total angular momentum operator where $\mathbf{J}$ is the total electronic angular momentum operator and $\mathbf{I}$ is the nuclear spin operator. As discussed in Section 2.3.3, this expression is valid as long as F remains a good quantum number, i.e the magnetic field is not too strong. Otherwise only the components of $\mathbf{J}$ and $\mathbf{I}$ parallel to $\mathbf{F}$ are important.

Now consider the situation where the atom is confined in a static trapping field $\mathbf{B}_{\mathrm{s}}(\mathbf{r})$ and is irradiated with a linearly polarised radio frequency field $\mathbf{B}_{\mathrm{rf}}(\mathbf{r})\cos(\omega t)$. The total $\mathbf{B}(\mathbf{r},t)$ then is

$$\mathbf{B}(\mathbf{r},t) = \mathbf{B}_{\mathrm{s}}(\mathbf{r}) + \mathbf{B}_{\mathrm{rf}}(\mathbf{r})\cos(\omega t)\ . \tag{2.104}$$

Note that the index indicating the radio frequency field has been replaced for ease of notation here by the counter for the respective field.

For the types of adiabatic rf potentials we wish to consider in this thesis, we require N such linearly polarised radio frequency fields $\mathbf{B}_n(\mathbf{r})\cos(\omega_n t)$ where $n \in [1, N]$ so that the total $\mathbf{B}(\mathbf{r}, \mathbf{t})$ becomes

$$\mathbf{B}(\mathbf{r}, t) = \mathbf{B}_{\mathrm{s}}(\mathbf{r}) + \sum_{n=1}^{N} \mathbf{B}_n(\mathbf{r})\cos(\omega_n t) \; . \tag{2.105}$$

Both the piecewise resonance and the Floquet approach deal with multiple frequencies differently. For now, we continue with this generalised Hamiltonian and the next step is to move to a frame where the static trapping field $\mathbf{B}_{\mathrm{s}}(\mathbf{r})$ is always orientated along in the z-direction. In such a frame the Hamiltonian becomes

$$\begin{aligned} H(\mathbf{r}, t) = \mu_B g_F \Bigg\{ & B_{\mathrm{s}}(\mathbf{r}) F_z + \left[\sum_{n=1}^{N} B_{n_x}(\mathbf{r})\cos(\omega_n t) \right] F_x \\ & + \left[\sum_{n=1}^{N} B_{n_y}(\mathbf{r})\cos(\omega_n t) \right] F_y + \left[\sum_{n=1}^{N} B_{n_z}(\mathbf{r})\cos(\omega_n t) \right] F_z \Bigg\} \; , \end{aligned} \tag{2.106}$$

where both $\mathbf{F}$ and $\mathbf{B}_n(\mathbf{r})$ have been decomposed into their contributions along each axis in this frame.

The components of the rf fields that oscillate parallel to the static field, $B_{n_z}(\mathbf{r})\cos(\omega_n t)$, can be neglected if $\mu B_{n_z}(\mathbf{r}) \ll \hbar\omega_n$. Physically this means that the Larmor frequency associated with the rf field component parallel to the static field, $\omega_L = \sqrt{(\omega_n - \omega_t)^2 + {\Omega_n}^2}$ where ω_t is the atomic transition frequency and Ω_n the Rabi frequency of the rf field, is small compared to the oscillation frequency of the rf field. Therefore this component does not significantly modify the static field Larmor frequency and its contribution may be time-averaged to zero [58]. As such, only the elements of the rf field perpendicular to the static field, $B_{n_x}(\mathbf{r})\cos(\omega_n t)$ and $B_{n_y}(\mathbf{r})\cos(\omega_n t)$, contribute to coupling between the atomic levels [59] and (2.106) can be written as

$$\begin{aligned} H(\mathbf{r}, t) = \mu_B g_F \Bigg\{ & B_{\mathrm{s}}(\mathbf{r}) F_z + \left[\sum_{n=1}^{N} B_{n_x}(\mathbf{r})\cos(\omega_n t) \right] F_x \\ & + \left[\sum_{n=1}^{N} B_{n_y}(\mathbf{r})\cos(\omega_n t) \right] F_y \Bigg\} \; . \end{aligned} \tag{2.107}$$

Diagonalising this Hamiltonian is not trivial due to the time-dependently oscillating terms. Removing this time-dependence can be done in different ways and using different approximations, which is the point at which the piecewise resonance model and the Floquet model differ. We therefore present them separately, beginning with the piecewise resonance model in the following Section.

2.6.2 Piecewise Resonance Model

In this Section we present the detailed treatment of the piecewise resonance model we use to obtain the adiabatic rf potentials used in Chapter 4 of this thesis. This method was first used in [29] and is applicable in the limit where the different frequencies are well separated and the Rabi frequencies of the fields are not too large.

As previously stated, the next step in obtaining the adiabatic rf potentials is the removal of the time dependence from the Hamiltonian (2.107). Let us first discuss the procedure for a Hamiltonian with a single rf field and then, in the next Section, detail how to account for multiple rf fields.

For a single rf field, $N = 1$, the Hamiltonian (2.107) can be written as

$$H(\mathbf{r},t) = \mu_B g_F B_{\mathrm{s}}(\mathbf{r}) F_z + \mu_B g_F [B_{\mathrm{rf}_x}(\mathbf{r}) F_x \cos(\omega t) + B_{\mathrm{rf}_y}(\mathbf{r}) F_y \cos(\omega t)] \ . \tag{2.108}$$

where we have relabelled $B_1(\mathbf{r})\cos(\omega_1 t)$ as $B_{\mathrm{rf}}(\mathbf{r})\cos(\omega t)$. To remove the time dependence from this Hamiltonian, the first step is to move to a frame which rotates about the z-axis with the frequency of the rf field ω. This procedure is equivalent to the one described in Section 2.5.1, where one applies a unitary transformation U such that the Hamiltonian becomes,

$$H'(\mathbf{r},t) = U^\dagger H(\mathbf{r},t) U - F_z \hbar\omega \ , \tag{2.109}$$

where

$$U = \exp\left(-iF_z\omega t\right) \ . \tag{2.110}$$

Therefore, by applying this transformation to the Hamiltonian (2.108), one finds that the transformed Hamiltonian $H'(\mathbf{r},t)$ is given as,

$$\begin{aligned} H'(\mathbf{r},t) = \mu_B g_F \left(B_{\mathrm{s}}(\mathbf{r}) - \frac{\hbar\omega}{\mu_B g_F} \right) F_z + \mu_B g_F \Big\{ & B_{\mathrm{rf}_x}(\mathbf{r}) \left[F_x \cos^2(\omega t) - F_y \cos(\omega t)\sin(\omega t) \right] \\ & + B_{\mathrm{rf}_y}(\mathbf{r}) \left[F_x \cos(\omega t)\sin(\omega t) + F_y \cos^2(\omega t) \right] \Big\} \ . \end{aligned} \tag{2.111}$$

Using the identities $\cos^2(\omega t) = \frac{1-\cos(2\omega t)}{2}$ and $\cos(\omega t)\sin(\omega t) = \frac{\sin(2\omega t)}{2}$, eq. (2.111) can be rewritten as,

$$\begin{aligned} H'(\mathbf{r},t) = \mu_B g_F \left(B_{\mathrm{s}}(\mathbf{r}) - \frac{\hbar\omega}{\mu_B g_F} \right) F_z + & \mu_B g_F B_{\mathrm{rf}_x}(\mathbf{r}) \left[F_x \left(\frac{1}{2} - \frac{\cos(2\omega t)}{2} \right) - F_y \frac{\sin(2\omega t)}{2} \right] \\ & + \mu_B g_F B_{\mathrm{rf}_y}(\mathbf{r}) \left[F_x \frac{\sin(2\omega t)}{2} + F_y \left(\frac{1}{2} - \frac{\cos(2\omega t)}{2} \right) \right] \ . \end{aligned} \tag{2.112}$$

This expression can be simplified by applying the so-called rotating wave approximation (RWA) which leads to removing all terms in (2.112) that have fast oscillating components ($2\omega t$ terms). The RWA Hamiltonian is

$$H_{\mathrm{RWA}}(\mathbf{r}) = \mu_B g_F \left(B_{\mathrm{s}}(\mathbf{r}) - \frac{\hbar\omega}{\mu_B g_F} \right) F_z + \mu_B g_f \left[\frac{B_{\mathrm{rf}_x}(\mathbf{r}) F_x + B_{\mathrm{rf}_y}(\mathbf{r}) F_y}{2} \right] . \tag{2.113}$$

As one can see from this equation, the time dependence has been removed. The next step in the procedure is to diagonalise the Hamiltonian, and hence obtain the adiabatic rf potentials, given by the eigenvalues. For this, the first step is to write the Hamiltonian in matrix form by using the basis vectors of $\mathbf{F}$. In this thesis we consider systems with total spin $F = \frac{1}{2}$, although this procedure can be generalised to multilevel systems with $F > \frac{1}{2}$. For $F = \frac{1}{2}$ the basis vectors are $|\frac{1}{2}, \frac{1}{2}\rangle$ and $|\frac{1}{2}, -\frac{1}{2}\rangle$ and therefore the components of $\mathbf{F}$ in matrix form are

$$F_x = \begin{pmatrix} 0 & \frac{1}{2} \\ \frac{1}{2} & 0 \end{pmatrix} , \tag{2.114}$$

$$F_y = \begin{pmatrix} 0 & -\frac{i}{2} \\ \frac{i}{2} & 0 \end{pmatrix} , \tag{2.115}$$

$$F_z = \begin{pmatrix} \frac{1}{2} & 0 \\ 0 & -\frac{1}{2} \end{pmatrix} . \tag{2.116}$$

By using these expressions, the Hamiltonian (2.113) can be written in matrix form,

$$H_{\mathrm{RWA}}(\mathbf{r}) = \mu_B g_F \frac{1}{2} \begin{pmatrix} B_{\mathrm{s}}(\mathbf{r}) - \hbar\omega & \frac{B_{\mathrm{rf}_x}(\mathbf{r}) - iB_{\mathrm{rf}_y}(\mathbf{r})}{2} \\ \frac{B_{\mathrm{rf}_x}(\mathbf{r}) + iB_{\mathrm{rf}_y}(\mathbf{r})}{2} & -B_{\mathrm{s}}(\mathbf{r}) + \hbar\omega \end{pmatrix} . \tag{2.117}$$

Since this is a simple 2x2 Hamiltonian, it can be analytically diagonalised and the eigenvalues are given by

$$E_{\pm}(\mathbf{r}) = \frac{\pm\mu_B g_F}{2} \sqrt{\left(B_{\mathrm{s}}(\mathbf{r}) - \frac{\hbar\omega}{\mu_B g_F} \right)^2 + \frac{1}{4} \left(B^2_{\mathrm{rf}_x}(\mathbf{r}) + B^2_{\mathrm{rf}_y}(\mathbf{r}) \right)} . \tag{2.118}$$

To highlight the basic form of these eigenergies, in Fig. 2.4 we show a one dimensional schematic of the bare trap eigenenergies of an atom confined to a linear static field, and the eigenergies when it is irradiated with a single rf field. As can be seen from this figure, the bare eigenstates are dressed by the rf field in such a way that an avoided crossing is produced where the rf field is resonant, i.e. the position at which $B_{\mathrm{s}}(\mathbf{r}) = \frac{\hbar\omega}{\mu_B g_F}$. As such, by adjusting the frequency of the rf field, it can be made to be resonant at any position, i.e. the rf field couples with spatial resolution.

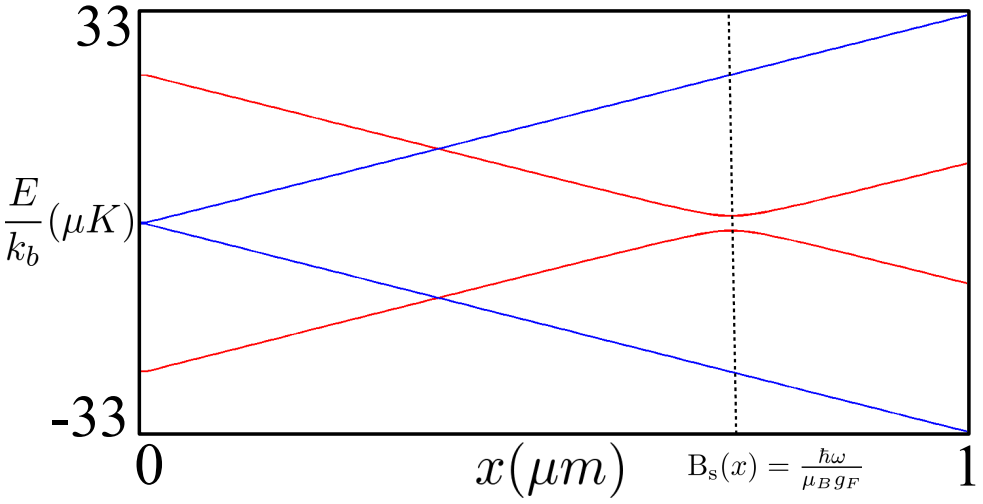

FIGURE 2.4: The eigenenergies obtained from equation (2.118) for an atom in a linear static field $\mathbf{B}_\mathrm{s}(x) = x$. The blue line shows the bare trap eigenenergies (no rf field) and the red line shows the eigenergies when the atom is irradiated with a single rf field of frequency $\omega = 2\pi \times 10\mathrm{kHz}$ with $B_{\mathrm{rf}_x}(x) = B_{\mathrm{rf}_y}(x) = 5 \times 10^{-8}\mathrm{T}$. The dotted line indicates the position the rf field is resonant with the bare eigenergies.

2.6.2.1 Multi-Frequency Potentials

To create multi-well potentials, as is required for the work in this thesis, it is necessary to use several frequencies making the above analysis significantly more complicated. In this Section we will detail the piecewise resonance approach to describing these multi-frequency adiabatic rf potentials.

The situations we will be considering here are where the frequencies of the rf fields are well separated and the Rabi frequencies are not too large. For such a situation, a good approach is to calculate the eigenvalues (2.118) for each rf field of frequency ω_n separately. For numerical simplicity, we will concentrate on a one dimensional description of such a process where the atom interacts with an inhomogeneous magnetic field $B_s = B(x)$ and the other two dimensions are tightly confined by a magnetic trap which the atom chip produces. We now define the Rabi frequency $\Omega(\mathbf{r})$,

$$\Omega(\mathbf{r}) = \frac{\mu_B g_F}{4\hbar}(B_{\mathrm{rf}_x}(\mathbf{r}) - iB_{\mathrm{rf}_y}(\mathbf{r}))\ , \tag{2.119}$$

which allows us to rewrite (2.117) as

$$H(x) = \frac{1}{2}\begin{pmatrix} \mu_B g_F B(x) - \hbar\omega & \hbar\Omega(x) \\ \hbar\Omega^*(x) & -\mu_B g_F B(x) + \hbar\omega \end{pmatrix}\ . \tag{2.120}$$

The approach to dealing with multiple frequencies here is to assume that the individual frequencies are spaced sufficiently far apart and have low Rabi frequencies with respect

to the detuning. In this case one can approximate the dynamics locally by considering only the nearest resonance frequency, $\omega(x) = \omega_n$ at any point in space [29]. Formally, this is done by choosing n such that $[\mu_B g_F B(x) - \hbar\omega_n]$ is minimized at any position x.

With this local frequency approximation the eigenvalues of Hamiltonian (2.120) can be approximated by making a second order Taylor expansion;

$$E_\pm(x) = \pm\frac{1}{2}\sqrt{\hbar^2\Omega^2(x) + [\mu_B g_F B(x) - \hbar\omega_n]^2} \tag{2.121}$$

$$\approx \pm\frac{1}{2}[\mu_B g_F B(x) - \hbar\omega_n] \pm \frac{\hbar^2\Omega^2(x)}{4[\mu_B g_F B(x) - \hbar\omega_n]} , \tag{2.122}$$

where the second expression is valid far from the resonance, $\hbar\Omega(x) \ll [\mu_B g_f B(x) - \hbar\omega_n]$. The second term in the expression can be viewed as a Stark shift on the energy levels. The effect of all other rf fields which are not closest to resonance can be approximated by creating an effective Stark shift which is the sum of the Stark shifts of all rf fields of frequency ω_j with $j \neq n$ [29]. The explicit form of this effective Stark shift is

$$L_n(x) = \sum_{j\neq n} \frac{\hbar^2\Omega^2(x)}{4[\mu_B g_F B(x) - \hbar\omega_{j(x)}]} . \tag{2.123}$$

Combining 2.120 and 2.123 gives

$$H(x) = \frac{1}{2}\begin{pmatrix} \mu_B g_F B(x) - \hbar\omega_{n(x)} - L_n(x) & \hbar\Omega(x) \\ \hbar\Omega(x) & -\mu_B g_F B(x) + \hbar\omega_{n(x)} + L_n(x) \end{pmatrix} , \tag{2.124}$$

and diagonalising this new Hamiltonian gives the corrected eigenvalues

$$E_\pm(x) = \pm\frac{1}{2}\sqrt{\hbar^2\Omega^2(x) + [\mu_B g_F B(x) - \hbar\omega + 2L_n(x)]^2} . \tag{2.125}$$

From this, and considering that the Rabi frequencies are strong enough so that each rf field flips the atoms spin where it is resonant, the resulting piecewise resonant, adiabatic potential is given by

$$V_{ad,\pm}(x) = (-1)^{n(x)}\left[E_\pm(x) \mp \frac{\hbar\omega_{n(x)}}{2}\right] \mp \sum_{k=1}^{n(x)-1}(-1)^k\hbar\omega_k . \tag{2.126}$$

Note that this expression for our adiabatic rf potentials gives us spatial resolution due to the spatial dependence of the magnetic field. We also see that we have two adiabatic potentials to choose from depending on the sign of the atom's spin $V_{ad,+}$ and $V_{ad,-}$.

2.6.3 Floquet Model

In this Section we detail the Floquet approach used in Chapter 5 to obtain the adiabatic eigenvalues of a system driven by multiple rf fields of different frequencies. Floquet theory, developed by Gaston Floquet [30], provides a practical and powerful non-perturbative method for studying the interaction of a quantum system with an oscillating field such as ionization and multiphoton excitation processes. It allows one to find the solutions of a Schrödinger equation with a temporally periodic Hamiltonian by representing it as an infinite matrix, the Floquet matrix. Therefore, one can utilise Flouqet theory to remove the time dependence from the generalised rf Hamiltonian (2.107) derived in Section 2.6.1.

The motivation for using Floquet theory for rf systems is that one is not required to apply the RWA which discards higher order coupling terms as was done in the piecewise resonance approach of the previous Section. In the RWA certain physical phenomena are not accounted for, with one prominent example being the Bloch-Siegert shift [60] which describes a shift in the resonance frequency due to the counter-rotating, fast oscillating terms. In [31], Floquet theory was used to derive expressions for the higher-order terms responsible for the Bloch-Siegert shift. Since we are interested in determining the transition frequencies exactly, we will take all oscillating terms into account with a Floquet approach and not make the RWA.

However, before we detail how to apply Floquet theory to the Hamiltonian (2.107), in the next Section we give an overview of the Floquet approach for a general periodic Hamiltonian.

2.6.3.1 Floquet Theory

In this Section we show how Floquet theory can be applied to a general Hamiltonian that is periodic in time. The Floquet theorem states that the time-dependent Schrödinger equation has a complete set of quasi-periodic solutions. These solutions, or quasi-eigenvalues, are found by diagonalising the Floquet matrix which can be thought of as a matrix whose elements consist of the Fourier components of the Hamiltonian.

First consider the time-dependent Schrödinger equation

$$i\hbar\frac{\partial\Psi(t)}{\partial t} = H(t)\Psi(t)\ , \tag{2.127}$$

where the Hamiltonian is periodic in time with frequency ω,

$$H(t) = H(t+\tau) = H\left(t + \frac{2\pi}{\omega}\right) . \tag{2.128}$$

The strategy for removing the time dependence from this Hamiltonian is to decompose it as a Fourier series,

$$H(t) = \sum_{m=-\infty}^{\infty} H_m e^{-im\omega t} , \tag{2.129}$$

and make the ansatz that the wave function can also be decomposed into a Fourier series,

$$\Psi(t) = \sum_{n=-\infty}^{\infty} \Phi_n(t) e^{-in\omega t} . \tag{2.130}$$

The next step is to obtain a Fourier representation of time-dependent Schrödinger equation. By inserting (2.130), into (2.127) one finds

$$i\hbar \sum_{n=-\infty}^{\infty} [\dot{\Phi}_n(t) - in\omega\Phi_n(t)]e^{-in\omega t} = H(t) \sum_{n=-\infty}^{\infty} \Phi_n(t) e^{-in\omega t} , \tag{2.131}$$

and replacing $H(t)$ with its Fourier representation (2.129) completes the Fourier decomposition of the Schrödinger equation,

$$i\hbar \sum_{n=-\infty}^{\infty} [\dot{\Phi}_n(t) - in\omega\Phi_n(t)]e^{-in\omega t} = \sum_{n,m=-\infty}^{\infty} H_m \Phi_n(t) e^{-i(n+m)\omega t} . \tag{2.132}$$

The next step of the procedure in obtaining the Floquet matrix is an exercise in rearranging and relabelling indices. First, by introducing $k = n+m$, the infinite sum on the right hand side of equation (2.132) can be rewritten as

$$\sum_{k,n=-\infty}^{\infty} H_{k-n} \Phi_n(t) e^{-ik\omega t} , \tag{2.133}$$

and relabelling the indices such that $k \to n$ and $n \to m$, the infinite sum (2.133) becomes,

$$\sum_{n,m=-\infty}^{\infty} H_{n-m} \Phi_m(t) e^{-in\omega t} . \tag{2.134}$$

Therefore, (2.132) can be written as

$$i\hbar \sum_{n=-\infty}^{\infty} [\dot{\Phi}_n(t) - in\omega\Phi_n(t)]e^{-in\omega t} = \sum_{n,m=\infty}^{\infty} H_{n-m} \Phi_m(t) e^{-in\omega t} . \tag{2.135}$$

This equation can now be simplified by cancelling the $e^{-in\omega t}$ terms on both sides

$$i\hbar\dot{\Phi}_n(t) + n\hbar\omega\Phi_n(t) = \sum_{m=-\infty}^{\infty} H_{n-m}\Phi_m(t) \;, \tag{2.136}$$

and rearranging it into a form similar to the Schrödinger equation where the time-dependent Hamiltonian has become an infinite dimensional static one

$$i\hbar\dot{\Phi}_n(t) = \sum_{m=-\infty}^{\infty} H_{n-m}\Phi_m(t) - n\hbar\omega\Phi_n(t) \tag{2.137}$$

$$= \sum_{m=-\infty}^{\infty} [H_{n-m} - n\hbar\omega\delta_{nm}]\Phi_n(t) \;. \tag{2.138}$$

As one can see from this expression, by carrying out this procedure the time-dependent Hamiltonian can be represented by a time-independent, infinite dimensional matrix. This is the so-called Floquet matrix H_F,

$$H_F = \sum_{m=-\infty}^{\infty} [H_{n-m} - n\hbar\omega\delta_{nm}] \;. \tag{2.139}$$

The explicit form of the Floquet matrix is

$$H_F = \begin{pmatrix} .. & .. & .. & .. & .. & .. & .. \\ .. & H_0 + 2\hbar\omega_1 & H_{-1} & H_{-2} & H_{-3} & H_{-4} & .. \\ .. & H_1 & H_0 + \hbar\omega_1 & H_{-1} & H_{-2} & H_{-3} & .. \\ .. & H_2 & H_1 & H_0 & H_{-1} & H_{-2} & ... \\ .. & H_3 & H_2 & H_1 & H_0 - \hbar\omega_1 & H_{-1} & .. \\ .. & H_4 & H_3 & H_2 & H_1 & H_0 - 2\hbar\omega_1 & .. \\ .. & .. & .. & .. & .. & .. & .. \end{pmatrix} \;, \tag{2.140}$$

where each Floquet *block* H_n is found by using

$$H_n = \frac{1}{\tau}\int_0^{\tau} H(t)e^{in\omega t}\,\mathrm{d}t \;, \tag{2.141}$$

and $\tau = \frac{2\pi}{\omega}$ is the period of the Hamiltonian [61]. By evaluating these integrals the Floquet blocks can be found and used to construct the Floquet matrix H_F (2.140). In the next Section, we will detail how the Floquet matrix is built for a system driven by a single rf field.

2.6.3.2 Single Frequency Floquet Matrix

In this Section we apply Floquet theory to remove the time dependence from the Hamiltonian (2.107), in the case where only a single rf field of frequency ω_1 is present. We do this as the construction of the Floquet matrix is quite involved for multiple frequencies and so dealing with a single rf field makes it easier to follow, while fully exemplifying the procedure. In the following Section we will then describe the procedure for dealing multiple rf fields.

For a single rf field of frequency ω_1, the Hamiltonian (2.107) reduces to

$$H(\mathbf{r},t) = \mu_B g_F \left\{ B_s(\mathbf{r}) F_z + \left[B_{1_x}(\mathbf{r}) \cos(\omega_1 t) \right] F_x + \left[B_{1_y}(\mathbf{r}) \cos(\omega_1 t) \right] F_y \right\} \ . \tag{2.142}$$

This Hamiltonian has a period of $\tau = \frac{2\pi}{\omega_1}$ and therefore can be mapped to a Floquet matrix to remove the time dependence. The quasi-eigenenergies of the Floquet matrix can then be used to construct the adiabatic rf potentials.

The first step in finding the Floquet matrix of the form (2.140) is to find each Floquet block H_n by using equation (2.141). Applying this to the Hamiltonian (2.142) produces,

$$\begin{aligned} H_n &= \frac{\mu_B g_F}{\tau} \int_0^\tau B_s(\mathbf{r}) e^{i(n\omega t)} F_z \, \mathrm{d}t + \\ &\quad \frac{\mu_B g_F}{\tau} \int_0^\tau F_x (B_{1x}(\mathbf{r}) \cos(\omega_1 t)) e^{i(n\omega t)} \, \mathrm{d}t + \\ &\quad \frac{\mu_B g_F}{\tau} \int_0^\tau F_y (B_{1y}(\mathbf{r}) \cos(\omega_1 t)) e^{i(n\omega t)} \, \mathrm{d}t \ . \end{aligned} \tag{2.143}$$

Using Euler's formula ($e^{i\alpha t} = \cos(\alpha t) + i \sin(\alpha t)$), $\cos(\omega_1 t)$ can be expressed in terms of exponentials,

$$\cos(\omega_1 t) = \frac{e^{i\omega_1 t} + e^{-i\omega_1 t}}{2} \ , \tag{2.144}$$

and with this expression, (2.143) can be written as

$$\begin{aligned} H_n &= \frac{\mu_B g_F}{\tau} \int_0^\tau B_s(\mathbf{r}) e^{i(n-0)} F_z \, \mathrm{d}t + \\ &\quad \frac{\mu_B g_F}{\tau} \int_0^\tau B_{1x}(\mathbf{r}) F_x \frac{e^{i(n-(-1))\omega_1 t} + e^{i(n-1)\omega_1 t}}{2} \, \mathrm{d}t + \\ &\quad \frac{\mu_B g_F}{\tau} \int_0^\tau B_{1y}(\mathbf{r}) F_y \frac{e^{i(n-(-1))\omega_1 t} + e^{i(n-1)\omega_1 t}}{2} \, \mathrm{d}t \ . \end{aligned} \tag{2.145}$$

These integrals may be evaluated by using the following identity [61],

$$\frac{1}{\tau} \int_0^\tau e^{i(n-m)\omega t} \mathrm{d}t = \delta_{nm} \ , \tag{2.146}$$

so that the evaluated Floquet blocks follow as

$$H_0 = \mu_B g_F B_s(\mathbf{r}) F_z \,, \tag{2.147a}$$

$$H_{+1} = \frac{\mu_B g_F B_{1x}(\mathbf{r}) F_x}{2} + \frac{\mu_B g_F B_{1y}(\mathbf{r}) F_y}{2} \,, \tag{2.147b}$$

$$H_{-1} = \frac{\mu_B g_F B_{1x}(\mathbf{r}) F_x}{2} + \frac{\mu_B g_F B_{1y}(\mathbf{r}) F_y}{2} \,, \tag{2.147c}$$

and all other H_n blocks are zero. These Floquet blocks can be rewritten in matrix form by using the basis vectors of $\mathbf{F}$ according to equations (2.114), (2.115) and (2.116) such that

$$H_0 = \frac{\mu_B g_F}{2} \begin{pmatrix} B_s(\mathbf{r}) & 0 \\ 0 & -B_s(\mathbf{r}) \end{pmatrix} \,, \tag{2.148a}$$

$$H_{+1} = \frac{\mu_B g_F}{2} \begin{pmatrix} 0 & \frac{B_{1x}(\mathbf{r}) - iB_{1y}(\mathbf{r})}{2} \\ \frac{B_{1x}(\mathbf{r}) + iB_{1y}(\mathbf{r})}{2} & 0 \end{pmatrix} \,, \tag{2.148b}$$

$$H_{-1} = \frac{\mu_B g_F}{2} \begin{pmatrix} 0 & \frac{B_{1x}(\mathbf{r}) - iB_{1y}(\mathbf{r})}{2} \\ \frac{B_{1x}(\mathbf{r}) + iB_{1y}(\mathbf{r})}{2} & 0 \end{pmatrix} \,. \tag{2.148c}$$

By using the previously defined Rabi frequency Ω (2.119), the Floquet blocks reduce to

$$H_0 = \frac{\mu_B g_F}{2} \begin{pmatrix} B_s(\mathbf{r}) & 0 \\ 0 & -B_s(\mathbf{r}) \end{pmatrix} \,, \tag{2.149}$$

$$H_{+1} = \begin{pmatrix} 0 & \hbar\Omega^*(\mathbf{r}) \\ \hbar\Omega(\mathbf{r}) & 0 \end{pmatrix} \,, \tag{2.150}$$

$$H_{-1} = \begin{pmatrix} 0 & \hbar\Omega^*(\mathbf{r}) \\ \hbar\Omega(\mathbf{r}) & 0 \end{pmatrix} \,. \tag{2.151}$$

Now that all the Floquet blocks H_n have been obtained, the Floquet matrix H_F can be constructed according to equation (2.140). Here, we show the infinite H_F matrix up to order $\hbar\omega_1$

$$H_F = \begin{pmatrix} \ddots & \vdots & \vdots & \vdots & \vdots & \vdots & \vdots & \iddots \\ \cdots & kB_s(\mathbf{r}) + \hbar\omega_1 & 0 & 0 & \hbar\Omega^*(\mathbf{r}) & 0 & 0 & \cdots \\ \cdots & 0 & -kB_s(\mathbf{r}) + \hbar\omega_1 & \hbar\Omega(\mathbf{r}) & 0 & 0 & 0 & \cdots \\ \cdots & 0 & \hbar\Omega^*(\mathbf{r}) & kB_s(\mathbf{r}) & 0 & 0 & \hbar\Omega^*(\mathbf{r}) & \cdots \\ \cdots & \hbar\Omega(\mathbf{r}) & 0 & 0 & -kB_s(\mathbf{r}) & \hbar\Omega(\mathbf{r}) & 0 & \cdots \\ \cdots & 0 & 0 & 0 & \hbar\Omega^*(\mathbf{r}) & kB_s(\mathbf{r}) - \hbar\omega_1 & 0 & \cdots \\ \cdots & 0 & 0 & \hbar\Omega(\mathbf{r}) & 0 & 0 & -kB_s(\mathbf{r}) - \hbar\omega_1 & \cdots \\ \iddots & \vdots & \vdots & \vdots & \vdots & \vdots & \vdots & \ddots \end{pmatrix} \,, \tag{2.152}$$

where $k = \frac{\mu_B g_F}{2}$.

Before the eigenvalues and eigenvectors of H_F can be found, the Floquet matrix must be truncated to a finite size, and a consistent way of doing this is to fix the number of

multiples of $\hbar\omega_1$ that are included. This corresponds to limiting the order of photonic processes that can occur. For example, if the Floquet matrix is limited to include terms up to $\pm 2\hbar\omega_1$, maximally two photons can be absorbed and emitted in a single process. As such, including higher orders leads to a more accurate description, but in real experiments, processes involving multiple photons are rare events. To demonstrate the effect, we choose to set $\hbar\omega_1$ as the highest multiple, which leads to

$$H_F = \begin{pmatrix} kB_s(\mathbf{r})+\hbar\omega_1 & 0 & 0 & \hbar\Omega^*(\mathbf{r}) & 0 & 0 \\ 0 & -kB_s(\mathbf{r})+\hbar\omega_1 & \hbar\Omega(\mathbf{r}) & 0 & 0 & 0 \\ 0 & \hbar\Omega^*(\mathbf{r}) & kB_s(\mathbf{r}) & 0 & 0 & \hbar\Omega^*(\mathbf{r}) \\ \hbar\Omega(\mathbf{r}) & 0 & 0 & -kB_s(\mathbf{r}) & \hbar\Omega(\mathbf{r}) & 0 \\ 0 & 0 & 0 & \hbar\Omega^*(\mathbf{r}) & kB_s(\mathbf{r})-\hbar\omega_1 & 0 \\ 0 & 0 & \hbar\Omega(\mathbf{r}) & 0 & 0 & -kB_s(\mathbf{r})-\hbar\omega_1 \end{pmatrix} . \tag{2.153}$$

Diagonalisation of this matrix leads to the quasi-energy spectrum, which in turn allows the calculation the adiabatic rf potential. The manuscript presented in Chapter 5 details this process further.

2.6.3.3 Multi Frequency Floquet Matrix

In this Section we will consider the Hamiltonian (2.107) when several rf fields are present. This situation can be treated using Many Mode Floquet Theory (MMFT) and a detailed explanation of it can be found in [62]. Here, we will explicitly demonstrate the procedure for two different frequencies, ω_1 and ω_2, for which the Hamiltonian is given by

$$\begin{aligned} H(\mathbf{r},t) = \mu_B g_F \Big[& B_s(\mathbf{r})F_z + \left(B_{1_x}(\mathbf{r})\cos(\omega_1 t) + B_{2_x}(\mathbf{r})\cos(\omega_2 t)\right) F_x \\ & + \left(B_{1_y}(\mathbf{r})\cos(\omega_1 t) + B_{2_y}(\mathbf{r})\cos(\omega_2 t)\right) F_y \Big] . \end{aligned} \tag{2.154}$$

As the explicit form of the multi-frequency Floquet matrix for a general periodic Hamiltonian is quite large and complicated, it will not be presented here, but can be found in [62]. Instead, we show the particular form of the Floquet matrix for the Hamiltonian (2.154). However, this multi-frequency Floquet matrix is still significantly more complicated than the single frequency case, but can be made more manageable by considering separate component matrices that are combined to make the full Floquet matrix. There are two main component matrices which we label A, P. These matrices have their own component matrices which we label Z, X (the components of A) and Y (the component

of P). With this labelling system the total Floquet matrix can be written as

$$H_F^{(2)} = \begin{pmatrix} .. & .. & .. & .. & .. & .. & .. \\ .. & A+2\hbar\omega_r I & P & 0 & 0 & 0 & .. \\ .. & P^T & A+\hbar\omega_r I & P & 0 & 0 & .. \\ .. & 0 & P^T & A & P & 0 & .. \\ .. & 0 & 0 & P^T & A-\omega_r I & P & .. \\ .. & 0 & 0 & 0 & P^T & A-2\hbar\omega_r & .. \\ .. & .. & .. & .. & .. & .. & .. \end{pmatrix}, \tag{2.155}$$

where $\omega_r = \omega_1 + \omega_2$ and I is the identity matrix. To understand why ω_r is used instead of ω_2, consider the energy spectrum of the effective field created by the static field and the first frequency ω_1. When this first frequency is applied, the position of zero in the energy spectrum is shifted from its position when just the static field is present. When the second frequency is applied, it is applied to this effective field. Therefore the point at which it couples is shifted to where $\omega_1 + \omega_2$ is resonant. This is the so-called dressed state picture.

$H_F^{(2)}$ can be thought of as a composite matrix of two single frequency Floquet matrices. The ω_1 frequency terms and the Rabi frequency of the first field $\Omega_1(\mathbf{r})$ are contained in matrix A, which is the same matrix as H_F (2.152) in the previous Section. The off diagonal elements P contain $\Omega_2(\mathbf{r})$, the Rabi frequency associated with the second rf field of frequency ω_2.

We now present both A and P, starting with A whose components depend only on terms from the first rf field of frequency ω_1,

$$A = \begin{pmatrix} .. & .. & .. & . & .. & .. & .. \\ .. & Z+2\hbar\omega_1 I & X & 0 & 0 & 0 & .. \\ .. & X & Z+\hbar\omega_1 I & X & 0 & 0 & .. \\ .. & 0 & X & Z & X & 0 & .. \\ .. & 0 & 0 & X & Z-\hbar\omega_1 I & X & .. \\ .. & 0 & 0 & 0 & X & Z-2\hbar\omega_1 I & .. \\ .. & .. & .. & . & .. & .. & .. \end{pmatrix}, \tag{2.156}$$

where X and Z, the components of A, are defined as

$$Z = \begin{pmatrix} kB_s(\mathbf{r}) & 0 \\ 0 & -kB_s(\mathbf{r}) \end{pmatrix}, \tag{2.157}$$

$$X = \begin{pmatrix} 0 & \hbar\Omega_1^*(\mathbf{r}) \\ \hbar\Omega_1(\mathbf{r}) & 0 \end{pmatrix} , \tag{2.158}$$

and $\Omega_1(\mathbf{r}) = \frac{\mu_B g_F}{4\hbar}(B_{1_x}(\mathbf{r}) + iB_{1_y}(\mathbf{r}))$ is the Rabi frequency of the first rf field. We note that matrix Z contains just the eigenvalues of the bare Hamiltonian (no rf field) and corresponds to H_0 from the previous Section. Similarly, the matrix X corresponds to $H_{\pm 1}$, the off diagonal terms of the Floquet matrix from previous Section. With Z and X now defined, matrix A can be written as

$$A = \begin{pmatrix} .. & .. & .. & .. & .. & .. & .. \\ .. & kB_s(\mathbf{r})+2\hbar\omega_1 & 0 & 0 & \hbar\Omega_1^*(\mathbf{r}) & 0 & .. \\ .. & 0 & -kB_s(\mathbf{r})+2\hbar\omega_1 & \hbar\Omega_1(\mathbf{r}) & 0 & 0 & .. \\ .. & 0 & \hbar\Omega_1^*(\mathbf{r}) & kB_s(\mathbf{r})+\hbar\omega_1 & 0 & 0 & .. \\ .. & \hbar\Omega_1(\mathbf{r}) & 0 & 0 & -kB_s(\mathbf{r})+\hbar\omega_1 & \hbar\Omega_1(\mathbf{r}) & .. \\ .. & 0 & 0 & 0 & \hbar\Omega_1^*(\mathbf{r}) & kB_s(\mathbf{r}) & .. \\ .. & 0 & 0 & \hbar\Omega_1(\mathbf{r}) & 0 & 0 & .. \\ .. & .. & .. & .. & .. & .. & .. \end{pmatrix} . \tag{2.159}$$

The last component that is required in order to produce the multi-frequency Floquet matrix $H_F^{(2)}$, is P which is defined as

$$P = \begin{pmatrix} .. & .. & .. & .. & .. & .. & .. \\ .. & 0 & Y & 0 & 0 & 0 & .. \\ .. & 0 & 0 & Y & 0 & 0 & .. \\ .. & 0 & 0 & 0 & Y & 0 & .. \\ .. & 0 & 0 & 0 & 0 & Y & .. \\ .. & 0 & 0 & 0 & 0 & 0 & .. \\ .. & .. & .. & .. & .. & .. & .. \end{pmatrix} , \tag{2.160}$$

where the only non-zero component Y contains the coupling terms introduced by the rf field with frequency ω_2,

$$Y = \begin{pmatrix} 0 & \Omega_2^*(\mathbf{r}) \\ \Omega_2(\mathbf{r}) & 0 \end{pmatrix} , \tag{2.161}$$

and $\Omega_2(\mathbf{r}) = \frac{\mu_B g_F}{4\hbar}(B_{2_x}(\mathbf{r}) + iB_{2_y}(\mathbf{r}))$ is the Rabi frequency of the second rf field. It is now straightforward to write down the matrix P

$$P = \begin{pmatrix} .. & .. & .. & .. & .. & .. & .. & .. \\ .. & 0 & 0 & 0 & \hbar\Omega_2^*(\mathbf{r}) & 0 & 0 & .. \\ .. & 0 & 0 & \hbar\Omega_2(\mathbf{r}) & 0 & 0 & 0 & .. \\ .. & 0 & 0 & 0 & 0 & 0 & \hbar\Omega_2^*(\mathbf{r}) & .. \\ .. & 0 & 0 & 0 & 0 & \hbar\Omega_2(\mathbf{r}) & 0 & .. \\ .. & 0 & 0 & 0 & 0 & 0 & 0 & .. \\ .. & 0 & 0 & 0 & 0 & 0 & 0 & .. \\ .. & .. & .. & .. & .. & .. & .. & .. \end{pmatrix} . \tag{2.162}$$

By combining both A and P according to equation (2.155), one can produce the desired Floquet matrix H_f. This matrix is very large so we only present a subsection of it here to highlight its basic structure,

$$H_f = \begin{pmatrix} \ddots & \ddots & \ddots & \ddots & \ddots & \ddots & \ddots & \ddots \\ \cdots & kB_S(\mathbf{r})+\hbar\omega_1+\hbar\omega_r & 0 & 0 & \hbar\Omega_1^*(\mathbf{r}) & 0 & 0 & \cdots \\ \cdots & 0 & -kB_S(\mathbf{r})+\hbar\omega_1+\hbar\omega_r & \hbar\Omega_1(\mathbf{r}) & 0 & 0 & 0 & \cdots \\ \cdots & 0 & \hbar\Omega_1^*(\mathbf{r}) & kB_S(\mathbf{r})+\hbar\omega_r & 0 & 0 & \hbar\Omega_1^*(\mathbf{r}) & \cdots \\ \cdots & \hbar\Omega_1(\mathbf{r}) & 0 & 0 & -kB_S(\mathbf{r})+\hbar\omega_r & \hbar\Omega_1(\mathbf{r}) & 0 & \cdots \\ \cdots & 0 & 0 & 0 & \hbar\Omega_1^*(\mathbf{r}) & kB_S(\mathbf{r})-\hbar\omega_1+\hbar\omega_r & 0 & \cdots \\ \cdots & 0 & 0 & \hbar\Omega_1(\mathbf{r}) & 0 & 0 & -kB_S(\mathbf{r})-\hbar\omega_1+\hbar\omega_r & \cdots \\ \cdots & 0 & 0 & 0 & \hbar\Omega_2^*(\mathbf{r}) & 0 & 0 & \cdots \\ \cdots & 0 & 0 & \hbar\Omega_2(\mathbf{r}) & 0 & 0 & 0 & \cdots \\ \ddots & \ddots & \ddots & \ddots & \ddots & \ddots & \ddots & \ddots \end{pmatrix} . \quad (2.163)$$

The key points about the structure of this Floquet matrix are that the bare trap eigenenergies are given along the diagonal and each Floquet block differs by multiples of both ω_1 and ω_r. The off-diagonal terms correspond to the coupling strengths and contain terms for both $\Omega_1(\mathbf{r})$ and $\Omega_2(\mathbf{r})$, the Rabi frequency associated with the first and the second frequency respectively. Like the single frequency Floquet matrix (2.153), truncation and diagonalisation of this Floquet matrix produces a quasi-eigenenergy spectrum from which the adiabatic rf potential can be extracted. This procedure is detailed in the manuscript presented in Chapter 5.

2.7 Solitons

In this Section we give a brief overview of solitons, the focus of Chapter 6. Solitons are localised wavepackets that exist in many different areas of physics such as non-linear optics [34] and hydrodynamics [35], where a non-linearity present in the system can compensate for the dispersion of the wavepacket. As a result of this balance, solitons have the property that they can propagate without dispersion. They also emerge from collisions with other solitons unchanged (expect for a phase change). As the previously derived time-dependent Gross-Pitaevskii equation (2.17) contains such a non-linear term, soliton solutions can be found [63, 64].

Strictly speaking, proper mathematical and stable soliton solutions to the Gross-Pitaevskii equation (GPE) exist only in 1D and in the case where it is completely integrable [43]. Physically, this means that the condensate is completely homogeneous and there is no external potential. In such a situation, the GPE (2.17) reduces to

$$i\hbar\frac{d\psi(z,t)}{dt} = \left[-\frac{\hbar^2}{2m}\nabla^2 + gN|\psi(z,t)|^2\right]\psi(z,t) \, , \quad (2.164)$$

where $g = \frac{4\pi\hbar^2 a_s}{m}$ with m and a_s the mass and s-wave scattering length respectively. Different kinds of soliton solutions exist depending on the sign of the interaction term

g, i.e whether the interaction is repulsive or attractive. Here we will focus on repulsive interactions ($g > 0$). The soliton solutions to the GPE were first derived in the 1970's [65] and give the general form of the wave function of a soliton with speed v on a homogeneous background density $n = |\psi|^2$ [43],

$$\psi(z - vt, t) = \sqrt{n} e^{-i\mu t/\hbar} \left[\sqrt{1 - \left(\frac{v}{c}\right)^2} \tanh\left(\sqrt{1 - \left(\frac{v}{c}\right)^2} \frac{z - vt}{\xi} \right) + i\frac{v}{c} \right] , \quad (2.165)$$

where $c = ng/m$ is the Bogoliubov speed of sound, $\xi = \frac{\hbar}{2mgn}$ is the healing length of the condensate and μ is the chemical potential. The density of the soliton wave function predicts a minimum for $z = vt$,

$$|\psi(0, t)|^2 = \frac{nv^2}{c^2} . \quad (2.166)$$

The wave function also undergoes a phase change $\Delta\Theta$ as z varies from $-\infty$ to $+\infty$ of

$$\Delta\Theta = 2 \arccos\left(\frac{v}{c}\right) . \quad (2.167)$$

For a stationary soliton ($v = 0$), this equation predicts a phase change of $\Delta\Theta = \pi$ and equation (2.166) gives $|\psi(0, t)|^2 = 0$, zero density at the centre of the soliton. This is the so called dark soliton and the blue line in Fig. 2.5 shows its density and phase profile. While a dark soliton is stationary and has a zero density depression, the velocity of a non-stationary soliton is intrinsically linked to the depth of the minimum density such that

$$v = c\sqrt{1 - n_d/n} , \quad (2.168)$$

where n_d is the depth of the density depression. From this expression one can see that, as the velocity of the soliton increases towards the maximum value set by the Bogoliubov speed of sound c, the depth of the density depression of the soliton decreases. Such a filled in dark soliton is called a grey soliton and Fig. 2.5 (except the blue line) shows the density and phase of grey solitons with various velocities.

Dark solitons created in an inhomogeneous background are stationary. However, in [40] it was shown that dark solitons are not stable and possess a dynamical instability that leads them to pick up velocity and turn grey. If the inhomogeneous background stems from harmonic trapping, the soliton will oscillate back and forth in the trap with a frequency given by

$$\omega_S = \frac{\omega_H}{\sqrt{2}} , \quad (2.169)$$

where ω_H is the frequency of the harmonic oscillator.

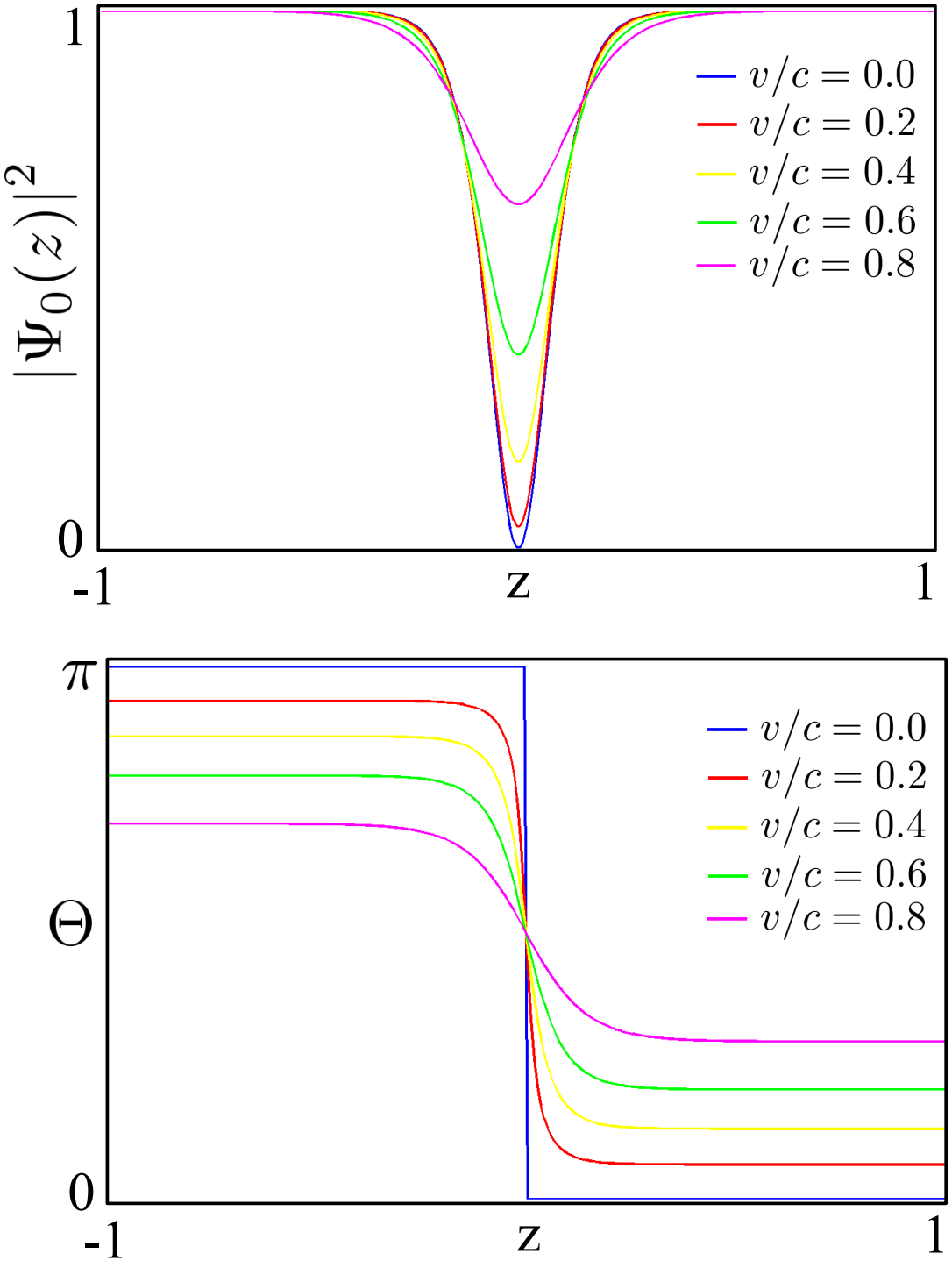

FIGURE 2.5: Density (upper panel) and phase (lower panel) of solitons with increasing velocity v.

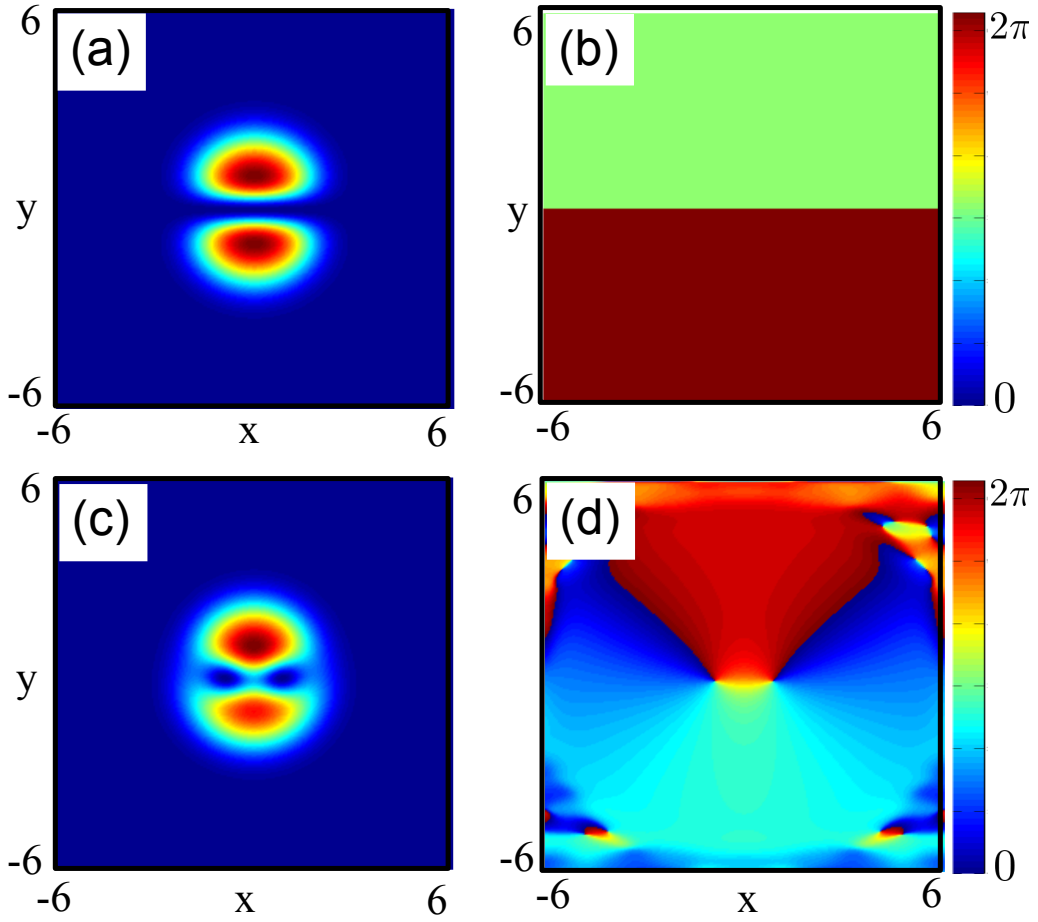

FIGURE 2.6: The density (a) and phase (b) of a dark soliton at $t = 0$. The density (c) and phase (d) of the dark soliton once the snake instability has set in.

2.7.1 Solitons in Higher Dimensions

As previously stated, strict mathematical and stable soliton solutions for the GPE exist only in one dimension and for no external trapping potential. However, solitons can be embedded in 2D and 3D systems with or without external potentials where, unlike their 1D counterparts, one finds that they are no longer stable [66–68]. In Chapter 6 of this thesis, we focus on a system of 2D dark solitons in a BEC which is confined in a tight harmonic potential and study its instabilities. To numerically create a dark soliton in such a system, we simply enforce a phase difference of π between two different spatial regions of the wave function which allows us to numerically find the ground state with the characteristic density in 2D. Figs. 2.6 (a) and (b) show the density and phase of a single dark soliton that results from this process.

The basic instability of a single dark soliton in two dimensions is to eventually decay

into a number of quantized vortices through what is called the *snake instability* [66, 69]. This instability causes the soliton to bend (or *snake*) along the direction of the density minimum until the curvature is large enough to lead to a break up into vortex-antivortex pairs. Figs. 2.6 (c) and (d) show an example of this process.

The instabilities of solitons may be studied by using the Bogoliubov-de Gennes equations (2.31) as discussed in Section 2.2. The Bogoliubov spectrum of eigenvalues produced by diagonalising (2.31) for the dark soliton shown in Figs. 2.6 (a) and (b) reveals the existence of a single, purely imaginary eigenfrequency and an associated eigenvector. This unstable mode is responsible for the snake instability.

In inhomogeneous systems however, the snake instability can be suppressed. In [66] the authors examined the Bogoliubov spectrum of eigenfrequencies of a single dark soliton of constant density confined to a square trap. They found that the Bogoliubov spectrum could be made completely real when the dimensions of the trap were reduced in size. At this point the soliton is completely stable, which can be intuitively understood by considering that the transversal width of the soliton is made so short that it no-longer supports even the lowest mode of the snake instability.

By working in this regime, in Chapter 6 we numerically create a family of multidimensional solitons which exhibit interesting instabilities which cannot be related to the snake instability.

Chapter 3

Coherent Tunnelling by Adiabatic Passage in Atom Chip Systems

As mentioned in Chapter 2, Coherent Tunnelling by Adiabatic Passage (CTAP) is the atom-optical analogue of the optical STIRAP technique and was first introduced in 2004 by Eckert *et al.* [20]. They showed that the CTAP process offers a way of coherently transporting the centre-of-mass state of a single atom between two traps and also showed how the fidelity of the process is affected by various system parameters. However, the suggested trapping potential of three-line dipole traps was modelled as three piece-wise harmonic potentials and the influence that each trap would have on each other was neglected. As such, this treatment is not experimentally realistic. Many other studies involving CTAP since then have made similar approximations [21, 24, 70].

In the two manuscripts presented in this Chapter, we theoretically show how the CTAP technique can be used to coherently transport the centre-mass-state of a single cold atom between two spatially distinct magnetic waveguides created on an atom chip for experimentally realistic parameters. [1] The trapping potentials created by the current carrying wires on the atom chip are treated realistically without any of the approximations made by previously mentioned works. As such, this system is a good candidate for experimental verification of CTAP, which has up to now only been achieved in a classical wave optics analogue [71].

CTAP has also found a large number of applications beyond that of the coherent transport of atoms, for which it was originally suggested. Notable examples of such applications are filtering out unwanted vibrational states [70], atomtronics [72], electron transfer

[1] The work in the first manuscript was done in collaboration with Brian O'Sullivan and Padraic Morrissey. Each author contributed to all areas of the manuscript. The work in the second manuscript was done in collaboration with Lee O'Riordan, Neil Crowley and Brian O'Sullivan. Each author contributed to all areas of the manuscript.

in quantum dots [23, 73–75], CNOT gates [76], electron transport in triple donor systems [77] and adiabatic passage of light [71, 78]. Recent work has also focused on speeding up CTAP through optimal control techniques [79] and on performing interferometry of BECs [80].

The atom chip system which we propose in this Chapter has been widely used by experimentalists around the world for some time and a general review of their uses and properties can be found in [25]. Highlights of recent work with atom chips include guiding neutral atoms [81], manipulation of BECs [82], matter-wave interferometry [28], multi-state interferometry [83], studying correlations in isolated quantum systems [84], quantum gates [85–87], suppressing roughness in atom chip potentials [88], creation of adiabatic radio frequency potentials [89] and integration of optical elements [90].

In the second manuscript presented in this Chapter, we make use of graphics processing unit (GPU) computing to numerically solve the Schrödinger equation in three dimensions. The performance increase offered by GPU computing allows the simulations of the atom chip system to be numerically tractable on a consumer desktop computer. GPU computing is a relatively recent development in computational physics and there has been significant progress in its general applications to numerical problems such as the solving the Schrödinger [91–93], the Boltzmann equation [94] and to more specific systems such as descriptions of electrical potentials in Hall devices [95] and spin systems [96].

3.1 Using Adiabatic Coupling Techniques in Atom Chip Waveguide Structures

Manuscript Information

Manuscript Title: Using adiabatic coupling techniques in atom-chip waveguide structures.

Journal Information: Physica Scripta, **T140** 014029 (2010).

Authors: Brian O'Sullivan, Padraic Morrissey, Tadhg Morgan and Thomas Busch.

Pages: 6.

Figures: 6.

Phys. Scr. **T140** (2010) 014029 (6pp) doi:10.1088/0031-8949/2010/T140/014029

Using adiabatic coupling techniques in atom-chip waveguide structures

B O'Sullivan, P Morrissey, T Morgan and Th Busch

Physics Department, University College Cork, Cork, Ireland

E-mail: bosullivan@phys.ucc.ie

Received 29 March 2010
Accepted for publication 15 June 2010
Published 30 September 2010
Online at stacks.iop.org/PhysScr/T140/014029

Abstract
Adiabatic techniques are well-known tools in multi-level electron systems to transfer population between different states with high fidelity. Recently, it has been realized that these ideas can also be used in ultracold atom systems to achieve coherent manipulation of the atomic centre-of-mass states. Here, we present an investigation into a realistic setup using three atomic waveguides created on top of an atom chip and show that such systems hold great potential for the observation of adiabatic phenomena in experiments.

PACS numbers: 03.67.−a, 03.67.Mn, 03.75.Lm

(Some figures in this article are in colour only in the electronic version.)

1. Introduction

Trapping and controlling small numbers of neutral atoms has, in recent years, emerged as one of the most active and productive areas in physics research [1–4]. Such systems allow us to perform experiments to answer fundamental questions in quantum mechanics [5, 6] and hold great potential for use in quantum information processing [7–9]. Advances in the technology of optical lattices and micro-traps have allowed for substantial progress in this area [10–14] and various concepts have been developed to prepare and process the states of single atoms. While techniques for controlling and preparing the internal states of atoms using appropriate electromagnetic fields are well developed, only a few concepts exist for achieving the same control over the spatial part of a wavefunction [8, 15–18]. Such control would complement currently existing techniques and allow for the complete engineering of a particle's quantum state.

One area where control over the spatial part of the wavefunction is important is the challenge of devising techniques for the controlled movement of atoms between different regions in space. In optical lattices this corresponds to moving between discrete lattice sites, and in waveguide settings this would allow transfer from one guide to another. Direct tunnelling is a coherent process that can achieve this; however, Rabi-type oscillations make it experimentally very hard to reach high fidelities [19].

Recently, it was pointed out that systems consisting of three separated centre-of-mass modes allow for the use of STIRAP-like processes to achieve robust transfer of atoms from one position to another with high fidelity [16, 17, 20]. The process of stimulated Raman adiabatic passage (STIRAP) is well known in three-level-optics, where it refers to the technique of applying a counter-intuitive sequence of laser pulses to achieve a transition of an electron between the two ground states in a Λ-system [21, 22]. In the atom trap scenario, the energy levels are replaced by spatially separated trap ground states and the laser interaction is replaced by the coherent tunnelling interaction.

One advantage of adiabatic techniques is their large robustness against experimental uncertainties as long as the whole process is carried out mostly adiabatically [23]. However, this also means that a resonance between the asymptotic eigenstates has to exist, which is a condition that for many realistic situations is hard to ensure. Suggestions for and examinations of realistic systems in which the STIRAP process could be observed for cold atomic gases are therefore currently very rare.

In this work, we will focus on atom-chip systems and investigate their suitability to observe this adiabatic process. These micro-fabricated chips, on which surface-mounted, current carrying wires provide guiding potentials for matter waves, can be loaded with ultracold atom gases at low densities. As opposed to traditional experimental setups, these systems allow reaching smaller dimensions, and wire geometry, and therefore waveguide geometry, can be chosen almost at will [24].

The first investigation into adiabatic techniques in waveguides was presented by Eckert *et al* [17], who showed that a CPT-like process that acts like a 50 : 50 beam splitter could be realized with a large degree of fidelity. While the initial state for a numerical evolution can be prepared with a large degree of localization, one of the problems following subsequent evolution inside the waveguide is that the wavefunction disperses along the guide. This makes it hard to exactly measure the final state of the system and put a quantitative number on the efficiency of the adiabatic process. Here we will introduce a simple harmonic potential along the longitudinal direction of the trap, which will allow us to perfectly measure the fidelity of the process. It is also worth mentioning that STIRAP in optical waveguides with classical light has been observed recently [25].

In the next section, we will first briefly review the idea of STIRAP and its translation into the realm of waveguides. After that, in section 3, we will examine a model waveguide potential in which the resonance condition is fulfilled throughout the whole process and show that the dispersion of the wavefunction in the longitudinal direction has no significant effect on the fidelity of the process. In section 4, we describe a realistic situation by examining three waveguides created on top of an atom chip. We show that even though the resonance condition is not fulfilled at all times, a counter-intuitive approach will lead to larger transfer and can clearly be distinguished from a direct tunnelling approach. Finally, we conclude.

2. STIRAP

In this section, we will briefly review the basic idea of STIRAP, which is a technique originally developed for transitions in optical λ-systems and makes use of a two-photon Raman process. By applying the pump and the Stokes pulse in a counter-intuitive time-ordered way, it leads to population transfer directly from one of the ground states to the other without any population ever being in the excited transitional state. In optical systems, this inhibits spontaneous emission and is therefore often referred to as a dark-state technique.

The basic idea can be understood in the simple model of a three-state system described by the Hamiltonian

$$H(t) = \hbar \begin{pmatrix} 0 & -\Omega_{\mathrm{P}}(t) & 0 \\ -\Omega_{\mathrm{P}}(t) & 0 & -\Omega_{\mathrm{S}}(t) \\ 0 & -\Omega_{\mathrm{S}}(t) & 0 \end{pmatrix}, \qquad (1)$$

where we have set the energies of the three asymptotic eigenstates to zero and the Rabi frequencies of the pump and the Stokes pulses are given by Ω_{P} and Ω_{S}, respectively. This Hamiltonian can be diagonalized and the eigenstate that is of interest to us here is the so-called dark state given by

$$|d\rangle = \cos\theta|1\rangle - \sin\theta|3\rangle\,, \qquad (2)$$

where the mixing angle θ is given by $\tan\theta = \Omega_{\mathrm{P}}/\Omega_{\mathrm{S}}$. This angle describes how the population is distributed between the two states $|1\rangle$ and $|3\rangle$ and it can be chosen by varying the strength of the pump and the Stokes pulse with respect to each other in time. In particular, if the intensity of the Stokes pulse increases before that of the pump pulse (counter-intuitive coupling scheme), one finds that all the initial population in $|1\rangle$ will be transferred to $|3\rangle$.

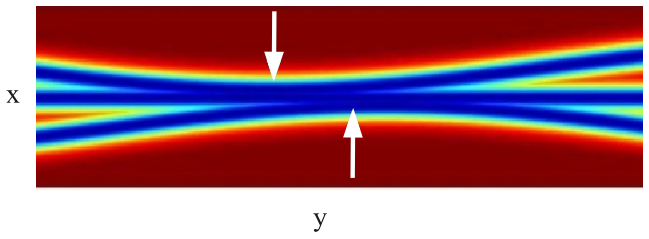

Figure 1. Waveguide structure near the point of closest approach. The points where the upper and lower waveguides have a minimum distance from the central waveguide are indicated by the arrows. The wavepacket will originally travel in the lowest waveguide from left to right.

The fact that this process can be observed for trapped atoms was first pointed out by Eckert *et al* [16]. The asymptotic eigenstates of the Hamiltonian (1) are then the spatial modes the atoms occupy and the time-dependent coupling is given by the tunnelling strength between these modes. While the time dependence of the tunnelling strength can be achieved by temporally changing the distance or the barrier height between the individual states, an atom moving in a waveguide can also experience this as a function of travelled distance [17]. In the next section, we will examine an example of this.

3. Model

The Schrödinger equation for the evolution of a wavepacket in a two-dimensional (2D) waveguide structure is given by

$$\mathrm{i}\dot{\psi}(x, y) = -\frac{\hbar^2}{2m}\nabla^2\psi(x, y) + V(x, y)\psi(x, y), \qquad (3)$$

where m is the mass of the atom. As the third dimension does not significantly contribute to the dynamics we are aiming to observe, the restriction of the above Hamiltonian to two dimensions is justified. In this section, we will first examine the STIRAP process using an idealized potential in which the condition of resonance between the individual waveguides is fulfilled at any point. This will help us to illustrate the basic process and in particular highlight the influence of the longitudinal dimension. In section 4, we will compare these results to realistic atom-chip scenarios in which we will have to relax the resonance condition.

The assumption we make to guarantee that the ground state energy in all three waveguides is the same everywhere is that we can construct our potential $V(x, y)$ by stitching three independent waveguides together. In a realistic situation, the potentials creating each guide would influence each other and lead to non-symmetric situations between pairs. We assume each guide to have the potential

$$V_{\mathrm{s}} = A\tanh[B(x - f(y))]^2, \qquad (4)$$

where A determines the height, B the width and $f(y)$ the position of the minimum along the x-axis. The overall

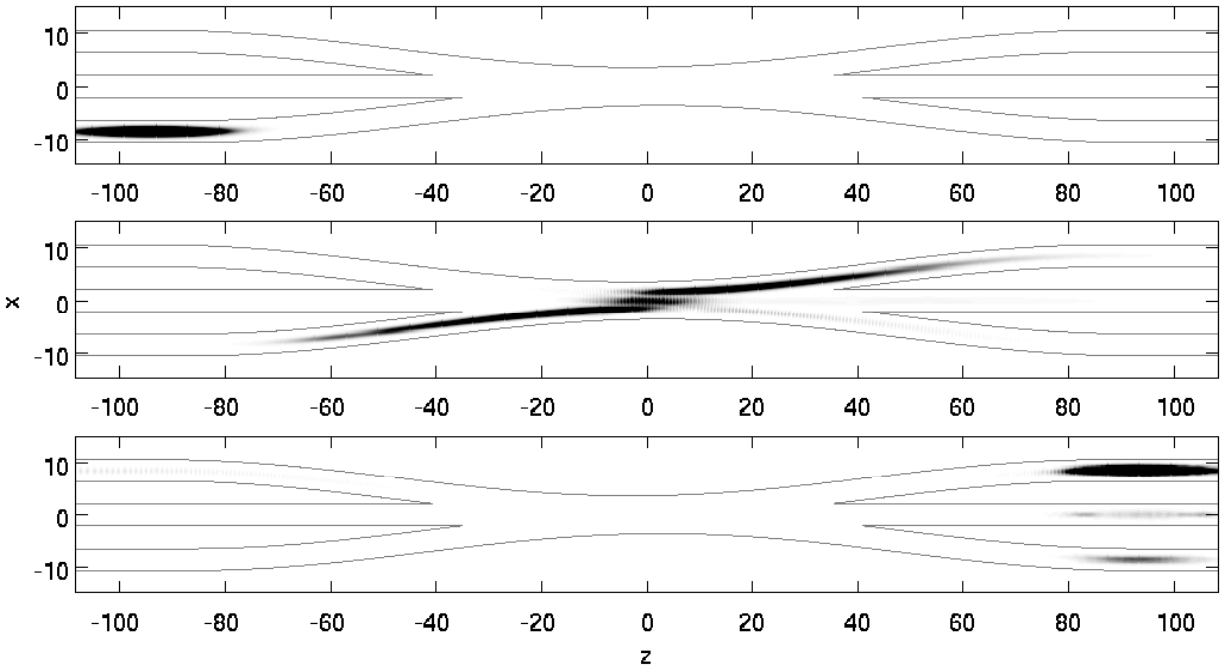

Figure 2. Time evolution of the wavepacket in a counter-intuitive arrangement of the waveguides at three different times for values of $A = 20$ and $B = 0.5$. The shapes of the waveguides are indicated by the black lines and they are fully separated at the energy of the wavepacket in the coupling zone (not visible).

potential is then assumed to be given by the minimum value of each of the three potentials at any point in space. A schematic view of the area in which the guides approach most closely is shown in figure 1.

The eigenstates of matter waves propagating in 2D waveguides at different distances have recently been explored by Jääskeläinen and Stenholm [26]. They determined the conditions under which the movement of a matter wave can be considered adiabatic in a curved waveguide and developed a formalism based on localized and de-localized basis states. Here we will take a more straightforward approach and present a numerical solution to the process, which will show that despite the existence of velocity-dependent potentials due to the curvature of the waveguides [26] the STIRAP process can be observed with high fidelity.

Our simulations start with a well-localized wavepacket far from the coupling area. In time, however, this packet will disperse along the waveguide, making it hard to quantify the success of the transfer process. To overcome this problem, we introduce an additional harmonic potential of frequency ω_l along the y-axis, which will lead to a refocusing of the wavepacket in the longitudinal direction after a time of $\omega_l/2$. The initial state of our wavepacket is given by the ground state of an isotropic trap of the transverse frequency of the waveguide and its movement along the guide is induced by the harmonic potential as well.

In figure 2 we show the evolution of the wavefunction at different times throughout the process for a counter-intuitive arrangement of the waveguides. Starting with the wavepacket located in the lower guide, one can clearly see that a majority of the probability is transferred into the upper guide. The evolution of the same initial state in an intuitive arrangement of waveguides (see figure 2) shows significantly less transfer.

The amount of transfer varies as a function of several parameters. The first one is the distance between the two points of closest approach of the outer waveguides to the middle one, Δz. We show the amount transferred as a function of this quantity in figure 4 on the left-hand side. The full line (blue) represents the counter-intuitive case and a maximum at a finite value of Δz is visible. The broken line shows the same quantity for the intuitive setting, clearly indicating that direct tunnelling does not lead to high fidelities.

The second parameter that plays an important role is the degree of adiabaticity of the process. For a waveguide system, this translates into the velocity with which the atom moves or alternatively the length of the coupling area. Here, we keep the velocity effectively constant and show on the right-hand side of figure 4 the variation of the maximum amount transferred as a function of the overall length of the coupling area. Making the overall structure longer also corresponds to decreasing the curvature of the waveguides, thereby reducing the velocity-dependent couplings introduced by it [26]. As expected, we find that a more adiabatic process leads to a larger transfer probability.

Two caveats have to be pointed out with respect to the above simulations. While our calculations are carried out with the atom in the ground state in the transversal direction, this is not a necessary condition. In fact, the process will work for any state for which three degenerate asymptotic states exist. This in particular includes states of higher energy.

Secondly, our simulations are carried out only for the linear case of a single atom. If one would like to carry out the same process using, say, a Bose–Einstein condensate, one has to take care of the nonlinearity that arises from the atomic interactions. However, we believe that our simulations give a very good approximation for low-density condensates or even thermal clouds of atoms.

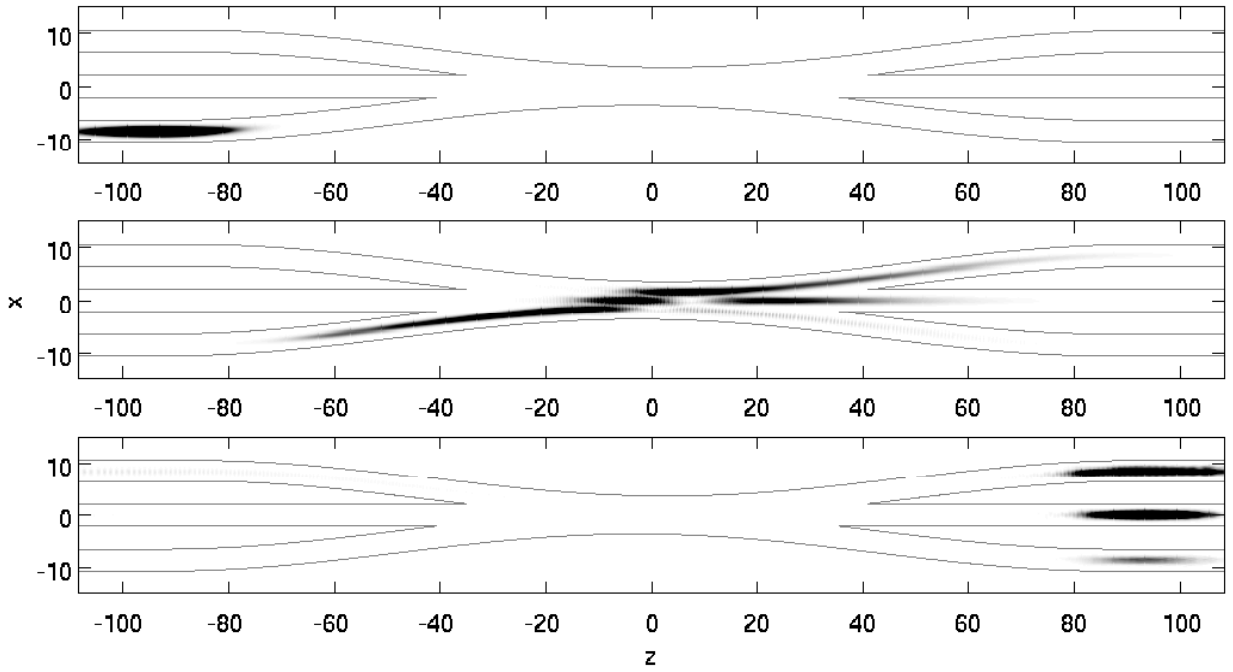

Figure 3. Time evolution of the wavepacket in an intuitive arrangement of the waveguides for the same parameters as in figure 2.

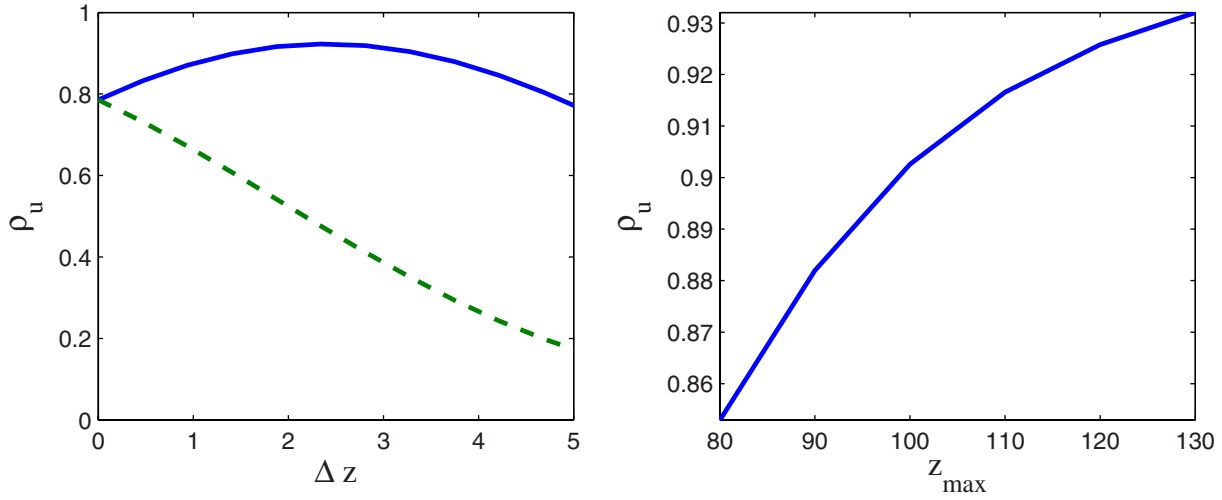

Figure 4. (Left) Probability transferred into the upper waveguide as a function of offset between the two outer guides. The full line shows the results from the intuitive case and the broken line for the counter-intuitive one. (Right) Maximum probability transferred as a function of the length of the interaction region.

4. Atom chips

While the above results clearly demonstrate the viability of the process, it is currently not clear in which experimental system it will be possible to observe it. One of the problems is that the asymptotic eigenstates of the system have to be in resonance at any point in time. This is hard to achieve in many realistic systems as neighbouring trapping potentials usually strongly influence each other when they are close enough to allow for significant tunnelling rates.

Atom chips are well-developed experimental tools these days and consist of an arrangement of current carrying wires mounted on a surface [24]. A current, I_w, flowing through a wire creates a magnetic field around it with the minimum sitting on the wire. When applying a homogeneous bias field, B_b, in the direction orthogonal to the wire, a 2D field minimum above the wire can be created at a height given by [24]

$$r_0 = \left(\frac{\mu_0}{2\pi}\right)\frac{I_w}{B_b}. \tag{5}$$

To lift the energetic degeneracy between trapped and untrapped spin states and thereby avoid spin flip losses at the field minimum, it is necessary to apply a second small B-field component, B_{ip}, along the axis of the wire (z-axis). This changes the potential at the minimum from linear to harmonic [24]:

$$U(r,z) \approx U_z + \tfrac{1}{2}m\omega_r^2(r-r_0)^2, \tag{6}$$

where $U_z = m_F g_F \mu_B |B_{ip}|$ and the radial harmonic trap frequency is

$$\omega_r = \frac{\mu_0}{2\pi}\frac{I_w}{r_0^2}\sqrt{\frac{m_F g_F \mu_B}{m B_{ip}}}. \tag{7}$$

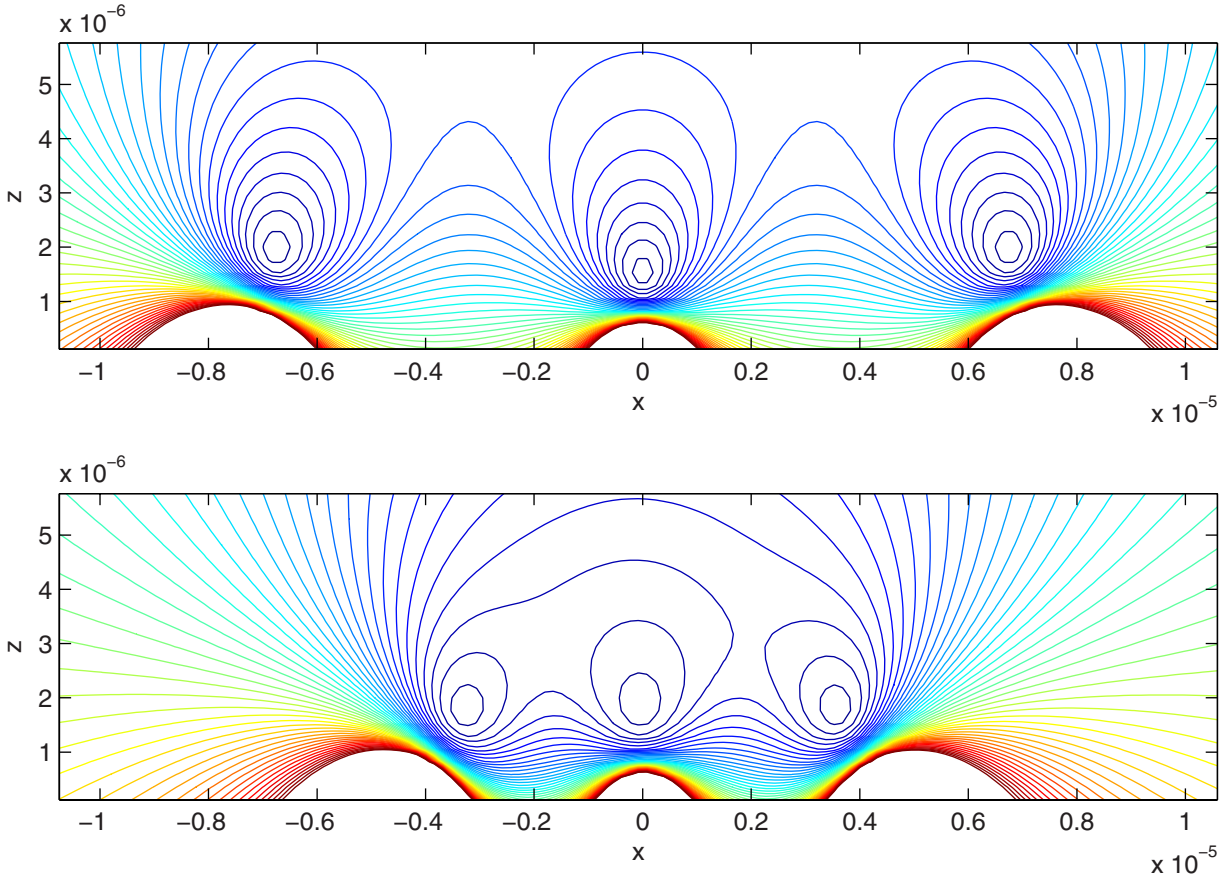

Figure 5. Potentials above the three wires on an atom chip when all wires are separated at an equal distance (upper) and at the point where the wire on the left is closest to the centre wire (lower).

We simulate the STIRAP process by considering three such wires separated by a distance of 9 μm initially. The overall length of the coupling zone is chosen such that in the intuitive case several Rabi oscillations can be expected and the distance between two wires at the point of closest approach is chosen as 4.5 μm. The applied bias field has a magnitude of $B_b = 100$ G and, because of the small curvature of the wires, can be regarded as orthogonal at any point. Since a large ground state is advantageous for tunnelling, the atomic species we consider is ^{6}Li.

In general, the central minimum is influenced by the fields from the two outer wires and increasingly so as the wires come closer. This will affect the resonance condition and ultimately prevent the STIRAP process from working. In order to minimize this behaviour, we make use of a trick and adjust the current going through the middle wire to be slightly lower than the ones going through the outer wires. In our simulations, we choose $I_m = 700$ mA for the middle wire and $I_{l,r} = 1000$ mA for the two outer wires.

Figure 5 shows the potential above the wires for the two different situations of symmetric distance between all wires (upper graph) and when the left wire is closer to the centre one than the right wire (lower graph). While an asymmetry in the second case is clearly visible, its effect on the potentials is moderate.

A full 3D simulation of the STIRAP process in these potentials is a numerically taxing task and beyond our current capabilities. We have therefore simulated the process by using the 2D potentials of the kind displayed in figure 5 and changing the distance between the wires as a function of time. In doing so, we neglect the dispersion of the wavefunction along the longitudinal direction. However, since we have shown in section 3 that the dispersion does not have any significant effect on the transfer fidelity, our simulations can be seen as a good approximation of the full situation.

In figure 6, we show the results of these simulations by displaying the populations in the individual traps as a function of time for the intuitive (right) and the counter-intuitive case (left). Initially, all population is on the left-hand side and it can be clearly seen that in the counter-intuitive situation there is a smooth transition over to the right-hand side. While in the perfect STIRAP setup no population should ever appear in the central trap, the various imperfections of this realistic example lead to a finite occupation during the process. However, at the very end no population is left in the middle trap. Contrary to this, the graph for the intuitive case shows Rabi oscillations between neighbouring waveguides and a less than full transfer of the wavefunction. These are two signs that would allow us to distinguish adiabatic transfer from simple tunnelling.

The fact that we achieve higher transfer fidelities in this non-perfect situation compared to the results presented in section 3 is purely due to being able to evolve more adiabatically in time than in space due to the limitations of our computer hardware.

5. Conclusion

We have investigated the use of the STIRAP technique to transfer atomic wavepackets between neighbouring

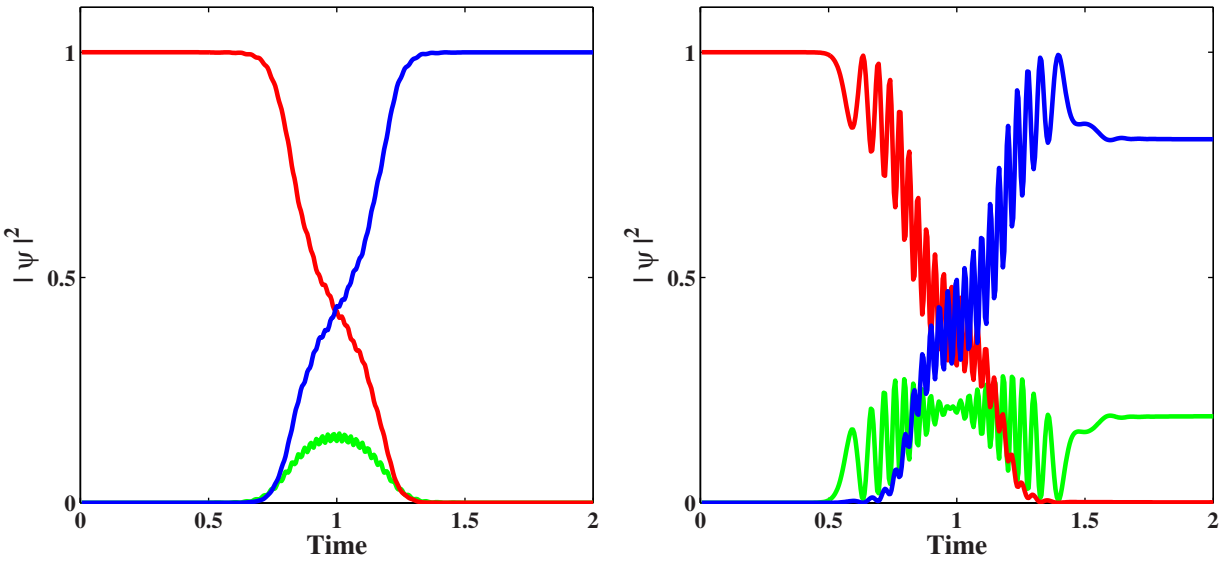

Figure 6. Population in the individual waveguides as a function of time for the counter-intuitive (left) and intuitive (right) waveguide arrangements. The population in the trap on the left is shown by the blue line, the middle one by the green line and the one on the right by the red line.

waveguides. Using an idealized system, we have first shown that the dispersion along the guide does not significantly affect the transfer probability. This was done by introducing a harmonic potential along the longitudinal axis, which allowed us to refocus the wavepacket after half an oscillation period. We have then simulated the STIRAP process using realistic potentials created above current-carrying wires on atom chips and have shown that by choosing a lower current for the central wire the energetic resonance condition can be fulfilled at any point to a very high degree. The results clearly showed that adiabatic transfer in the counter-intuitive setup leads to higher fidelity and can be clearly distinguished from direct tunnelling in the intuitive setup by the absence of Rabi oscillations.

Acknowledgments

This project was supported by Science Foundation Ireland under project number 05/IN/I852. BOS acknowledges support from IRCSET through the Embark Initiative RS/2006/172. The work is dedicated to Prof. Stig Stenholm on his 70th birthday.

References

[1] Hänsel W, Reichel J, Hommelhoff P and Hänsch T W 2001 *Phys. Rev.* A **64** 063607
[2] Bergamini S, Darquié B, Jones M, Jacubowiez L, Browaeys A and Grangier P 2004 *J. Opt. Soc. Am.* B **21** 1889
[3] Chuu C S, Schreck F, Meyrath T P, Hanssen J L, Price G N and Raizen M G 2005 *Phys. Rev. Lett.* **95** 260403
[4] Shevchenko A, Heiliö M, Lindvall T, Jaakkola A, Tittonen I, Kaivola M and Pfau T 2006 *Phys. Rev.* A **73** 051401
[5] Eschner J, Raab C, Schmidt-Kaler F and Blatt R 2001 *Nature* **413** 495
[6] Beugnon J, Jones M P A, Dingjan J, Darquié B, Messin G, Browaeys A and Grangier P 2006 *Nature* **440** 779
[7] Brennen G K, Caves C M, Jessen P S and Deutsch I H 1999 *Phys. Rev. Lett.* **82** 1060
[8] Jaksch D, Briegel H-J, Cirac J I, Gardiner C W and Zoller P 1999 *Phys. Rev. Lett.* **82** 1975
[9] Jaksch D, Cirac J I, Zoller P, Rolston S L, Côté R and Lukin M D 2000 *Phys. Rev. Lett.* **85** 2208
[10] Birkl G, Buchkremer F B J, Dumke R and Ertmer W 2001 *Opt. Comm.* **191** 67
[11] Khudaverdyan M, Alt W, Dotsenko I, Förster L, Kuhr S, Meschede D, Miroshnychenko Y, Schrader D and Rauschenbeutel A 2005 *Phys. Rev.* A **71** 031404
[12] Yavuz D D, Kulatunga P B, Urban E, Johnson T A, Proite N, Henage T, Walker T G and Saffman M 2006 *Phys. Rev. Lett.* **96** 063001
[13] Sortais Y R P *et al* 2007 *Phys. Rev.* A **75** 013406
[14] Fortier K M, Kim S Y, Gibbons M J, Ahmadi P and Chapman M S 2007 *Phys. Rev. Lett.* **98** 233601
[15] Zhang M, Zhang P, Chapman M S and You L 2006 *Phys. Rev. Lett.* **97** 070403
[16] Eckert K, Lewenstein M, Corbalán R, Birkl G, Ertmer W and Mompart J 2004 *J Phys. Rev.* A **70** 023606
[17] Eckert K, Mompart J, Corbalán R, Lewenstein M and Birkl G 2006 *Opt. Commun.* **264** 264
[18] Karski M, Förster L, Choi J-M, Steffen A, Alt W, Meschede D and Widera A 2009 *Science* **325** 174
[19] Mompart J, Eckert K, Ertmer W, Birkl G and Lewenstein M 2003 *Phys. Rev. Lett.* **90** 147901
[20] Greentree A S, Cole J H, Hamilton A R and Hollenberg L C L 2004 *Phys. Rev.* B **70** 235317
[21] Bergmann K, Theuer H and Shore B W 1998 *Rev. Mod. Phys.* **70** 1003
[22] Vitanov N V, Fleischhauer M, Shore B W and Bergmann K 2001 *Adv. At., Mol. Opt. Phys.* **46** 55
[23] Härkönen K, Kärki O and Suominen K-A 2006 *Phys. Rev.* A **74** 043404
[24] Folman R, Krüger P, Schmiedmayer J, Denschlag J and Henkel C 2002 *Adv. At. Mol. Opt. Phys.* **48** 263–356
[25] Longhi S, Della Valle G, Ornigotti M and Laporta P 2007 *Phys. Rev.* B **76** 201101
[26] Jääskeläinen M and Stenholm S 2003 *Phys. Rev.* A **68** 033607

3.2 Coherent Transport by Adiabatic Passage on Atom Chips

Manuscript Information

Manuscript Title: Coherent transport by adiabatic passage on atom chips.

Journal Information: Physical Review A **88**, 053618 (2013).

Authors: Tadhg Morgan, Lee James O'Riordan, Neil Crowley, Brian O'Sullivan and Thomas Busch.

Pages: 6.

Figures: 6.

PHYSICAL REVIEW A **88**, 053618 (2013)

Coherent transport by adiabatic passage on atom chips

T. Morgan,[1,2] L. J. O'Riordan,[1,2] N. Crowley,[1] B. O'Sullivan,[1] and Th. Busch[1,2]
[1]*Department of Physics, University College Cork, Cork, Ireland*
[2]*Quantum Systems Unit, OIST Graduate University, Okinawa, Japan*
(Received 12 September 2013; published 15 November 2013)

Adiabatic techniques offer some of the most promising tools for achieving high-fidelity control of the center-of-mass degree of freedom of single atoms. Because the main requirement of these techniques is to follow an eigenstate of the system, constraints on timing and field strength stability are usually low, especially for trapped systems. In this paper we present a detailed example of a technique to adiabatically transport a single atom between different waveguides on an atom chip. To ensure that all conditions are fulfilled, we carry out fully three-dimensional simulations of the system, using experimentally realistic parameters. We also detail our method for simulating the system in very reasonable time scales on a consumer desktop machine by leveraging the power of graphics-processing-unit computing.

DOI: 10.1103/PhysRevA.88.053618 PACS number(s): 03.75.−b, 05.60.Gg, 67.85.−d

I. INTRODUCTION

Recent experimental progress in trapping and controlling all degrees of freedom of single atoms and ions has allowed us to test and explore the fundamentals of quantum mechanics at a completely new level [1,2]. In fact, progress has been so dramatic that application of the laws of single- and few-particle quantum mechanics to areas such as quantum information and quantum metrology has come into experimental reach [3,4].

While control over the internal degrees of freedom of atoms is a highly advanced field, significant progress in developing techniques to coherently control the external degrees of freedom to the same level has only recently been achieved. One class of techniques that can offer high fidelities are adiabatic processes, and recently a technique called coherent tunneling by adiabatic passage (CTAP) was shown to be a very promising tool for controlling the quantized center-of-mass state of a single particle trapped in a microtrap [5]. CTAP is designed to transfer populations between microtraps at high fidelities while being robust to variations in the system parameters. Although the physics of CTAP is well understood, the process has yet to be observed experimentally and several realistic systems have recently been proposed [6–8].

Coherent transport between microtraps can be facilitated via tunneling and the tunneling rates can be controlled by moving the centers of the individual traps relative to each other. While this requires dynamical potentials, a similar system with static potentials can be constructed by considering three parallel running waveguides with spatially varying coupling strength between them and an atom which travels along these guides [6]. Recently, in our previous work, a realistic atom chip system of this kind was considered [9]; however, the simulations were limited to two dimensions.

While the transversal dynamics in a system of waveguides can be well described in a two-dimensional model, effects stemming from bending, longitudinal dispersion, and the lack of stationary states in the z direction cannot be accounted for. To overcome these limitations and understand the total dynamics of a waveguide system, it is necessary to carry out a fully three-dimensional simulation.

We therefore present here, an analysis of a system composed of three waveguides by taking the full dynamics in all three spatial directions into account and using realistic experimental parameters. The latter is important as most treatments of the problem in recent years have assumed idealized trapping potentials that guarantee resonance between the individual traps at any moment in time. By carrying out three-dimensional simulations which account for all possible dynamics, we show that CTAP is indeed a suitable technique for use in waveguides on atom chips.

By today, fully three-dimensional simulations of the Schrödinger equation in the context of atomic transport are still rare [10]. The computational resources needed are very large and have traditionally required the power of large supercomputers. Recently it was shown that the emerging technique of graphics-processing-unit (GPU) computing allows tremendous speedup of many numerical techniques including the fast Fourier transform (FFT) [11], which is the main numerical tool that we require. By making use of this, we have been able to perform the simulations of this extensive atomic system with one consumer desktop PC using the CUDA programming model and numerical libraries, on very reasonable time scales.

The structure of this paper is as follows. In Sec. II we briefly review the CTAP process in waveguide systems and in Sec. III we describe the atom chip potentials we are simulating. In Sec. IV we discuss our implementation of CUDA and MPI (message passing interface) codes and examine the performance benefits in each case. Our results of the three-dimensional simulations and the evidence that CTAP can be observed will be presented and discussed in Sec. V. Finally we conclude in Sec. VI.

II. COHERENT TUNNELING BY ADIABATIC PASSAGE

Let us first briefly review the CTAP process by considering an atom trapped in a linear system of three identical, one-dimensional microtraps [5]. Assuming that the atom is in its center-of-mass ground state in the trap on the left-hand side $|L\rangle$, it can reach the ground states of the other two traps $|M\rangle$ and $|R\rangle$ through coherent tunneling described by the strength J_{LM} for the transition $|L\rangle \rightarrow |M\rangle$ and J_{MR} for $|M\rangle \rightarrow |R\rangle$. In

this basis the Hamiltonian is given by

$$H(t) = \hbar \begin{pmatrix} 0 & -J_{LM}(t) & 0 \\ -J_{LM}(t) & 0 & -J_{MR}(t) \\ 0 & -J_{MR}(t) & 0 \end{pmatrix}, \quad (1)$$

where the energy of the trap ground states was renormalized to zero. The tunneling strengths are assumed to be time dependent, which can be achieved by increasing or decreasing the distances between neighboring traps $d_{LM}(t)$ and $d_{MR}(t)$. The eigenstates of the Hamiltonian (1) are well known [2] and of particular interest for adiabatic transport is the so-called dark state

$$|d\rangle = \cos\theta|L\rangle - \sin\theta|R\rangle, \quad (2)$$

in which the mixing angle θ is given as a function of the tunneling strengths as

$$\tan\theta = J_{LM}/J_{MR}. \quad (3)$$

This state has a nondegenerate zero eigenvalue, and an adiabatic evolution will therefore guarantee that the system, once prepared in $|d\rangle$, will always stay in it. Note that the only contribution of $|M\rangle$ to $|d\rangle$ is through the mixing angle and that the system has zero probability to be found in $|M\rangle$ at any time.

The CTAP process can now be understood by considering an atom initially in the state $|L\rangle$. Increasing and decreasing J_{MR} before J_{LM}, which is counterintuitive to traditional tunneling schemes, continuously decreases the population in state $|L\rangle$ and increases the population in state $|R\rangle$, leading to a 100% transfer at the end of the process.

Adapting this process to a system of waveguides is now straightforward. The temporal dependence of the tunneling strength in Eq. (1) can be replaced by a spatial one through suitable adjustment of the distance between neighboring waveguides as a function of the direction the particle travels in (see Fig. 1 for a schematic view) [6].

There are, however, several conditions that both the microtrap and the waveguide system must fulfill for the CTAP dynamics to occur. First, the process must be adiabatic with respect to the other relevant energy scales in the system. For the waveguide system this means the whole process has to be slower than the inverse of the approximate transverse trapping frequencies of the guides. As typical numbers for such guides are in the kHz regime, this means that the time allowed for the atom to travel along the chip can be much shorter than a typical system's lifetime. The second condition which has to be fulfilled, as previously mentioned, is that all trapping states are in resonance at any point in time, which is difficult to achieve once the potentials of the individual guides start to overlap. However, we will demonstrate in the next section how a waveguide setup on an atom chip is a realistic experimental system in which this resonance condition can be fulfilled to a good approximation.

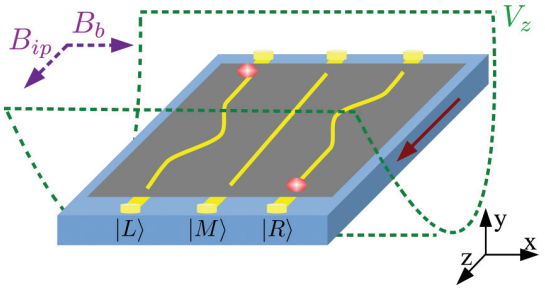

FIG. 1. (Color online) Schematic of the suggested setup for observing the CTAP process in a system of waveguides. Note that the asymmetric approach of the outer wires to the middle wire is exaggerated, so that the counterintuitive arrangement is visible. The atom is initially located in the left guide and, due to the presence of a harmonic oscillator potential V_z in the z direction, travels along the direction indicated by the red solid arrow. We also show the expected position of the atom at $t = \pi/\omega_z$ in the right-hand-side guide and indicate the orientation of the bias field, B_b, and the applied field, B_{ip} (purple dashed arrows).

III. ATOM CHIPS

Atom chips are versatile experimental tools that are by today used extensively in experiments with ultracold atoms [12,13]. A small current flowing through nanofabricated wires on the substrate produces a magnetic field gradient in such a way that cold atoms can be trapped very close to the surface. Because the layout of the nanowires can be chosen during the chip's production process, atom chips have been used in many cold-atom experiments to produce microtraps, interferometers, and waveguides [12,14–16]. Here we will take advantage of this versatility to consider waveguides in the geometry indicated in Fig. 1 and develop a procedure which will allow us to observe high-fidelity transport based on CTAP.

Let us briefly review the basic description and properties of atom chip trapping. The magnetic potential $\mathbf{B}$ at position $\mathbf{r}$ generated by a typical nanowire on an atom chip can be described by the Biot-Savart law

$$\mathbf{B} = \frac{\mu_0 I}{4\pi} \oint \frac{d\mathbf{l} \times \hat{\mathbf{r}}}{r^2}, \quad (4)$$

where I is the current in the wire, μ_0 the vacuum permeability, $\hat{\mathbf{r}}$ the unit vector in the direction of $\mathbf{r}$, and $d\mathbf{l}$ the differential length of the wire carrying current I. For this expression to be valid, however, we have to assume that the thickness of the wire is negligible, which is a good approximation as long as we are using the properties of the field at a sufficient distance above the chip's surface. To achieve this and to lift the field minima above the nanowires for the desired waveguide structure, a homogeneous magnetic bias field B_b can be applied orthogonal to the current flow. This raises the potential minimum to a height above the wire given by

$$r_0 = \frac{\mu_0}{2\pi}\frac{I}{B_b}. \quad (5)$$

Finally, to lift the degeneracy of the spin states of the atoms and avoid losses due to spin flips at the center of the waveguide a further magnetic field B_{ip} parallel to the direction of the wires is usually applied.

An example of the waveguide potentials resulting from this model for ^{6}Li atoms and for experimentally realistic parameters is shown in Fig. 2. If an atom is initially located in the left waveguide and travels in the positive z direction, these waveguides provide the desired counterintuitive tunnel coupling needed for CTAP. To give the atom momentum to

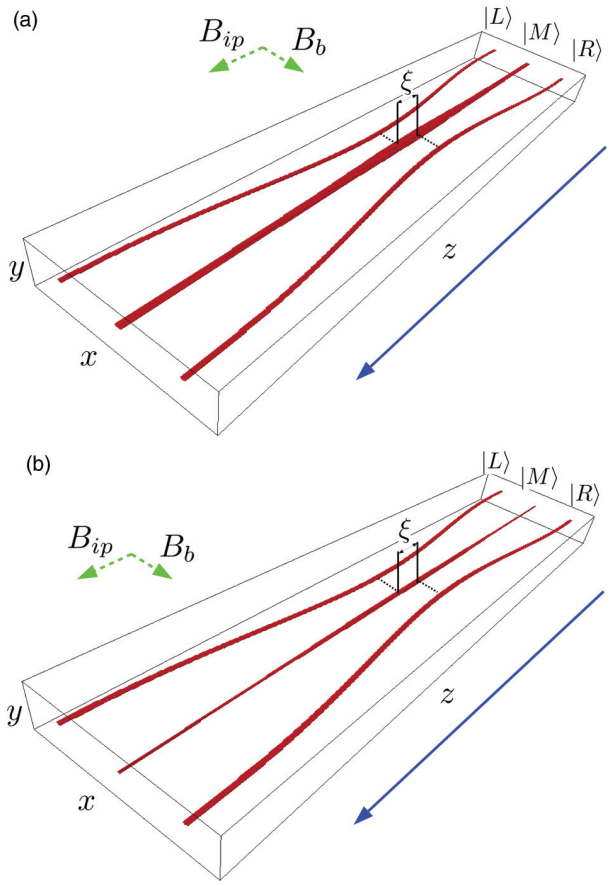

FIG. 2. (Color online) Isosurfaces of the waveguides created on an atom chip with the direction of propagation indicated by the blue solid arrow (for clarity $V_z = 0$ in this plot). The dimensions of the interesting area on the chip we simulate are 20 μm $\times$1000 μm ($x \times z$) and we take a height (y direction) above the chip of 4 μm into account. The three wires are initially equally separated by 7 μm and their distance at the position of closest approach is 4.3 μm. The left wire remains straight initially for a distance of 50 μm, which produces an asymmetry in the point of closest approach of the left and right wires to the middle wire as indicated by ξ. The bias and applied fields (indicated by the green dashed arrows) are $B_b = 140 \times 10^{-4}$ T and $B_{ip} = 300 \times 10^{-4}$ T. In (a) the currents of the left, middle, and right wires are $I_L = I_M = I_R = 0.1$ A, respectively, and in (b) the currents of the left and right wires are $I_L = I_R = 0.1$ A and the middle wire current is reduced to $I_M = 0.07$ A.

travel along the wires we add an additional harmonic oscillator potential V_z of frequency ω_z along the z direction, which is centered at the middle of the chip (see Fig. 1). This will also lead to a refocusing of the traveling wave packet at the classical turning point on the other side of the chip and help to clearly determine the position of the atom.

To ensure that the process is adiabatic and the atom remains in the dark state of the system at all times, the total time for the process has to be much larger than the inverse of the transverse trapping frequencies of the individual waveguides. By approximating the potentials to have a harmonic oscillator shape in the transverse direction, we find the inverse of the relevant frequency to be of the order of $f_{\mathrm{HO}}^{-1} \approx 0.2$ ms, and by choosing the trapping frequency of the harmonic oscillator in the z direction to be $\omega_z = 2\pi \times 5$ Hz, the total time taken for the process (half an oscillation) is 0.1 s. This allows the adiabaticity condition to be clearly fulfilled at any point during the evolution.

Finally, the bend in the wires will lead to a potential from the currents in the z direction, which requires the atom to have enough kinetic energy to overcome it and therefore sets an upper bound to the adiabaticity that can be reached. However, this effect can be reduced by increasing the length of the atom chip (z direction) and therefore reducing the curvature of the wires. From our simulations, we find that the kinetic energy resulting from locating an atom initially at the edge of a chip that is $z_{\max} = 1000$ μm long allows us to successfully propagate the atom though the waveguides using the harmonic trap described above.

IV. MPI AND CUDA

To simulate the propagation of the atom along the waveguide we solve the three-dimensional time-dependent Schrödinger equation using the well known Fourier split-operator method [17]. A typical numerical implementation of this method requires the use of four Fourier transforms followed by three complex multiplications for each time step. The numerical library we make use of to perform the Fourier transforms is the well known FFTW library, and its GPU implementation CUFFT [18].

Performing three-dimensional Fourier transforms is the most intensive part of our code with the length of time required to perform one iteration of the split operator method depending heavily upon the size of the numerical grid. As discussed in the previous section, the atom chip has a relatively large extension in the z direction ($z_{\max} = 1000$ μm) compared to the other dimensions. Since the maximum value of the momentum grid is defined as $p_{\max} = \frac{\pi N_z}{z_{\max}}$ we require a large number of points, N_z, for our grid to be large enough to resolve the longitudinal momentum stemming from the external harmonic oscillator potential. This is the main reason that the computational resources required to simulate the system are quite substantial.

A. GPU computing

To overcome the numerical barrier presented by this system we turn to the relatively new computing paradigm of GPU computing. Whereas traditional computers perform computations using the central processing unit (CPU), GPU computing allows some of the work to be off loaded to the graphics processor. GPUs are inherently single-instruction, multiple-data (SIMD) devices, designed for operating upon a large data set at a given time with a single task, such as a two-dimensional grid of pixels. Due to their parallel nature, GPUs can perform better than CPUs for certain types of calculations. One example where they offer large performance gains are fast Fourier transformations and it was recently shown that the Fourier split-operator method can be accelerated using GPU computation [11]. This performance increase offers the numerical power needed to simulate the above system and we have implemented the algorithms for split-operator evolution of the Schrödinger equation with C, CUDA, and Nvidia's CUFFT libraries for the Fourier transforms.

TABLE I. Approximate times taken to simulate the propagation of an atom through our atom chip system on both GPU and CPU.

Device	No. devices	Timing	Rel. improvement
CPU (MPI)	8	~6 Hr	1.0×
	16	~4 Hr	1.5×
	32	~1.5 Hr	4.0×
	64	~1 Hr	6.0×
GPU	1	~1 Hr	6.0×

B. Performance

To demonstrate the performance offered by GPU computing we compare it to using FFTW with MPI, a more traditional CPU-based method. The MPI implementation allows the code to be run across multiple machines, benefiting from the parallelism which may be offered by a supercomputing cluster. Although MPI-enabled FFTW is fast and supports extremely large grid sizes, it requires computer-cluster access of a significant size to be a viable option.

To effectively simulate the CTAP process and accurately resolve the momentum, our code requires a grid size of $256 \times 64 \times 1024$ ($x \times y \times z$). For accurate time evolution, a time step of $\Delta t = 1 \times 10^{-6}$ s was found to be adequate. For the GPU simulations, the test system was an Intel Core i7 2600K CPU at stock frequency, 8 GB double data rate type three (DDR3) memory operating at 1600 MHz, 7200 rpm hard disk drive (HDD), Nvidia GeForce GTX 580 with 3 GB of onboard memory running at 783 MHz GPU core frequency, 1566 MHz shader processor frequency, and 2010 MHz memory frequency. For all simulations the desktop was running the Ubuntu 11.10 64-bit operating system and all calculations were performed in double precision (64-bit floating point) where applicable. For the CPU simulations we utilized the supercomputers at the Irish Centre of High-End Computing (ICHEC).

Table I shows the approximate timings for the completion of runs on GPU and CPU. As one can see, not only does GPU computing offer a sixfold improvement over a single CPU, it also allows us to achieve a performance level which is comparable to a 64 core CPU. Such performance has previously been restricted to high powered supercomputers. Having such computational power available to a single user on a desktop computer allows us to obtain a large volume of simulated data on a much shorter time scale rather than through the use of a shared resource CPU-based computer cluster. Additionally, a second GPU card added to the system allowed concurrent runs of the code, which effectively halved the overall time required for a large number of simulations. It is also worth mentioning that moving computations over to the GPU of the system frees up the CPU and a large part of the system memory to be used for other tasks that would have previously been inhibited by CPU bound computations.

V. 3D SIMULATIONS

In the following section we present a set of typical results from the GPU-accelerated three-dimensional (3D) simulations we carried out over a large range of experimentally controllable parameters and show that the atom chip allows the CTAP process to take place. All parameters for our atom chip are the same as in Fig. 2 unless otherwise stated.

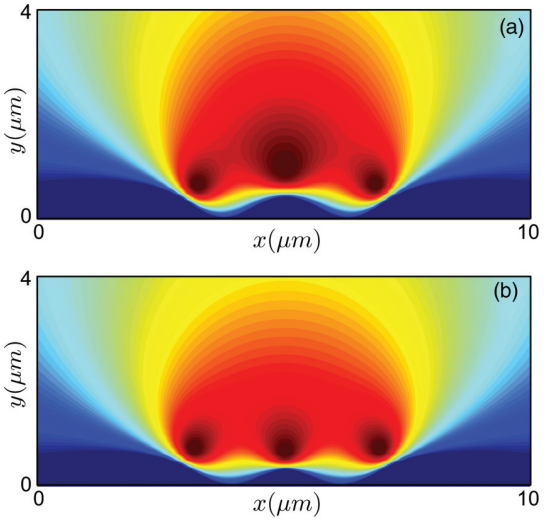

FIG. 3. (Color online) Contour plot of the waveguides at 500 μm along the -axis. Panel (a) shows the deformation of the waveguides when all currents are equal, $I_L = I_M = I_R = 0.1$ A, and panel (b) shows how this effect can be mitigated by using a reduced middle-wire current of $I_M = 0.07$ A, while the current in the outer wires remain at $I_L = I_R = 0.1$ A.

Our simulations start out with a single ^{6}Li atom which is initially located in the left waveguide. Its transversal wave function corresponds to the ground state of the potential in the transversal direction (determined numerically) and longitudinally we assume a Gaussian profile of similar width. We then evolve this initial state in time, and due to the longitudinal harmonic oscillator potential centered at the middle of the atom chip ($z = 500$ μm), the atom starts to propagate along the waveguide.

Initially the wires are far enough away from each other for each waveguide to be approximately given by the current of the wire closest to it and if all currents are identical, the waveguides are in resonance. However, once the wires start approaching each other, the respective magnetic fields add and create waveguide potentials of unequal size [see Figs. 2(a) and 3(a)]. This drives the transversal ground states of the guides out of resonance and the conditions for observing the CTAP process are no longer given.

However, atom chips offer an intriguingly straightforward way to adjust for this, as the current in each wire can be individually (and even time-dependently) controlled. This can be used to compensate for effects stemming from the potentials overlapping and ensure resonance between the waveguides [9]. While one can imagine a numerically optimized algorithm that adjusts the currents in a time-dependent manner based on the position of the center-of-mass of the atom, here we will show that a much simpler approach, which maintains the simplicity of all currents being constant in time, is already sufficient. We suggest reducing the current in the middle wire so that in the crucial coupling region, where the magnetic fields from neighboring waveguides have the strongest

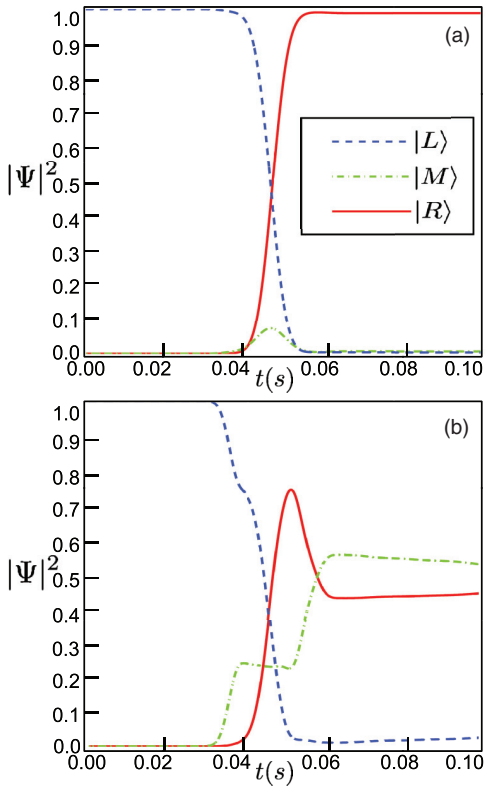

FIG. 4. (Color online) The population in the left (blue dashed line), middle (green dot-dash line) and right (red solid line) waveguides as a function of time for (a) the counter-intuitive waveguide arrangement and (b) the intuitive, direct tunneling one. The current in the middle wire is reduced to $I_M = 0.07A$.

influence on each other, the waveguides are approximately resonant.

To demonstrate the effect of this adjustment we show in Fig. 3 a transversal cut through the system at the middle of the chip ($z = 500$ μm) for the case where (a) all three currents are identical ($I = 0.1$ A) and (b) the current in the middle wire is reduced ($I_M = 0.07$ A). One can clearly see that the transversal shape of the waveguides is very similar for the case of the reduced center current, which indicates that this approach can lead to enhanced resonance between the guides.

In the areas where the guides are farther away from each other, however, the reduced current in the middle wire will have the opposite effect and reduce the quality of the resonance. This can clearly be seen from the iso-potential surface plot in Fig. 2(b). Yet, since the tunneling in these areas is small, it has only a negligible influence on the CTAP process and we will in the following demonstrate that the near resonant setup of Fig. 3(b) allows us to observe the CTAP process.

In Fig. 4 we show the population in each waveguide as a function of time for an atom chip with reduced current in the central wire. The results in Fig. 4(a) are obtained for the situations where the wires are arranged such that the counterintuitive tunneling sequence takes place and full transfer from the initial guide into the final guide is clearly visible. Only a small population in the central guide appears halfway through the process, and while the ideal CTAP process

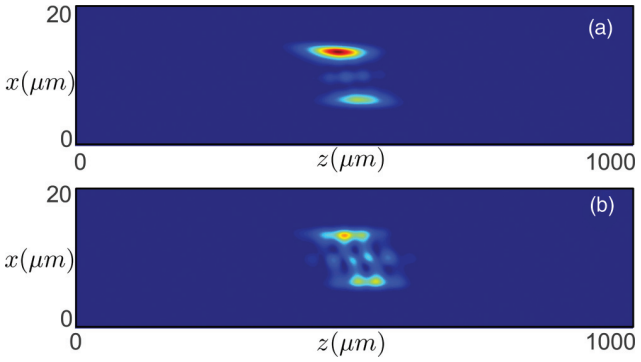

FIG. 5. (Color online) The density of the atomic state at $t = 0.048$ for (a) the counterintuitive setup and (b) the intuitive one. The current in the middle wire is $I_M = 0.07$ A in both cases.

does not allow for population in the central trap at any time, the limited adiabaticity and resonance of the simulated setup leads to this temporary deviation. However, it has no effect on the final state.

In contrast to this, and confirming that the large fidelity of the transport process above is due to CTAP, we show in Fig. 4(b) the results for an intuitive arrangement of the waveguides on the atom chip. As is clearly visible, this does not produce high-fidelity population transfer to the guide on the right-hand side, but rather leads to a split of the probability between the middle and the right-hand-side wire.

While Fig. 4 only gives an indication of the ongoing process as a function of time, the presence of the CTAP process for the counterintuitively arranged wires can also be inferred from looking at the atomic probability distribution in real space. For this we show in Fig. 5 the density of the atomic state in the x and z planes at $t = 0.048$ s integrated over the y direction. At this time the atomic wave packet is in the region where the tunneling interaction between all three waveguides is large and clear differences between the two situations are visible. Figure 5(a) shows the counterintuitive situation where the wave packet can be seen to follow the dark state with only a negligible population component in the middle waveguide. In contrast, Fig. 5(b) shows the intuitive setup, in which the population is distributed between all three waveguides and clear signatures of Rabi oscillations due to the direct tunneling are clearly visible.

It is exactly these Rabi oscillations in the intuitive process that lead to the time dependence of the final population in each waveguide and therefore a strong dependence of the outcome on small changes in the system parameters. This can be seen when examining Fig. 6, where we show the final population in the right-hand-side waveguide as a function of the current in the middle wire I_M. For the intuitive process (blue dashed line), the final population varies significantly with changing I_M, whereas the counterintuitive setup (red solid line) is very robust to these changes, with the fidelity of population transfer never dropping below 0.98. This is another indication that the transfer is due to CTAP.

From Fig. 6 it is also clear that, while there are large oscillations in the fidelity of the intuitive process, there is an upward trend in the fidelity of the process towards unity as the current in the middle wire increases. However, at these

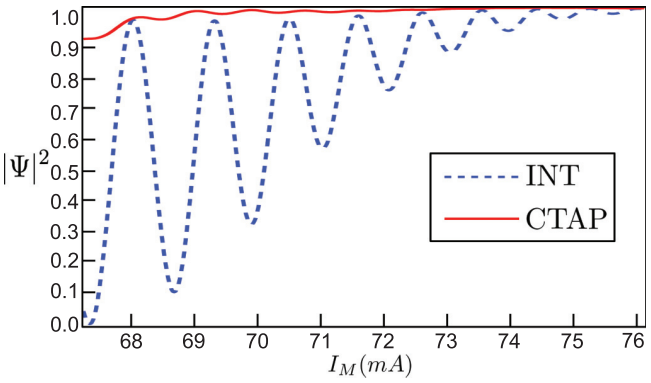

FIG. 6. (Color online) The final population in the target waveguide for both the CTAP (red solid line) and intuitive (blue dashed line) processes, for values of $I_M = 0.0672$ A to $I_M = 0.0761$ A in steps of 0.001 A.

higher values of the middle-wire current, the waveguides are no longer resonant at all times and one would expect that neither the CTAP nor the intuitive processes would lead to high-fidelity transfer. Nevertheless, the simulations show that this is not the case.

We conjecture that in the regime of larger currents in the middle wire the population transfer is due to Stark-shift-chirped rapid-adiabatic passage (SCRAP) [19]. In this process a time-dependent shift of the energy of the intermediate state in the traditional three-level arrangement allows high-fidelity population transfer between two states, independent of being in the intuitive or counterintuitive situation. A translation of this to the spatial realm is straightforward: the approach and retreat of the outer wires from the middle one shift the energy of the central waveguide in a spatially dependent manner. This effect is the topic of a future investigation.

VI. CONCLUSIONS

We have performed fully three-dimensional simulations of an experimentally realistic waveguide system on an atom chip, where the arrangements of the wires produce spatial-dependent tunnel couplings between the waveguides. These simulations were done by implementing the CUFFT library provided by Nvidia, which made this problem numerically tractable on a desktop computer.

Using a simple method for controlling the resonance as the waveguides are brought close together, we have demonstrated that a counterintuitive approach of the outer wires to the middle allows us to observe high fidelity and robust transfer between the wires due to CTAP. In contrast, for intuitively coupled waveguides, where direct tunneling between them is allowed to occur, significant Rabi oscillations between all guides exist. This makes the transfer process highly sensitive to the system parameters. While a large number of theoretical works on CTAP exist, the analysis presented offers a direct way for experimental observation and confirmation of the effect.

Finally, we have also seen an indication that waveguide systems might be natural systems for observing the SCRAP protocol and a detailed investigation will be the topic of a future work. While we have used the numerical methods described here to perform three-dimensional simulations, they can actually be used in any number of dimensions, where they still offer large performance gains over standard CPU approaches.

ACKNOWLEDGMENTS

The authors thank Peter Krüger and Thomas Fernholz for valuable discussions and ICHEC for use of their computing resources for the MPI-enabled code. This work was supported by Science Foundation Ireland under Project No. 10/IN.1/I2979.

[1] Y. A. Chen, S. Nascimbène, M. Aidelsburger, M. Atala, S. Trotzky, and I. Bloch, Phys. Rev. Lett. **107**, 210405 (2011).
[2] K. Bergmann, H. Theuer, and B. W. Shore, Rev. Mod. Phys. **70**, 1003 (1998).
[3] M. A. Nielsen and I. L. Chuang, *Quantum Computation and Quantum Information* (Cambridge University, Cambridge, England, 2000).
[4] M. Riedel, P. Bohi, Y. Li, T. Hansch, A. Sinatra, and P. Treutlein, Nature **464**, 1170 (2010).
[5] K. Eckert, M. Lewenstein, R. Corbalán, G. Birkl, W. Ertmer, and J. Mompart, Phys. Rev. A **70**, 023606 (2004).
[6] K. Eckert, J. Mompart, R. Corbalán, M. Lewenstein, and G. Birkl, Opt. Commun. **264**, 264 (2006).
[7] T. Morgan, B. O'Sullivan, and Th. Busch, Phys. Rev. A **83**, 053620 (2011).
[8] J. Huneke, G. Platero, and S. Kohler, Phys. Rev. Lett. **110**, 036802 (2013).
[9] B. O'Sullivan, P. Morrissey, T. Morgan, and Th. Busch, Phys. Scr. T **140**, 014029 (2010).
[10] M. Rab, J. H. Cole, N. G. Parker, A. D. Greentree, L. C. L. Hollenberg, and A. M. Martin, Phys. Rev. A **77**, 061602 (2008).
[11] H. Bauke and C. H. Keitel, Comp. Phys. Comm. **182**, 2454 (2011).
[12] J. Fortagh and C. Zimmermann, Rev. Mod. Phys. **79**, 235 (2007).
[13] R. Folman, P. Krüger, D. Cassettari, B. Hessmo, T. Maier, and J. Schmiedmayer, Phys. Rev. Lett. **84**, 4749 (2000).
[14] P. D. D. Schwindt, E. A. Cornell, T. Kishimoto, Y. J. Wang, and D. Z. Anderson, Phys. Rev. A **72**, 023612 (2005).
[15] J. Petrovic, I. Herrera, P. Lombardi, and F. Cataliotti, New J. Phys. **15**, 043002 (2013).
[16] T. Schumm, S. Hofferberth, L. M. Andersson, S. Wildermuth, S. Groth, I. Bar-Joseph, J. Schmiedmayer, and P. Krüger, Nat. Phys. **1**, 57 (2005).
[17] J. A. Fleck, J. R. Morris, and M. D. Feit, Appl. Phys. **10**, 129 (1976).
[18] Nvidia, Inc. http://developer.nvidia.com/nvidia-gpu-computing-documentation (accessed 16/02/2012).
[19] A. A. Rangelov, N. V. Vitanov, L. P. Yatsenko, B. W. Shore, T. Halfmann, and K. Bergmann, Phys. Rev. A **72**, 053403 (2005).

Chapter 4

Coherent Adiabatic Transport of Atoms in Radio Frequency Traps

In the manuscript presented in this Chapter, we investigate adiabatic radio frequency (rf) potentials as another realistic system in which Coherent Tunnelling by Adiabatic Passage (CTAP) can be observed [1].

Adiabatic rf potentials are typically made in conjunction with atom chips [89], but have also been created in quadrupole traps [98] and were first used to created dressed states of cold neutron [97]. More recently, adiabatic rf potentials have evolved into one of the most versatile tools for trapping cold atoms[27, 28, 89]. The advantage of rf-systems over other types of trapping potentials is that their physics is well known, they are relatively benign systems to work with experimentally and are widely available today.

Experimental progress in more recent years has seen a shift from using rf radiation to create standard trapping potentials [27], towards creating more complicated, non-standard trapping geometries such as ring traps [99], toroidal traps [100], linear multi-well potentials [29] and traps that can transition between ring shaped and double well geometries [26]. As a result of this progress towards greater versatility, they have also been used to control and manipulate matter waves in a time-dependent way [26, 28, 89]. There have also been a number of interesting theoretical works in recent years such as a study of non rotating wave approximation effects in adiabatic rf potentials [59], geometric phase of atoms in adiabatic rf potentials [101] and a method for enhancing on-site interactions of tunnelling atoms in optical potentials [102]

In this Chapter we will theoretically show that an rf system of six separate frequencies can produce a triple well potential in which CTAP can be performed. Adiabatic rf

[1] The work in this manuscript was done in collaboration with Brian O'Sullivan. Each author contributed to all areas of the manuscript.

potentials can fulfil the requirements for CTAP to a very high degree in an experimentally realistic setup and therefore produce the kind of robust, high fidelity transport the scheme allows for. We will also show that the rf system allows the extension of the CTAP process to coherently control a cloud of interacting atoms. This is beyond what could be achieved with magnetic waveguides on atom chips in Chapters 3 and 4, where we were limited to transporting single atoms.

4.1 Coherent Adiabatic Transport of Atoms in Radio-Frequency Traps

Manuscript Information

Manuscript Title: Coherent adiabatic transport of atoms in radio-frequency traps.

Journal Information: Physical Review A **83**, 053620 (2011). (Erratum) Physical Review A **85**, 039904(E) (2012).

Authors: Tadhg Morgan, Brian O'Sullivan and Thomas Busch.

Pages: 7.

Figures: 7.

PHYSICAL REVIEW A **83**, 053620 (2011)

Coherent adiabatic transport of atoms in radio-frequency traps

T. Morgan, B. O'Sullivan, and Th. Busch
Department of Physics, University College Cork, Cork, Ireland
(Received 21 March 2011; published 19 May 2011)

Coherent transport by adiabatic passage has recently been suggested as a high-fidelity technique to engineer the center-of-mass state of single atoms in inhomogeneous environments. While the basic theory behind this process is well understood, several conceptual challenges for its experimental observation have still to be addressed. One of these is the difficulty that currently available optical or magnetic micro-trap systems have in adjusting the tunneling rate time dependently while keeping resonance between the asymptotic trapping states at all times. Here we suggest that both requirements can be fulfilled to a very high degree in an experimentally realistic setup based on radio-frequency traps on atom chips. We show that operations with close to 100% fidelity can be achieved and that these systems also allow significant improvements for performing adiabatic passage with interacting atomic clouds.

DOI: 10.1103/PhysRevA.83.053620 PACS number(s): 03.75.−b, 05.60.Gg, 67.85.−d

I. INTRODUCTION

Going beyond nanotechnologies and engineering quantum systems on the basis of single particles has in recent years been one of the most exciting and active areas of physics [1]. Due to the fragile nature of single-particle quantum states, quantum engineering techniques need to be fault tolerant and lead to high fidelities on every application to avoid the large and costly overhead that comes with error-correction schemes [2]. Comprising one class of techniques that can achieve this are so-called adiabatic techniques and their use in optical systems has been widely investigated in the past. In particular, stimulated Raman adiabatic passage (STIRAP) is one adiabatic technique that allows the transfer of the populations from one electronic state to another with 100% fidelity [3]. It relies on the existence of a so-called dark state in a three-level system and requires a counterintuitive pulse sequence to coherently couple the individual levels.

Recently, it has been shown that similar techniques can, in principle, be used to control the quantized center-of-mass state of single particles [4–6]. This atom-optical analog has been dubbed coherent transport by adiabatic passage (CTAP) and while the possibility of observing this process has received significant attention [7,8], the conditions that have to be fulfilled for its observation are currently hard to achieve experimentally. In particular, all states involved are required to be in resonance during the whole process. However, since the strength of the tunnel coupling is usually adjusted by changing the distance between the microtraps, which leads to significant overlap of the neighboring trapping potentials, the eigenstates become time dependent. Several solutions to the problem have been suggested, all involving significant experimental resources or restrictions on the parameter space [4,6,7]. A similar process coupling classical light between optical waveguides has recently been experimentally demonstrated [9–11].

Here we propose a simple experimental setup that fulfills all necessary conditions to observe CTAP for cold atoms. Our proposal is based on radio-frequency (rf) traps, which have recently become one of the most versatile tools for trapping cold atoms [12,13]. The advantage of rf systems is that their physics is well known, they are relatively benign systems to work with experimentally, and they are widely available today. They not only allow us to create standard trapping potentials [12] but can also be used to coherently manipulate matter waves [13,14] or create complicated, nonstandard trapping geometries [15–17].

We will also show that our setup offers the possibility for extending adiabatic techniques to clouds of interacting atoms. The presence of interaction between the atoms introduces nonlinearities into the system [18] which have been shown to inhibit the effectiveness of CTAP in transporting atoms [7]. Several strategies to adjust the process and to allow transport in the presence of these nonlinear interactions have been suggested, for example a fixed detuning between the potential wells [19]. Here we will show that dynamically controlling the detuning between the potentials provides a marked improvement in the state transfer efficiency over both regular and fixed detuning CTAP.

In the following we will first briefly review the idea of CTAP for ultracold atoms. In Sec. III we will outline the theoretical description of rf trapping and describe the system needed for CTAP. In Sec. IV we demonstrate atomic transport in this system and show that the process allows high-fidelity atomic transport in contrast to the intuitive method, which fails. In Sec. V we examine the transport of an interacting atomic cloud and how the presence of nonlinear interaction can be compensated for by dynamic detuning. Finally, in Sec. VI we conclude.

II. COHERENT TRANSPORT ADIABATIC PASSAGE

To briefly review the process of adiabatic population transfer let us consider a system of three ground states in three identical microtraps, $|0\rangle_L, |0\rangle_M$, and $|0\rangle_R$ (see Fig. 1). In a linear arrangement the only tunnel couplings that are significant are J_{LM} for the transition $|0\rangle_L \rightarrow |0\rangle_M$ and J_{MR} for $|0\rangle_M \rightarrow |0\rangle_R$. By assuming that the three states are in resonance when isolated, the Hamiltonian for such a system is given by

$$H(t) = \hbar \begin{pmatrix} 0 & -J_{LM}(t) & 0 \\ -J_{LM}(t) & 0 & -J_{MR}(t) \\ 0 & -J_{MR}(t) & 0 \end{pmatrix} . \qquad (1)$$

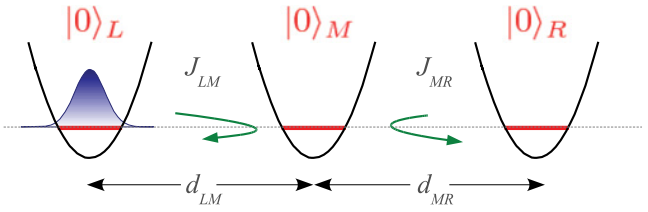

FIG. 1. (Color online) Schematic of the CTAP process for an atom in the left trap. Reducing the distances between the traps leads to an increase in the tunneling strengths.

and a smooth time dependence of the tunneling coupling pulses can be achieved by continuously changing the distances between the traps, $d_{LM}(t)$ and $d_{MR}(t)$. The eigenstates of this Hamiltonian are very well known [3] and of particular interest to our work here is the so-called dark state

$$|d\rangle = \cos\theta|0\rangle_L - \sin\theta|0\rangle_R \tag{2}$$

for which the mixing angle θ is given by

$$\tan\theta = J_{LM}/J_{MR}. \tag{3}$$

This state has a nondegenerate zero eigenvalue and therefore an adiabatic evolution will guarantee that the system, once prepared in $|d\rangle$, will always stay in it. Note that, as the only contribution to $|d\rangle$ from the state $|0\rangle_M$ comes through the mixing angle, the system has zero probability of being found in $|0\rangle_M$ at any time.

The CTAP process can now be understood by considering an atom initially in the state $|0\rangle_L$. Increasing and decreasing J_{MR} before J_{LM}, which is counterintuitive to traditional tunneling schemes, continuously decreases the population in state $|0\rangle_L$ and increases the population in state $|0\rangle_R$, leading to a 100% transfer at the end of the process.

It is worth stressing again the conditions that have to be fulfilled for the above dynamics to occur. First, the process must be adiabatic with respect to the energy level splitting in the harmonic oscillators, which means that the movement of the traps has to be slow and the whole process must take longer than $\omega_{\mathrm{HO}}^{-1}$, where ω_{HO} is the harmonic oscillator frequency of the individual traps. As typical numbers of ω_{HO} for microtraps are in the kilohertz regime, this means that the time required for this process is much shorter than lifetimes of the trapped atoms, which makes this process a promising tool for quantum information. The other condition we require, as previously mentioned, is that all single trap states are in resonance at any point in time, which is difficult to achieve once the trapping potentials start to overlap.

In the next section we will demonstrate how the second condition can be fulfilled in an experimentally realistic system using radio-frequency potentials.

III. RADIO-FREQUENCY TRAPPING

Radio-frequency trapping relies on the process of coupling magnetic sublevels in the presence of an inhomogeneous magnetic field [12–15]. Consider a hyperfine atomic ground state with total spin $F = \frac{1}{2}$. In the presence of a magnetic field the two hyperfine sublevels $m_F = \frac{1}{2}$ and $m'_F = -\frac{1}{2}$ are split by an amount $\mu_B g_F m_F B$, where g_F is the atomic g factor of the hyperfine level and μ_B is the Bohr magneton. Irradiating such a system with a linearly polarized radio frequency, $\mathbf{B}_{\mathrm{rf}}\cos(\omega t)$, couples the sublevels $|\frac{1}{2},\frac{1}{2}\rangle \leftrightarrow |\frac{1}{2},-\frac{1}{2}\rangle$ with spatial resolution due to the spatial dependence of the magnetic field. Here we will concentrate on a one-dimensional (1D) description of such a process, which is valid when the radio frequency and magnetic field are orthogonal to each other. By assuming the inhomogeneous magnetic field to be oriented in the x direction, $B = B(x)$, the Hamiltonian of the coupled system can be written as

$$H(x) = \frac{1}{2}\begin{pmatrix} \mu_B g_F B(x) - \hbar\omega & \hbar\Omega \\ \hbar\Omega & -\mu_B g_F B(x) + \hbar\omega \end{pmatrix}, \tag{4}$$

where the strength of the coupling is given by the Rabi frequency [20]

$$\Omega = \frac{\mu_B g_F}{4\hbar}|\mathbf{B}_{\mathrm{rf}} \times \hat{e}_B|\sqrt{F(F+1) - m_F m'_F}\,, \tag{5}$$

and where $\hat{e}_B$ is the orientation of the local static magnetic field. The eigenvalues of this Hamiltonian are [15]

$$E_\pm(x) = \pm\frac{1}{2}\sqrt{\hbar^2\Omega^2 + [\mu_B g_F B(x) - \hbar\omega]^2}, \tag{6}$$

$$\approx \pm\frac{1}{2}[\mu_B g_F B(x) - \hbar\omega] \pm \frac{\hbar^2\Omega^2}{4[\mu_B g_F B(x) - \hbar\omega]}, \tag{7}$$

where the second expression is valid far from resonance, $\hbar\Omega \ll [\mu_B g_f B(x) - \hbar\omega]$. The second term in the expression can be viewed as a Stark shift on the energy levels.

To create a multiwell potential it is necessary to use several frequencies and the above analysis will become significantly more complicated. However, if we assume that the individual frequencies are spaced sufficiently far apart and have low Rabi frequencies with respect to the detuning, we can approximate the dynamics locally by considering only the nearest resonance frequency, $\omega(x) = \omega_{n(x)}$ [15]. Formally, this means that n is chosen such that $[\mu_B g_F B(x) - \hbar\omega_{n(x)}]$ is minimized at any position x. The effects of the combined Stark shifts, produced by the frequencies not closest to resonance, can then be summed as [15]

$$L_n(x) = \sum_{j\neq n} \frac{\hbar^2\Omega^2}{4[\mu_B g_F B(x) - \hbar\omega_{j(x)}]}, \tag{8}$$

so that the eigenvalues are given by

$$E_\pm(x) = \pm\tfrac{1}{2}\sqrt{\hbar^2\Omega^2 + [\mu_B g_F B(x) - \hbar\omega + 2L_n(x)]^2}. \tag{9}$$

From this, and by considering that the couplings are strong enough to yield a Landau-Zener transition probability close to unity, the resulting adiabatic potential is given by

$$V_{ad,\pm}(x) = (-1)^{n(x)}\left[E_\pm(x) \mp \frac{\hbar\omega_{n(x)}}{2}\right] \mp \sum_{k=1}^{n(x)-1}(-1)^k\hbar\omega_k. \tag{10}$$

To produce a radio-frequency potential with three minima along the x direction we will need six different radio frequencies. In the following we will assume that the 1D linear magnetic field is given by $B(x) = bx$, where b is the magnetic field gradient. For convenience we choose five of the six radio frequencies to be equally spaced initially,

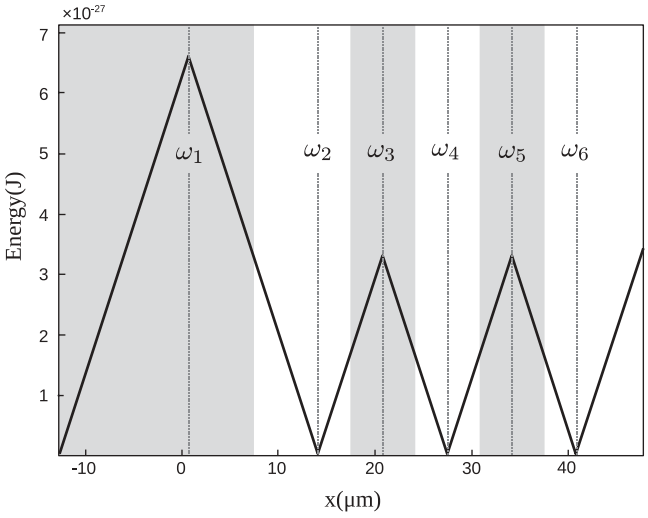

FIG. 2. Trapping potential created by six radio frequencies $\omega_1 = 2\pi \times 1000$ kHz and $\omega_n = 2\pi n \times 10\,000$ kHz, $n = 2 : 6$. Their resonance positions are marked by the broken vertical lines and the range over which they are applied is indicated by the gray and white zones. The magnetic field gradient has strength $b = 160$ G cm^{-1} and $g_F = -\frac{2}{3}$ for the ^{87}Rb ground state $^2S_{\frac{1}{2}}$. The Rabi frequency is chosen to be $2\pi \times 50$ kHz. The traps resemble harmonic oscillator potentials close to each minima.

$\omega_n = 2n\pi \times 10\,000$ kHz ($n = 2 : 6$), which produces three equidistant minima. The first radio frequency ω_1 does need to have the same distance as the other frequencies, as its value only controls the height of the first maximum (see Fig. 2) and can therefore be adjusted without changing the trap geometry in the area where tunneling takes place. For our potential we set $\omega_1 = 2\pi \times 1000$ kHz and in Fig. 2 we indicate the local frequencies and show the resulting adiabatic potential in the positive x direction.

IV. ADIABATIC PASSAGE

In this section we will apply the CTAP procedure to a single atom trapped in a three-well rf potential. We will show that the strong decay of the influence of the radio frequencies away from their respective resonance points allows us to fulfill the resonance condition between the asymptotic eigenstates at all times during the process. While the Stark shift from neighboring resonances cannot be neglected, it is small enough to not destroy the process.

Movement of the traps is achieved by changing the individual radio frequencies that are associated with each trap. Traditionally for CTAP the middle trap is chosen to be at rest and the two outer ones are moving inward and outward (see also Fig. 1). Here we will choose a slightly different, but of course completely analogous, route in that we keep the position of the left trap fixed. This allows us to keep the values of the minima equal, which is essential to satisfy the condition of resonance between all traps.

In order to achieve CTAP when moving the traps in this nontraditional manner the approach of the right trap toward the middle must start earlier than the approach of the middle trap to the left. One therefore initially only changes the frequencies ω_5 and ω_6, which determine the shape and position of the right-hand-side trap. After a delay τ, the two frequencies ω_3 and ω_4 are changed as well, allowing the middle trap to move toward the left. Due to the adiabatic nature of the process the exact shape of this time-dependent frequency adjustment, $f(t)$, does not matter and we can formalize this process as

$$\omega_1(t) = \omega_1(t_0), \tag{11a}$$
$$\omega_2(t) = \omega_2(t_0), \tag{11b}$$
$$\omega_3(t) = \omega_3(t_0) - \tfrac{1}{2} f(t-\tau)\theta(t-\tau), \tag{11c}$$
$$\omega_4(t) = \omega_4(t_0) - f(t-\tau)\theta(t-\tau), \tag{11d}$$
$$\omega_5(t) = \omega_5(t_0) - \tfrac{1}{2} f(t) - f(t-\tau)\theta(t-\tau), \tag{11e}$$
$$\omega_6(t) = \omega_6(t_0) - f(t) - f(t-\tau)\theta(t-\tau), \tag{11f}$$

where $\theta(t)$ is the Heaviside step function. In Fig. 3(a) these changes are shown for the typical system considered here and the resulting movements of the trap minima are displayed in Fig. 3(b). As can been seen, the minimum of the left trap remains stationary while the other traps are moving toward and away from it. The resulting movement between neighboring traps exactly fulfills the requirement of the CTAP process, leading to the desired increase and decrease in the tunneling strength between initially the middle and right traps before the increase and decrease in tunneling strength between the left and middle traps.

To demonstrate adiabatic passage for single atoms and for typical experimentally realistic parameters, we will in the following show the results of numerical simulations of the full Schrödinger equation. We choose a single ^{87}Rb atom to be initially located in the center-of-mass ground state of the left trap and start the process described in Sec. IV with an initial separation between the radio frequencies of $2\pi \times 10\,000$ kHz. The minimum distance to which the frequencies approach each other is $2\pi \times 200$ kHz, which ensures that we are always in the regime of tunneling interaction, as the minimum barrier height

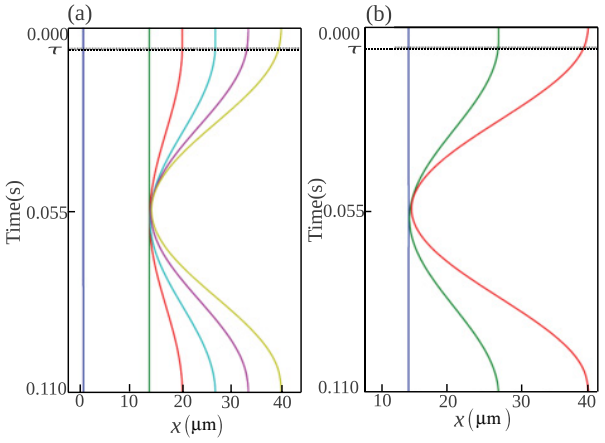

FIG. 3. (Color online) (a) Radio frequencies, ω_n, as a function of time to achieve the counterintuitive positioning sequence. (b) Positions of the trap minima as a function of time. The left trap remains stationary while the other two traps move toward it. The delay in the movement of the middle trap in comparison to the right trap ($\tau = 0.0055$ s) is indicated by the broken line.

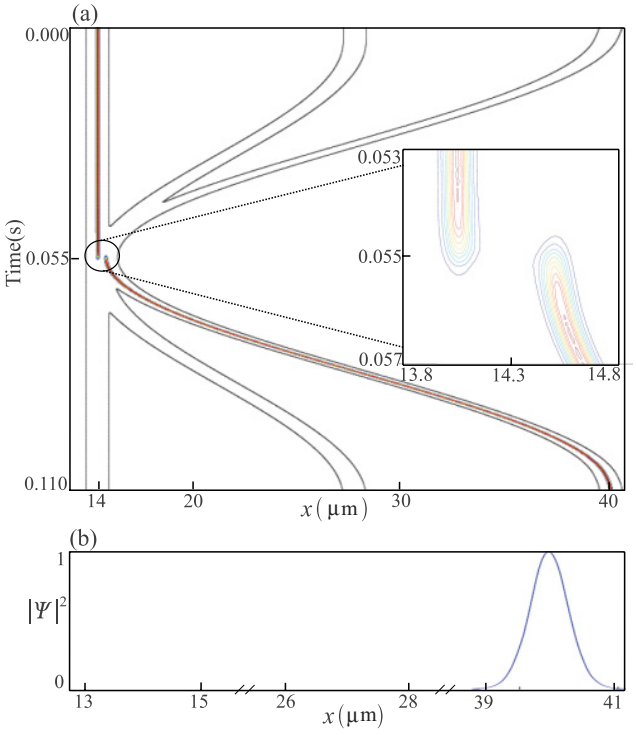

FIG. 4. (Color online) (a) Probability density for a single atom initially located in the trap on the left-hand side with respect to time for counterintuitive trap movement. The inset shows the tunneling area in greater detail. (b) Density of the final state in each of the three traps.

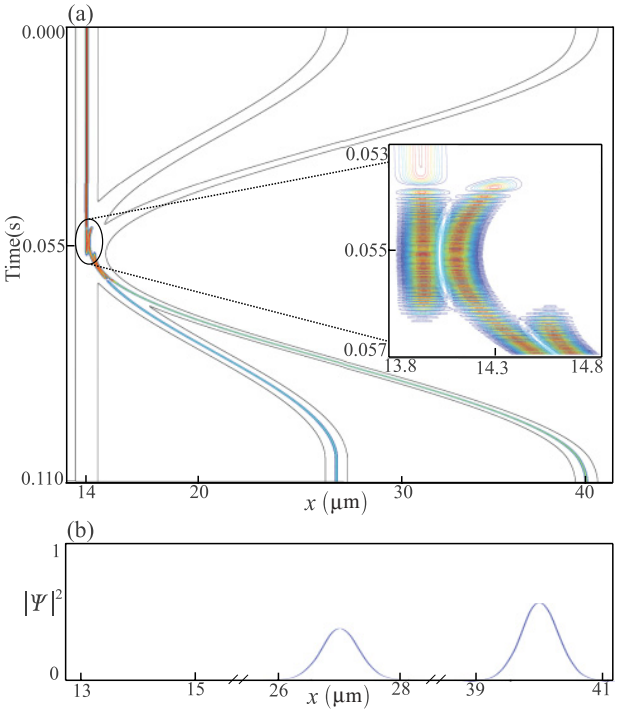

FIG. 5. (Color online) (a) Probability density for a single atom initially located in the trap on the left-hand side with respect to time for intuitive trap movement. The inset shows the tunneling area in greater detail, where Rabi oscillations between neighboring traps are clearly visible. (b) Density of the final state in each of the three traps.

between the individual traps is 5.3313×10^{-29} J at the point of closest approach, compared to the ground-state energy of 1.3615×10^{-29} J. The form of the adjustment function $f(t)$ is taken to be a cosine and for numerical simplicity we restrict ourselves to one spatial dimension.

In Fig. 4 we show the probability density function with respect to time for the CTAP process. The overall time for this process is chosen to be $T = 0.11$ s, which is large compared to the approximate harmonic oscillator frequency of the individual traps of $\omega_{\mathrm{HO}}^{-1} \approx 4 \times 10^{-6}$ s, and we are therefore assured that the system is at all times in the dark eigenstate. This can also be seen from the fact that the probability for being in the middle trap at any time is zero. The process leads to high-fidelity population transfer and an absence of Rabi oscillations.

To compare the above situation to a process in which direct tunneling between two neighboring traps plays an important role, we show in Fig. 5 the results of the same process, this time however using an intuitive trap movement. The direct tunneling is clearly manifest in the appearance of Rabi oscillations between the traps and the process therefore does not deliver the required robust population transfer. In fact, the final state becomes highly susceptible to variations of the system parameters [21].

We have confirmed that these results are representative for a large range of parameters, making rf traps ideal systems to investigate general adiabatic processes.

V. NONLINEAR SYSTEMS

The extension of adiabatic methods to nonlinear systems is of great importance not only to describe experimental situations but also for the understanding of the underlying physical principles [18,19,22,23]. In this section we show how CTAP can be used with time-dependent potentials to coherently transport a cloud of interacting, Bose-condensed atoms. For this, we treat the adiabatic process as a series of stationary states which can be described by the time-independent Gross-Pitaevskii equation

$$\mu\Psi(x) = \left(-\frac{\hbar^2}{2m}\nabla^2 + V(x) + g_{1D}|\Psi|^2\right)\Psi(x), \quad (12)$$

where $V(x)$ is the external potential and μ is the chemical potential at each respective point in time. The one-dimensional interaction strength between bosons with a three-dimensional s-wave scattering length a_s is given by $g_{1D} = \frac{4N\hbar^2 a_s}{m a_\perp}(a_\perp - Ca_s)^{-1}$ [24]. The trap width in the radial direction is given by $a_\perp$ and $C \approx 1.4603$. In the three-level approximation the Hamiltonian can therefore be written as

$$H(t) = \hbar \begin{pmatrix} \hbar\omega_L + \mu_L & -J_{LM}(t) & 0 \\ -J_{LM}(t) & \hbar\omega_M & -J_{MR}(t) \\ 0 & -J_{MR}(t) & \hbar\omega_R + \mu_R \end{pmatrix}, \quad (13)$$

where μ_L and μ_R are the chemical potentials associated with the atomic clouds in the left or right trap, respectively, and ω_L, ω_M, and ω_R are the harmonic oscillator frequencies associated

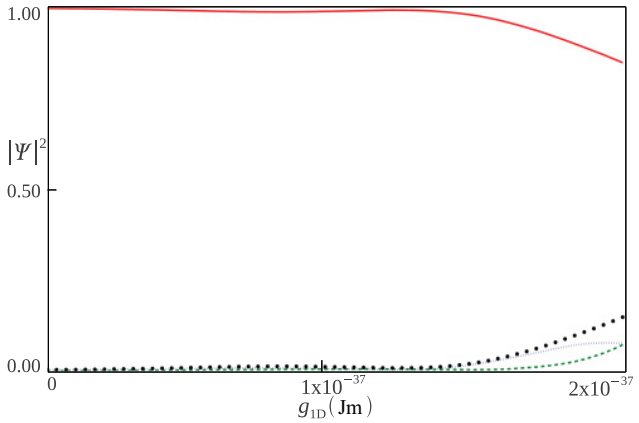

FIG. 6. (Color online) Final population in left (vertical dashed line, blue), middle (horizontal dashed line, green), and right (solid line, red) traps with increasing interaction strength. The dotted black line shows the total population not occupying the target (right) trap. The maximum value of g_{1D} corresponds to $\mu = 1.4318 \times 10^{-29}$ J, which is smaller than $\hbar\omega_{L,M,R}$ at all times.

with the individual traps. Note that this Hamiltonian has been extensively investigated for constant couplings between the traps [25,26]. As the particle number in each individual trap is a function of time, the chemical potentials μ_i will change and destroy the resonances between the traps. To compensate for this we will in the following allow for the trapping frequencies to be functions of time as well. Starting with a cloud of atoms in the left trap, it is clear that the chemical potential μ_L will decrease durning the process, while μ_R will increase. Adjusting the trapping frequencies ω_L and ω_R can restore the resonance between the uncoupled traps by ensuring that $\hbar\omega_i + \mu_i \approx$ constant at all times. However, in order to be able to make the three-state approximation, we need to make sure that $\mu_i < \hbar\omega_i$ for all values of μ_i and ω_i. This means in practice that the process is limited to cold atomic clouds with small nonlinearities.

Using the same radio-frequency potential as in the linear case, we place a cloud of interacting ^{87}Rb atoms in the ground state of the left trap by determining the solution to the Gross-Pitaevskii equation for an isolated trapping potential. To show the influence of the nonlinear behavior, we first carry out the same counterintuitive trap movements as in the linear section without time-dependent change in the trapping frequencies. In Fig. 6 we show the final populations in the individual traps as a function of increasing values for g_{1D}. It is immediately obvious that even for weak interactions the nonlinear term is disruptive to the process of CTAP. In fact, for $g_{1D} = 2 \times 10^{-37}$ J m the state transfer efficiency is reduced to 84%. By choosing a typical radial trap width of 130 nm, this value of g_{1D} corresponds to $N = 2$ for ^{87}Rb.

As outlined above, to restore resonance in the presence of a changing chemical potential we must adjust the trapping frequency so that at any point in time $\hbar\omega_L(t) + \mu_L(t) = \hbar\omega_M = \hbar\omega_R(t) + \mu_R(t)$. However, determining the required adjustments is not a simple exercise for at least two reasons. First, the density dependence of the chemical potential will prevent this change from simply being linear in time, and, second, a conceptual difficulty in determining the individual chemical potentials arises when the traps are close together. While one could try to calculate the chemical potential, and therefore the on-site energies, in all traps at all times to a good approximation, this is certainly not experimentally possible. In the following, we therefore suggest a simple functional form for dynamically detuning the outer traps and we show that it allows us to achieve significantly higher transfer than possible without adjustments. A similar idea, however without time dependence, was recently proposed by Graefe *et al.* [19], who showed that by detuning the left and the right traps by the same fixed amount throughout the process an improved transfer of population can be achieved.

The outline of our scheme for dynamic detuning is as follows. Initially the cloud is trapped in the left trap, which we detune such that resonance with the eigenstates of the other two traps is ensured (since the traps are far apart, it is possible to determine the chemical potential μ_L). As we time evolve the system, tunneling sets in and we begin to reduce the detuning on the left trap to zero while increasing the detuning of the right trap, as atoms enter it. This can be achieved by adjusting the radio frequencies ω_2 and ω_6, associated with the left- and right-hand-side traps, respectively. Here we suggest that a good form of function for the adjustment related to the left-hand-side trap is

$$\Delta\omega_2(\kappa;\tilde{t}) = \tfrac{1}{2}[1 - \tanh(\kappa\tilde{t})]\Delta\omega_0, \tag{14}$$

where the initial value for the change in ω_2 is given by ω_0. The function runs between $\Delta\omega_0$ and 0 and the steepness in the crossover region is determined by κ. This gives us an effective handle on both the time when the adjustment starts and the duration of the adjustment (see inset of Fig. 7). Here $\tilde{t} = t - T/2$, with T being the overall duration of the process. At the same time the frequency of the right-hand-side trap

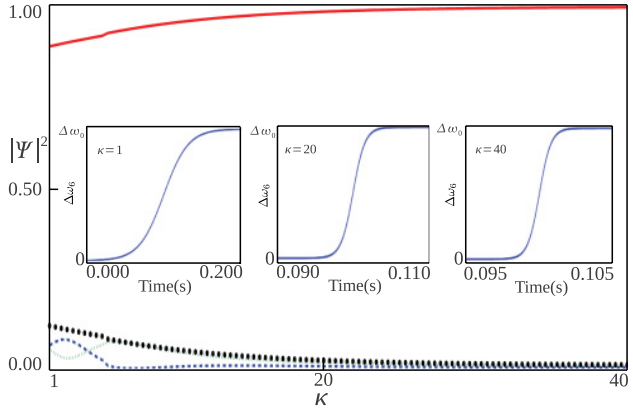

FIG. 7. (Color online) Final population in left (horizontal dashed blue line), middle (vertical dashed green line), and right (solid red line) traps for nonlinear CTAP with increasing κ and $\Delta\omega_0 = 2\pi \times 1.5$ kHz. The dotted black line shows the total population not occupying the target (right) trap. The insets show the shape of $\Delta\omega_6(\kappa;\tilde{t})$ for different values of κ. An increased value of κ increases the time when the adjustment begins and decreases the adjustment time.

needs to be adjusted as well and it is easy to see that a mirror-symmetric change in ω_6 is the best choice:

$$\Delta\omega_6(\kappa;\tilde{t}) = \tfrac{1}{2}[1+\tanh(\kappa\tilde{t})]\Delta\omega_0, \tag{15}$$

The dynamic adjustments of the radio-frequency equations (IV) then become

$$\omega_1(t) = \omega_1(t_0), \tag{16a}$$
$$\omega_2(t) = \omega_2(t_0) - \Delta\omega_2(\kappa,\tilde{t}), \tag{16b}$$
$$\omega_3(t) = \omega_3(t_0) - \tfrac{1}{2}f(t-\tau)\theta(t-\tau), \tag{16c}$$
$$\omega_4(t) = \omega_4(t_0) - f(t-\tau)\theta(t-\tau), \tag{16d}$$
$$\omega_5(t) = \omega_5(t_0) - \tfrac{1}{2}f(t) - f(t-\tau)\theta(t-\tau), \tag{16e}$$
$$\omega_6(t) = \omega_6(t_0) - f(t) - f(t-\tau)\theta(t-\tau) + \Delta\omega_6(\kappa,\tilde{t}). \tag{16f}$$

In Fig. 7 we show the final population transferred to the right trap for increasing values of κ and for $\Delta\omega_0 = 2\pi \times 1.5$ kHz. We can see that the dynamic adjustment of the detunings of the outer traps allows us to achieve population transfer of >99%, up from 84%. This is an improvement over both standard CTAP and fixed detuning in the weak-interaction regime and, in fact, returns to the transfer efficiency of single-particle CTAP.

VI. CONCLUSIONS

We have shown that radio-frequency traps can be used as microtraps for processes in which an adjustable tunneling strength is required. Neighboring trapping potentials can be overlapped without significantly changing the underlying energy level structure. This property has allowed us to create a triple-well radio-frequency potential in which coherent transport using adiabatic passage can be demonstrated. For a single atom, it was shown that complete transfer between the left and right traps by utilizing the dark state of the system is possible, maintaining the advantages of an absence of Rabi oscillations and robustness against variation in system parameters.

For a cloud of weakly interacting atoms we have demonstrated a technique that significantly improves the efficiency of CTAP by dynamically detuning the outer traps. Our suggested setup is close to experimental realities, avoids the large overhead of other suggestions, and can easily be extended to other adiabatic techniques.

ACKNOWLEDGMENTS

The authors would like to thank Peter Krüger and Thomas Fernholz for valuable discussions. This work was supported by Science Foundation Ireland under Projects No. 05/IN/I852 and No. 10/IN.1/I2979. BOS acknowledges support from IRCSET through the Embark Initiative No. RS/2006/172.

[1] M. A. Nielsen and I. L. Chuang, *Quantum Computation and Quantum Information* (Cambridge University Press, Cambridge, 2000).
[2] A. M. Steane, Phys. Rev. Lett. **77**, 793 (1996).
[3] K. Bergmann, H. Theuer, and B. W. Shore, Rev. Mod. Phys. **70**, 1003 (1998).
[4] K. Eckert, M. Lewenstein, R. Corbalán, G. Birkl, W. Ertmer, and J. Mompart, Phys. Rev. A **70**, 023606 (2004).
[5] A. D. Greentree, J. H. Cole, A. R. Hamilton, and L. C. L. Hollenberg, Phys. Rev. B **70**, 235317 (2004).
[6] K. Eckert, J. Mompart, R. Corbalán, M. Lewenstein, and G. Birkl, Opt. Commun. **264**, 264 (2006).
[7] M. Rab, J. H. Cole, N. G. Parker, A. D. Greentree, L. C. L. Hollenberg, and A. M. Martin, Phys. Rev. A **77**, 061602 (2008).
[8] B. O'Sullivan, P. Morrissey, T. Morgan, and Th. Busch, Phys. Scr. T **140**, 014029 (2010).
[9] S. Longhi, Phys. Rev. E **73**, 026607 (2006).
[10] S. Longhi, G. Della Valle, M. Ornigotti, and P. Laporta, Phys. Rev. B **76**, 201101(R) (2007).
[11] A. A. Rangelov, N. V. Vitanov, and B. W. Shore, J. Phys. B **42**, 055504 (2009).
[12] O. Zobay and B. M. Garraway, Phys. Rev. Lett. **86**, 1195 (2001).
[13] T. Schumm, S. Hofferberth, L. M. Andersson, S. Wildermuth, S. Groth, I. Bar-Joseph, J. Schmiedmayer, and P. Krüger, Nature Phys. **1**, 57 (2005).
[14] S. Hofferberth, B. Fischer, T. Schumm, J. Schmiedmayer, and I. Lesanovsky, Phys. Rev. A **76**, 013401 (2007).
[15] Ph. W. Courteille, B. Deh, J. Fortágh, A. Günther, S. Kraft, C. Marzok, S. Slama, and C. Zimmermann, J. Phys. B **39**, 1055 (2006).
[16] I. Lesanovsky, T. Schumm, S. Hofferberth, L. M. Andersson, P. Krüger, and J. Schmiedmayer, Phys. Rev. A **73**, 033619 (2006).
[17] T. Fernholz, R. Gerritsma, P. Krüger, and R. J. C. Spreeuw, Phys. Rev. A **75**, 063406 (2007).
[18] J. Liu, B. Wu, and Q. Niu, Phys. Rev. Lett. **90**, 170404 (2003).
[19] E. M. Graefe, H. J. Korsch, and D. Witthaut, Phys. Rev. A. **73**, 013617 (2006).
[20] W. Ketterle and N. J. van Druten, Adv. Mol. Opt. Phys. **37**, 181 (1996).
[21] J. Mompart, K. Eckert, W. Ertmer, G. Birkl, and M. Lewenstein, Phys. Rev. Lett. **90**, 147901 (2003).
[22] A. Smerzi, S. Fantoni, S. Giovanazzi, and S. R. Shenoy, Phys. Rev. Lett. **79**, 4950 (1997).
[23] I. Marino, S. Raghavan, S. Fantoni, S. R. Shenoy, and A. Smerzi, Phys. Rev. A **60**, 487 (1999).
[24] M. Olshanii, Phys. Rev. Lett. **81**, 938 (1998).
[25] G.-F. Wang, D.-F. Ye, L.-B. Fu, X.-Z. Chen, and J. Liu, Phys. Rev. A **74**, 033414 (2006).
[26] B. Liu, L.-B. Fu, S.-P. Yang, and J. Liu, Phys. Rev. A **75**, 033601 (2007).

PHYSICAL REVIEW A **85**, 039904(E) (2012)

Erratum: Coherent adiabatic transport of atoms in radio-frequency traps [Phys. Rev. A 83, 053620 (2011)]

T. Morgan, B. O'Sullivan, and Th. Busch

(Received 6 March 2012; published 14 March 2012)

DOI: 10.1103/PhysRevA.85.039904 PACS number(s): 03.75.−b, 05.60.Gg, 67.85.−d, 99.10.Cd

In our paper the values $g_f = -\frac{2}{3}$ and $b = 160\ \mathrm{G\,cm^{-1}}$ in Fig. 2 are incorrect. The correct values are $g_f = -\frac{1}{2}$ and $b = 213\ \mathrm{G\,cm^{-1}}$. The conclusions of our paper are not affected.

The authors would like to thank Professor Chris Foot for bringing this error to our attention.

Chapter 5

Floquet Theory for Modelling Adiabatic Radio Frequency Potentials

As was discussed in Chapter 4, adiabatic radio frequency potentials have in recent years become versatile experimental tools for trapping and controlling ultracold atoms [27, 28, 89]. They allow the creation of non-standard trapping potentials [26, 29, 99, 100] and can also be time-dependent to allow dynamical manipulation of matter waves [26, 28, 89]. However, most of the previously mentioned studies only use a single rf field to create the adiabatic rf potential, and only a few extensions to multiple rf fields of different frequencies have been discussed. Such multi-frequency systems allow for more complex potentials and higher control.

One example of a potential shape that can be created using a single rf is the annular trap for studies of rotating BECs [103]. By adding additional rf fields one can, for example, create potentials consisting of multiple concentric rings with frequency dependent spacings, thus giving control over the tunnel coupling between neighbouring rings. In such systems it is possible to study rotational fluxons (Josephson vortices) [104] or the Kibble-Zurek mechanism [105].

However, while exact treatments exist for adiabatic rf potentials of a single frequency, when multiple fields are present the removal of time dependence from the Hamiltonian of the system becomes highly non-trivial and approximations such as the rotating wave approximation (RWA) must be made. In the manuscript contained in this Chapter, we show how Floquet theory can be used to remove the time-dependence from the

Hamiltonian without having to perform the RWA [1]. This in turn allows higher order couplings of the atomic hyperfine states to be taken into account and we show that the subsequently generated adiabatic rf potentials are significantly more accurate than previously discussed approaches [29].

Floquet theory was developed by Gaston Floquet [30] but it was first shown by Shirley that it could be used to describe interaction of a quantum system with an oscillating field [31]. Subsequently, Ho *et al.* demonstrated that its application could be extended to systems with multiple oscillating fields [62] including multi-photon processes for atoms interacting with strong laser fields [106]. Since its development, Floquet theory has been applied to a large number of systems such as nuclear magnetic resonance [107, 108], adiabatic passage in optical systems [109] and intense frequency-comb laser fields [110]. A comprehensive overview of the application of Floquet theory to atomic and molecular multiphoton processes in intense laser fields can be found in [61].

[1] The work in this manuscript was done in collaboration with Thomas Fernholz. Each author contributed to all areas of the manuscript.

5.1 Floquet Theory for Modelling Adiabatic Radio Frequency Potentials

Manuscript Information

Manuscript Title: Floquet Theory for modelling adiabatic radio frequency potentials.
Journal Information: In preparation.
Authors: Tadhg Morgan, Thomas Fernholz and Thomas Busch.
Pages: 10.
Figures: 6.

Floquet Theory for modelling adiabatic radio frequency potentials

T. Morgan* and Th. Busch
Quantum Systems Unit, Okinawa Institute of Science and Technology, Okinawa, Japan and Department of Physics, National University of Ireland, UCC, Cork, Ireland

T. Fernholz
School of Physics & Astronomy, The University of Nottingham, University Park, Nottingham, NG7 2RD, UK

Adiabatic radio frequency (RF) potentials are powerful tools for creating advanced trapping geometries for ultra-cold atoms. While the basic theory of RF trapping is well understood, studies of more complicated setups involving multiple resonant frequencies in the limit where their effects cannot be treated independently are rare. Here we present an approach based on Floquet theory to describe the adiabatic potential experienced by an atom subjected to a RF field of multiple frequencies. We show that the Floquet approach offers corrections to existing models and significant accuracy enhancements when the frequencies are near degenerate. This model has no restrictions on the dimension or number of frequencies and can also be used to describe RF fields of arbitrary polarization. We show that these added degrees of freedom can, for example, be used to create a potential in which ring vortex solitons can be observed.

I. INTRODUCTION

Using resonant RF radiation to address the spins of atoms in inhomogeneous magnetic fields allows to locally address clouds of ultracold atoms with high spatial resolution. This technique is commonly used in combination with atom chips, a pairing which offers huge flexibility in the types of potentials that can be created [1, 2]. Being able to make the RF fields time dependent is adding to the versatility and has, for example, been used to split Bose-Einstein condensates (BECs) [3]. By today significant work has been done in the modelling of RF systems to create highly non trivial trapping geometries [4, 5], including annular traps [6], examine effects beyond the rotating wave approximation [7] and investigating nonlinear Zeeman effects [8].

The use of multi-frequency fields has recently been suggested to create multi-well or even periodic potentials [9, 11]. These can be periodic and time dependent and in [11] a method to coherently control the centre of mass motion of both a single atom and a cloud of interacting atoms was suggested. While this work highlighted how versatile multi-frequency RF potentials are for experimentally realistic parameters, the theoretical model used did not allow to investigate situations in which two frequencies come so close that their effects can no longer be treated independently.

The use of multi-frequency fields has recently been suggested to create multi-well or even periodic potentials [9, 11]. These can be periodic and time dependent and in [11] a method to coherently control the centre of mass motion of both a single atom and a cloud of interacting atoms was suggested. While this work highlighted how versatile multi-frequency RF potentials are for experimentally realistic parameters, the theoretical model used could only describe limited tunnel coupling strengths between two potential wells, as it required all radio frequencies to be well separated. For large tunnel couplings, however, it is usually necessary to have potentials where the curvature can be controlled over short distances, which, using rf technology, requires two frequencies to be brought close. In such situations the effects of both frequencies have to be considered simultaneously and a more advanced model is necessary.

To address the question of how to accurately deal with near degenerate frequencies and take full advantage of all degrees of freedom offered by RF fields, in this work we investigate the use of Floquet theory and compare the results to the models recently used [9]. Floquet theory allows to describe the interaction between a periodically oscillating field and a quantum system and its basic idea is to replace the semiclassical time-dependent Hamiltonian with a time-independent Hamiltonian of infinite dimensions [12]. By using a Floquet approach to model RF systems, we will show that highly accurate potentials can be obtained.

Since its first application to single mode systems, Floquet theory has been extended to many-mode systems [13] and has been extensively used in studying multiphoton processes for atoms in strong laser fields [14]. In [15] Floquet theory was used to describe adiabatic potentials produced by short laser pulses in order to stimulate a STIRAP (Stimulated Raman Adiabatic Passage) process. This was more recently extended to a many-mode Floquet theorem allowing to study multiphoton resonance dynamics driven by intense frequency-comb laser fields [16]. A comprehensive overview of the application of Floquet theory to atomic and molecular multiphoton processes in intense laser fields can be found in [17].

The layout of this paper is as follows. In Sec. II we consider the general Hamiltonian of atom confined to a static magnetic field which is irradiated with an RF field of a single frequency and show how the exact eigenvalues

* tmorgan@phys.ucc.ie

can be obtained. In Sec. III we review the model developed in [9], which we refer to as the piecewise resonance model, for adiabatic RF potentials created with multiple RF fields and highlight how it breaks down when two frequencies become too close. In Sec. IV we show how Floquet theory can be used to obtain a more accurate description and in Sec. VI we compare the two approaches and discuss the corrections and benefits of the Floquet approach. To demonstrate the power of the approach, we detail in Sec. VI B how an extension to higher dimensions can be done and show how controlling the orientation of the RF field can be used to produce non trivial trapping geometries. As an example, we show how controlling the tunnel coupling in multidimensional RF traps can allow ring vortex solitons in Bose-Einstein condensates to be created. Finally in Sec. VII we conclude.

II. RADIO-FREQUENCY DRESSED TRAPS

RF trapping is based on the idea of coupling magnetic sublevels in the presence of an inhomogeneous magnetic field. Consider a hyperfine atomic ground state manifold with total spin F. In the presence of a static magnetic field of modulus B_s, the Zeeman sublevels, $m_F = -F, ..., F$ undergo a linear splitting according to $E_{m_F} = m_F g_F \mu_B B_s$, as long as the field strength is not too large. Here, g_F is the atomic g-factor and μ_B is the Bohr magneton. Irradiating such a system with a radio frequency $\mathbf{B}_{\mathrm{RF}}(\omega t)$, which can excite atomic Larmor precession, will couple the sublevels $|F, m_F\rangle \leftrightarrow |F, m_F \pm 1\rangle$ with spatial resolution due to the spatial dependence of the magnetic field and varying Larmor frequency.

For simplicity, we first consider a one-dimensional situation with a static field pointing and increasing linearly along the z-direction, i.e. $B_s = B_s(z) = Gz$ where G is the magnetic field gradient. Such a situation arises, for example, when an atom travels along an axis of a quadrupole field. It is convenient to express the oscillating field in complex spherical components (σ^+, σ^-, and π-polarizations), such that

$$\mathbf{B}_{\mathrm{RF}}(\omega t) = \mathrm{Re}\left[\begin{pmatrix} \frac{1}{\sqrt{2}}(B_+ + B_-) \\ \frac{i}{\sqrt{2}}(B_+ - B_-) \\ B_\pi \end{pmatrix} \cdot e^{-i\omega t}\right], \qquad (1)$$

and the total Hamiltonian for the magnetic interaction can be written as

$$H(z,t) = \mu_B g_F \mathbf{F} \cdot (\mathbf{B}_s(z) + \mathbf{B}_{\mathrm{RF}}(\omega t)) . \qquad (2)$$

Transforming to a frame rotating about the z-axis at frequency ω using $H_{\mathrm{rot}} = i\hbar \dot{U} U^{-1} + U H U^{-1}$ with $U = e^{iF_z \omega t}$ leads to $H_{\mathrm{rot}} = \mu_B g_F \mathbf{F} \cdot \mathbf{B}_{\mathrm{eff}}$, where the effective field in Cartesian coordinates is given by,

$$\mathbf{B}_{\mathrm{eff}} = \begin{pmatrix} \frac{1}{\sqrt{2}}\mathrm{Re}[B_- e^{-i2\omega t}] + \frac{1}{\sqrt{2}}\mathrm{Re}[B_+] \\ \frac{1}{\sqrt{2}}\mathrm{Im}[B_- e^{-i2\omega t}] - \frac{1}{\sqrt{2}}\mathrm{Im}[B_+] \\ \mathrm{Re}[B_\pi e^{-i\omega t}] + B_s(z) - \frac{\hbar\omega}{\mu_B g_F} \end{pmatrix}. \qquad (3)$$

Expressing the Hamiltonian in the spherical basis then results in $H_{\mathrm{rot}} = \mu_B g_F (F_+ B_+^* + F_- B_-^* e^{i2\omega t} + F_z (B_\pi^* e^{i\omega t} + B_s(z) - \frac{\hbar\omega}{\mu_B g_F})) + c.c.$

If the RF field is purely σ^+-polarized, the Hamiltonian becomes time-independent and the situation in the rotating frame is fully equivalent to an atom moving in an inhomogeneous field across a non-zero field minimum. Conversely, the widely used Ioffe-Pritchard type trap, where the field-zero of a 2D quadrupole field is lifted with an orthogonal applied field B_I, can be viewed as a dressed state trap with zero coupling frequency. The quasi-energies, i.e., the eigenvalues of the rotating frame Hamiltonian can be obtained straightforwardly as

$$\begin{aligned} E_{m_F} &= m_F \mu_B g_F B_{\mathrm{eff}} \qquad (4) \\ &= m_F \mu_B g_F \sqrt{\left(B_s(z) - \frac{\hbar\omega}{\mu_B g_F}\right)^2 + |B^+|^2} , \end{aligned}$$

where the m_F are eigenvalues of the spin component aligned with the effective field.

If polarization components other than σ^+ are present, one can perform the rotating wave approximation (RWA) and discard the fast oscillating terms as long as $\hbar\omega \gg g_F \mu_B B_{\mathrm{eff}}$ [18]. This however, leads to neglecting shifts in the energy spectrum, which are known as Bloch-Siegert shifts [10]. A second order correction is caused by a σ^- field component, which can be seen as equivalent to a σ^+ polarized field at negative frequency and cause off-resonant coupling between states with $\Delta m_F = \pm 1$ (see Fig. 1). Other higher order effects can also stem from π polarised components.

III. PIECEWISE RESONANCE MODEL

More control and complexity can be introduced into RF dressed potentials by using multiple frequencies ω_n. Using the method outlined above, one can in principle apply an iterative procedure by performing consecutive rotating wave approximations for each frequency. However, it is then necessary at each step to transform all oscillating fields into the new rotating frame and determine new polarization components with respect to the effective field of the previous step. This procedure will lead to an accumulation of errors and can suffer from a certain arbitrariness as the order of eliminating individual frequencies is not defined.

However, if the individual frequencies are spaced sufficiently far apart and the coupling is small with respect to the detuning, one can approximate the dynamics locally by considering only the nearest resonance frequency, $\omega(z) = \omega_n$ [9]. Formally this means that n is chosen such that $[\mu_B g_F B_s(z) - \hbar\omega_n]$ is minimized at any position z. In the language of the above consecutive approach, this is equivalent to approximating the effective field by its z-component before decomposing polarisation components for the next step.

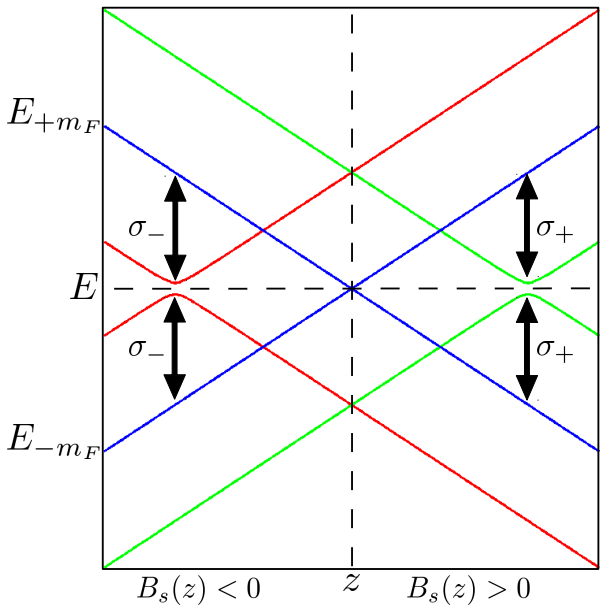

FIG. 1. A schematic diagram of the eigenvalues of the Hamiltonian in the rotating frame for both, σ_+ (green lines) and σ_- (red lines) polarised RF fields irradiating an atom in a linear static field $B_s(z) = Gz$. The blue lines show the bare Hamiltonian eigenvalues E_{+m_F} and E_{-m_F}. The dashed black lines indicate where $z = 0$ and $E = 0$.

With this local frequency approximation the Hamiltonian (2) for a system of total spin $F = \frac{1}{2}$ after the RWA has been applied is

$$H(z) = \frac{1}{2}\begin{pmatrix} \mu_B g_F B_s(z) - \hbar\omega_n & \hbar\Omega_n \\ \hbar\Omega_n^* & -\mu_B g_F B_s(z) + \hbar\omega_n \end{pmatrix}, \tag{5}$$

where $\Omega_n = \frac{\mu_B g_F}{4\hbar}\left(B_{n_x} + iB_{n_y}\right)$ is the Rabi frequency of the n^{th} RF field with B_{n_x} and B_{n_y} the component of the field along the x and y Cartesian directions, respectively. Here we will restrict ourselves to considering linearly polarised RF fields orthogonal to the static field so that $\Omega = \frac{\mu_B g_F}{4\hbar} B_{n_x}$. The change to a Cartesian basis is done so as to match the method outlined in [9].

For large detuning the eigenenergies of this Hamiltonian can be written as [9],

$$\begin{aligned} E_\pm(z) &= \pm\frac{1}{2}\sqrt{\hbar^2\Omega^2 + [\mu_B g_F B_s(z) - \hbar\omega_n]^2} \\ &\approx \pm\frac{1}{2}[\mu_B g_F B_s(z) - \hbar\omega_n] \pm \frac{\hbar^2\Omega^2}{4[\mu_B g_F B_s(z) - \hbar\omega_n]}, \end{aligned} \tag{6}$$

where the second step is valid far from the resonance, $\hbar\Omega \ll [\mu_B g_F B(z) - \hbar\omega_n]$ and the resulting second term can be viewed as a Stark shift. The effect of all other RF fields which are not closest to resonance can be approximated by creating an effective Stark shift, which is the sum of the Stark shifts of all RF fields of frequency ω_j $(j \neq n)$ [9],

$$L_n(z) = \sum_{j\neq n} \frac{\hbar^2\Omega^2}{4[\mu_B g_F B_s(z) - \hbar\omega_j]}. \tag{7}$$

This leads to a correction of the eigenvalues, which are now given by

$$E_\pm(z) = \pm\frac{1}{2}\sqrt{\hbar^2\Omega^2 + [\mu_B g_F B_s(z) - \hbar\omega + 2L_n(z)]^2}. \tag{8}$$

From this, and considering that the couplings are strong enough to yield a Landau-Zener transition probability close to unity, the resulting adiabatic potential is given by

$$V_{ad\pm}(z) = (-1)^n\left[E_\pm(z) \mp \frac{\hbar\omega_n}{2}\right] \mp \sum_{k=1}^{n-1}(-1)^k\hbar\omega_k. \tag{9}$$

In Fig. 2 we show the adiabatic RF potentials seen by an atom trapped in a Ioffe-Pitchard (IP) trap irradiated by a linearly polarised RF field with two frequencies, ω_1 and ω_2, for three different values of $\Delta\omega = \omega_2 - \omega_1$. In all work presented here we assume that the IP trap has the form of

$$B_s(r) = \sqrt{G^2 \times r^2 + B_I^2}, \tag{10}$$

with values for the magnetic field gradient $G = 1Tm^{-1}$ and the applied field $B_I = 1\mu T$ in the typical range applicable to an atom chip.

While for well spaced frequencies the potential resulting from the above procedure is visually smooth (see Fig. 2 (a)), a discontinuity appears for decreasing values of $\Delta\omega$, which grows as the frequencies approach each other further. Treating the RF fields independently from each other is therefore no longer appropriate and in order to be able to describe these situations we will explore the advantages a treatment using Floquet theory offers. Situations in which this becomes important are, for example, potentials in which the curvature changes on a small spatial scale.

While for well spaced frequencies the potential resulting from the above procedure is visually smooth (see Fig. 2 (a)), a discontinuity appears for decreasing values of $\Delta\omega$, which grows as the frequencies approach each other further. Such discontinuities mean that the piecewise resonance model cannot be applied to situations where control over the potential curvature on small length-scales is necessary, as for example is the case when trying to control a tunnelling strength. To treat the influence that several closely spaced RF have on each other, we will in the following describe the advantages and limits a treatment using Floquet theory offers.

IV. FLOQUET MODEL

Floquet theory provides a practical and powerful non-perturbative method for studying the interaction of a

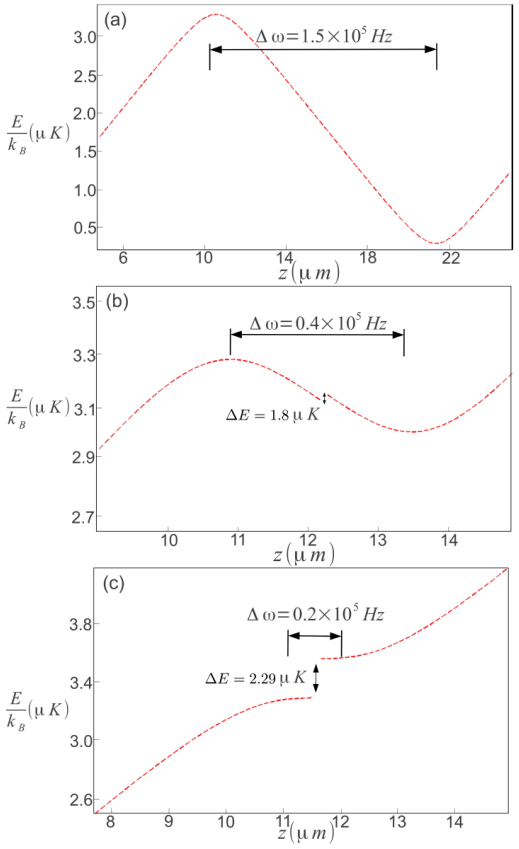

FIG. 2. Adiabatic RF potentials for an atom trapped in a IP trap irradiated by linearly polarised, two frequency RF fields with different frequency separation $\Delta\omega$ with $\omega_1 = 1.5 \times 10^5$ Hz and Rabi frequencies $\Omega_1 = \Omega_2 = 9.274 \times 10^4$ Hz. Note that the axis for each plot changes so we can resolve the important features of each potential. In all cases $m_F = \frac{1}{2}$ and $g_F = 1$.

quantum system with an oscillating field such as ionization and multiphoton excitation processes. It allows one to find the solutions of a Schrödinger equation with a temporally periodic Hamiltonian by representing it as an infinite matrix [12].

By using a Floquet approach to describe a system containing multiple RF fields we can ensure that higher-order frequency shifts, which are neglected by the piecewise resonance model and other approaches which reply on the RWA, are accounted for.

As in the previous section, we aim to describe the state of an atom confined to a static magnetic field $\mathbf{B}_s(\mathbf{r})$ subjected to a radio-frequency field $\mathbf{B}_{RF}(\omega t)$ with N different frequencies. However, unlike the previous section, we consider linearly polarised fields that can have arbitrary orientation relative to the static field by defining the σ_+ and σ_- components of the RF field as

$$B_+ = \frac{\alpha\cos(\theta) - i\alpha\sin(\theta)}{\sqrt{2}}\,, \tag{11a}$$

$$B_- = \frac{\alpha\cos(\theta) + i\alpha\sin(\theta)}{\sqrt{2}}\,, \tag{11b}$$

and requiring the B_π component to be real. According to eq. (1), the n^{th} RF field can then be written as

$$\mathbf{B}_{RF}(\omega_n t) = \mathbf{B}_n\cos(\omega_n t)\,, \tag{12}$$

where $\mathbf{B}_n$ is the RF field vector and can be decomposed into its components along each Cartesian axis, $\mathbf{B}_n = \alpha_n\cos(\theta_n)\hat{\mathbf{e}}_x + \alpha_n\sin(\theta_n)\hat{\mathbf{e}}_y + B_{\pi_n}\hat{\mathbf{e}}_z$, and controlling the angle θ allows to chose orientation of the RF field. Considering N such fields then leads to the Hamiltonian

$$H(\mathbf{r},t) = \mu_B g_F \mathbf{F}\cdot\left(\mathbf{B}_s(\mathbf{r}) + \sum_{n=1}^{N}\mathbf{B}_n\cos(\omega_n t)\right). \tag{13}$$

We now move to a frame in which the direction of $\mathbf{B}_s(\mathbf{r})$ always points along the z-axis by applying a rotation matrix R to the Hamiltonian. While this can be done for any static field, here we assume that it is of Ioffe-Pitchard form (10). In this case, the rotation matrix R can be written as,

$$R = \begin{pmatrix} \frac{y}{r} & \frac{x}{r} & 0 \\ \frac{B_I x}{B_s r} & \frac{B_I y}{B_s r} & \frac{Gr}{B_s} \\ \frac{Gx}{B_s} & \frac{-Gy}{B_s} & \frac{B_I}{B_s} \end{pmatrix}, \tag{14}$$

and we define $\mathbf{B}'_n(\mathbf{r})$ as the rotated RF field vector such that

$$\mathbf{B}'_n(\mathbf{r}) = \begin{pmatrix} B'_{n_x}(\mathbf{r}) \\ B'_{n_y}(\mathbf{r}) \\ B'_{n_z}(\mathbf{r}) \end{pmatrix} = R\cdot\mathbf{B}_n\,. \tag{15}$$

In the limit $|\mu_B g_F \mathbf{B}'_{n_z}(\mathbf{r})| \ll \hbar\omega_n$ the component that oscillates parallel to the static field, $\mathbf{B}'_{n_z}(\mathbf{r})$, can be neglected and only the orthogonal parts, $\mathbf{B}'_{n_x}(\mathbf{r})$ and $\mathbf{B}'_{n_y}(\mathbf{r})$, contribute to coupling between the atomic levels [7, 19]. The Hamiltonian (13) therefore becomes

$$H(\mathbf{r},t) = \mu_B g_F\left[B_s(\mathbf{r})F_z + \left(\sum_{n=1}^{N}B'_{n_x}(\mathbf{r})\cos(\omega_n t)\right)F_x + \left(\sum_{n=1}^{N}B'_{n_y}(\mathbf{r})\cos(\omega_n t)\right)F_y\right]. \tag{16}$$

A. Single Frequency Floquet Matrix

In this section we will demonstrate the Floquet approach by first explicitly considering the situation where only a single frequency, ω_1, is present. The Hamiltonian is then periodic in time with a period of $\tau = \frac{2\pi}{\omega_1}$

and the Floquet theorem states that the time-dependent Schrödinger equation has a complete set of quasi-periodic solutions, which acquire a phase $\exp(-i\epsilon_n\tau)$ when $t \to t+\tau$. Here the ϵ_n are quasi-eigenenergies and the phase factor defines ϵ_n mod ω_1.

The first step towards finding the quasi-eigenenergies is to remove the time dependence of the Hamiltonian by replacing it with an infinite matrix of the form

$$H_F = \begin{pmatrix} .. & .. & .. & .. & .. & .. & .. \\ .. & H_0+2\hbar\omega_1 & H_{-1} & H_{-2} & H_{-3} & H_{-4} & .. \\ .. & H_1 & H_0+\hbar\omega_1 & H_{-1} & H_{-2} & H_{-3} & .. \\ .. & H_2 & H_1 & H_0 & H_{-1} & H_{-2} & .. \\ .. & H_3 & H_2 & H_1 & H_0-\hbar\omega_1 & H_{-1} & .. \\ .. & H_4 & H_3 & H_2 & H_1 & H_0-2\hbar\omega_1 & .. \\ .. & .. & .. & .. & .. & .. & .. \end{pmatrix}, \tag{17}$$

where the *Floquet blocks* H_n (with n integer) are given by

$$H_n(\mathbf{r}) = \frac{1}{\tau}\int_0^\tau H(\mathbf{r},t)e^{in\omega_1 t}\,dt\,. \tag{18}$$

This procedure can be interpreted as an expansion of the original Hamiltonian in terms of the Fourier components of ω_1. For the Hamiltonian (16) the Floquet blocks can be calculated by using the identity $\frac{1}{\tau}\int_0^\tau e^{i(m-n)\omega t}dt = \delta_{nm}$, where δ is the Kronecker delta [17]. This leads to

$$H_F = \begin{pmatrix} .. & .. & .. & .. & .. & .. & .. \\ .. & kB_s(\mathbf{r})+2\hbar\omega_1 & 0 & 0 & \hbar\Omega_1^*(\mathbf{r}) & 0 & .. \\ .. & 0 & -kB_s(\mathbf{r})+2\hbar\omega_1 & \hbar\Omega_1(\mathbf{r}) & 0 & 0 & .. \\ .. & 0 & \hbar\Omega_1^*(\mathbf{r}) & kB_s(\mathbf{r})+\hbar\omega_1 & 0 & 0 & .. \\ .. & \hbar\Omega_1(\mathbf{r}) & 0 & 0 & -kB_s(\mathbf{r})+\hbar\omega_1 & \hbar\Omega_1(\mathbf{r}) & .. \\ .. & 0 & 0 & 0 & \hbar\Omega_1^*(\mathbf{r}) & kB_s(\mathbf{r}) & .. \\ .. & 0 & 0 & \hbar\Omega_1(\mathbf{r}) & 0 & 0 & .. \\ .. & .. & .. & .. & .. & .. & .. \end{pmatrix} \tag{19}$$

where the Rabi frequency is given by $\Omega_1(\mathbf{r}) = \frac{\mu_B g_F}{4\hbar}\left(B'_{1_x}(\mathbf{r}) + iB'_{1_y}(\mathbf{r})\right)$ and $k = \frac{\mu_B g_F}{2}$.

In order to obtain the eigenvalues and eigenvectors of H_F, it needs to be truncated to a finite size, and a consistent way of doing this is to fix the number of multiples of $\hbar\omega_1$ to include. This corresponds to limiting the order of the photonic processes that can occur, i.e. if we limit the matrix to terms up to $\pm 2\hbar\omega_1$, maximally two photons can be absorbed and emitted. Including higher orders will give a more accurate description, but usually these terms are quickly decreasing in magnitude. To first order, this leads to

$$H_F = \begin{pmatrix} kB_s(\mathbf{r})+\hbar\omega_1 & 0 & 0 & \hbar\Omega_1^*(\mathbf{r}) & 0 & 0 \\ 0 & -kB_s(\mathbf{r})+\hbar\omega_1 & \hbar\Omega_1(\mathbf{r}) & 0 & 0 & 0 \\ 0 & \hbar\Omega_1^*(\mathbf{r}) & kB_s(\mathbf{r}) & 0 & 0 & \hbar\Omega_1^*\mathbf{r} \\ \hbar\Omega_1(\mathbf{r}) & 0 & 0 & -kB_s(\mathbf{r}) & \hbar\Omega_1\mathbf{r} & 0 \\ 0 & 0 & 0 & \hbar\Omega_1^*(\mathbf{r}) & kB_s(\mathbf{r})-\hbar\omega_1 & 0 \\ 0 & 0 & \hbar\Omega_1(\mathbf{r}) & 0 & 0 & -kB_s(\mathbf{r})-\hbar\omega_1 \end{pmatrix}, \tag{20}$$

and diagonalising this matrix gives the quasi-energy spectrum, which in turn allows the adiabatic RF potential to be calculated. This process will be detailed in Sec. VI.

V. MULTI FREQUENCY FLOQUET MATRIX

In this section we will describe the treatment of an RF field containing several radio frequencies and use the model of Many Mode Floquet Theory (MMFT) [13]. We will carry out the calculations explicitly for two different frequencies, ω_1 and ω_2, with the extension to any number being straightforward. The Hamiltonian follows from (16) and is given by

$$H(\mathbf{r},t) = \mu_B g_F \mathbf{F}\cdot(\mathbf{B}_s(\mathbf{r}) + \mathbf{B}_1(\mathbf{r})\cos(\omega_1 t) + \mathbf{B}_2(\mathbf{r})\cos(\omega_2 t))\,, \tag{21}$$

which leads to the basic form for the Floquet matrix

$$H_F^{(2)} = \begin{pmatrix} .. & .. & .. & .. & .. & .. & .. \\ .. & A+2\hbar\omega_r I & P & 0 & 0 & 0 & .. \\ .. & P^T & A+\hbar\omega_r I & P & 0 & 0 & .. \\ .. & 0 & P^T & A & P & 0 & .. \\ .. & 0 & 0 & P^T & A-\omega_r I & P & .. \\ .. & 0 & 0 & 0 & P^T & A-2\hbar\omega_r & .. \\ .. & .. & .. & .. & .. & .. & .. \end{pmatrix}. \tag{22}$$

Here I is the identity matrix and $\omega_r = \omega_1 + \omega_2$ as we want to work in the dressed state picture. The elements of the $H_F^{(2)}$ matrix are matrices themselves and so, $H_F^{(2)}$ can be thought of as a composite matrix of two single frequency Floquet matrices. The ω_1 frequency terms and the $\Omega_1(\mathbf{r})$ Rabi frequency terms are contained in matrix A, which is the same matrix as H_F in the previous section.

The off diagonal elements P contain the Rabi frequency of the second field, $\Omega_2(\mathbf{r}) = \frac{\mu_B g_F}{4\hbar}\left(B'_{2_x}(\mathbf{r}) + iB'_{2_y}(\mathbf{r})\right)$, and are of the form

$$P = \begin{pmatrix} .. & .. & .. & .. & .. & .. & .. \\ .. & 0 & Y & 0 & 0 & 0 & .. \\ .. & 0 & 0 & Y & 0 & 0 & .. \\ .. & 0 & 0 & 0 & Y & 0 & .. \\ .. & 0 & 0 & 0 & 0 & Y & .. \\ .. & 0 & 0 & 0 & 0 & 0 & .. \\ .. & .. & .. & .. & .. & .. & .. \end{pmatrix}, \tag{23}$$

where

$$Y = \begin{pmatrix} 0 & \hbar\Omega_2^*(\mathbf{r}) \\ \hbar\Omega_2(\mathbf{r}) & 0 \end{pmatrix}. \tag{24}$$

By following the method outlined above for the single frequency case, one can then evaluate each of these matrices. However, the explicit form of $H_F^{(2)}$ is too large to reproduce here and we only show a small excerpt of it below to highlight the general structure. The key points of the structure are that the bare trap eigenenergies are given along the diagonal and each Floquet block differs by multiples of both ω_1 and ω_r. The off-diagonal terms correspond to the coupling strengths and contain terms for $\Omega_1(\mathbf{r})$ and $\Omega_2(\mathbf{r})$

$$H_F^{(2)} = \begin{pmatrix} kB_s(\mathbf{r}) + \hbar\omega_1 + \hbar\omega_r & 0 & 0 & .. \\ 0 & -kB_s(\mathbf{r}) + \hbar\omega_1 + \hbar\omega_r & \hbar\Omega_1(\mathbf{r}) & .. \\ 0 & \hbar\Omega_1^*(\mathbf{r}) & kB_s(\mathbf{r}) + \hbar\omega_r & .. \\ \hbar\Omega_1(\mathbf{r}) & 0 & 0 & .. \\ 0 & 0 & 0 & .. \\ 0 & 0 & \hbar\Omega_1(\mathbf{r}) & .. \\ 0 & 0 & 0 & ... \\ 0 & 0 & \hbar\Omega_2(\mathbf{r}) & .. \\ 0 & \hbar\Omega_2^*(\mathbf{r}) & 0 & .. \\ \hbar\Omega_2(\mathbf{r}) & 0 & 0 & .. \\ 0 & 0 & 0 & .. \\ 0 & 0 & \hbar\Omega_2(\mathbf{r}) & .. \\ .. & .. & .. & .. \end{pmatrix} \tag{25}$$

VI. ADIABATIC POTENTIAL GENERATION

In order to produce the adiabatic potential the trapped atoms will follow we need to extract the eigenvalues, $\epsilon^i_{z_n}$, and eigenvectors, $\psi^i_{z_n}$, from our Floquet matrix for every position on the spatial numerical grid, z_n. We do this numerically as producing analytic expressions becomes unfeasible at higher dimensions of the Floquet matrices.

A. 1D Potentials

The quasi-eigenenergies (the eigenvalues of H_F) generated when applying a two frequency, linearly polarised, RF field orthogonal to the movement of an atom in a one-dimensional IP trap are shown in Fig. 3. The spectrum has a periodic structure, which stems from the fact that the quasi eigenenenergies are defined mod ω_1 and mod ω_r, and shows the expected avoided crossings (see Fig. 3(b)). It should be noted that the Rabi frequencies Ω_1 and Ω_2 in this geometry are constant and can be changed independently from each other, which allows to control the size of the avoided crossings associated with each frequency separately.

The potential seen by the atoms can now be found by identifying the the energy eigenvalue in the centre of the trap which is closest to the bare trap eigenenergy, $\epsilon^A_{z_0}$ (normally the smallest positive quasi-eigenvalue), and following its evolution in space. To find the potential at the next numerical grid point z_1, we take the eigenvector $\psi^A_{z_0}$ associated with the eigenvalue at $\epsilon^A_{z_0}$ and calculate $\psi^A_{z_0} \cdot \psi^i_{z_1}$, the dot-product between it and all eigenvectors corresponding to the eigenvalues $\epsilon^i_{z_1}$. The index of the eigenvector which maximises this inner product gives the value of the potential at z_1. Iterating this process allows the construction of the potential along the whole length

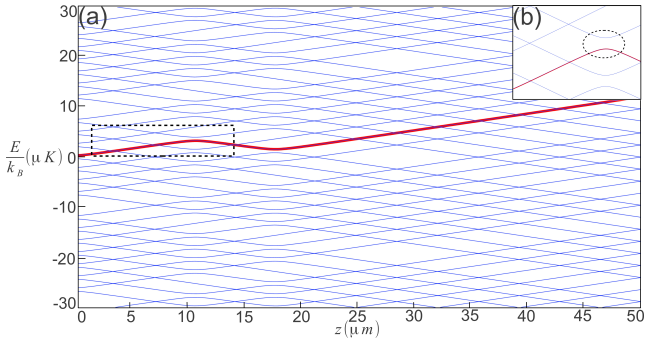

FIG. 3. (a) The spectrum of quasi eigenenergies for an atom trapped in a IP trap irradiated by a two frequency, linearly polarised, RF field. The red (bold) line is the adiabatic RF potential produced from this spectrum. The inset (b) shows a zoom of the highlighted area in (a) where the avoided crossings can be seen (dotted circle). The RF fields have the frequencies $\omega_1 = 2\pi \times 1.5 \times 10^5$Hz and $\omega_2 = 2\pi \times 4 \times 10^5$Hz with Rabi frequencies $\Omega_1 = \Omega_2 = 9.274 \times 10^4$Hz. $m_F = \frac{1}{2}$ and $g_F = 1$ in all cases.

of the trap (see red line in Fig. 3).

Fig. 4 shows the adiabatic RF potentials generated using both the piecewise resonance and Floquet methods for the same parameters as Fig. 2. One can see that the Floquet approach produces the same potential for (a) $\Delta\omega = 1.5 \times 10^5 Hz$ and avoids the discontinuity for (b) $\Delta\omega = 0.4 \times 10^5 Hz$, which is a notable improvement over the piecewise resonant model.

In the extreme case of $\Delta\omega = 0.2 \times 10^5 Hz$ shown in Fig. 4 (c) the Floquet model produces another pair of avoided crossings on either side of the original avoided crossings seen at larger frequency spacing. These extra avoided crossings are the result of the frequencies no longer just coupling the local static field $\mathbf{B}_s(\mathbf{r})$, where they are resonant. Instead, at this very close frequency separation, each frequency is applied to the effective field created by the static field and the other frequency, which leads to a shift in the resonance position and results in the additional avoided crossings. As one can also see from Fig. 4 (c), these avoided crossings are not present in the piecewise resonance model, since the rotating wave approximation eliminates the higher order coupling terms.

From this example it is clear that the Floquet approach to modelling adiabatic RF potentials produces highly accurate results with significant corrections to the piecewise resonance approach. It is therefore well suited to accurately describe multi-frequency RF potentials created using closely spaced frequency. In the next section we will show how the Floquet approach can be extend systems with multiple RF fields where the orientations of the fields are not necessarily perpendicular to the static field.

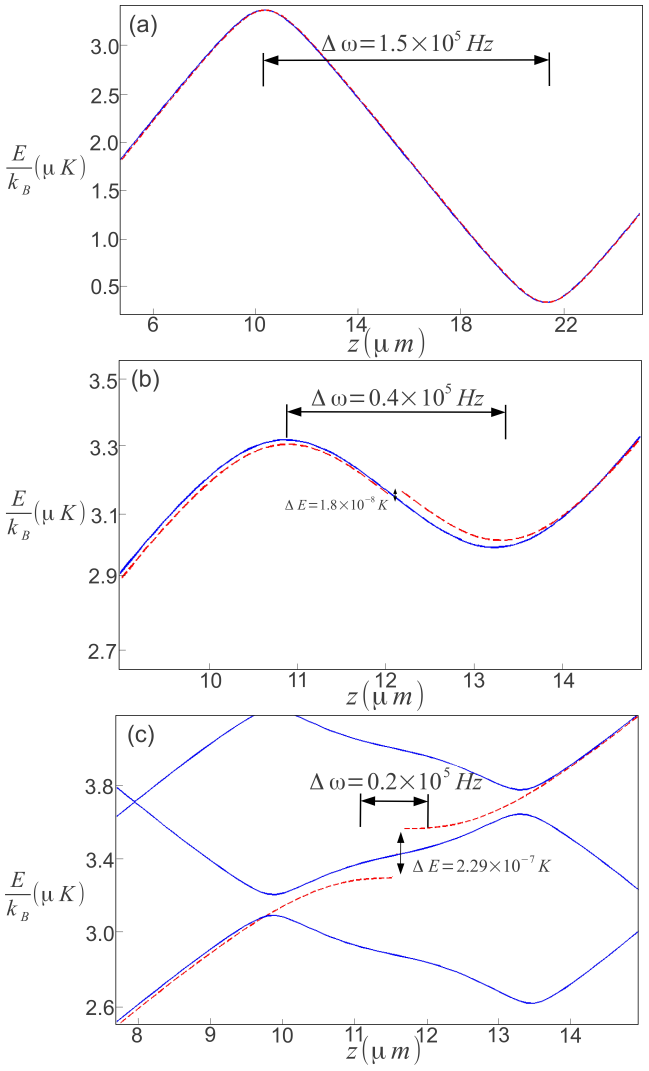

FIG. 4. Comparison between piecewise resonance model (Dashed Red Line) and the Floquet model (Solid Blue Line). All parameters are the same as for Fig 2. See text for discussion.

B. 2D Potentials

The well known flexibility of RF potentials stems from the large number of parameters (number of frequencies, frequency spacing, field strength and orientation) that can be controlled to modify the geometry of the potentials. Additionally these parameters can also be time-dependent, which allows to use the resulting potentials to instigate adiabatic or non-adiabatic dynamics. In the following we consider a multi-dimensional setup and use the Floquet approach to describe some of the features which appear when taking these additional parameters into account.

The main change necessary to extend the model to higher dimensions is to use a multi-dimensional static trapping field $B_s(\mathbf{r})$ which then leads to coupling terms

$\Omega(\mathbf{r})$ of the same, higher dimension. This means that the Floquet matrix contains elements that are multidimensional, but it's basic structure is unchanged from the one-dimensional case. The added dimension however means that the numerical processing power needed to diagonalise the Floquet matrix is significantly higher compared to the one dimensional case.

In the following we will show an example of an interesting potential that can be created using just two frequencies. The numerical approach is similar to the one detailed above, in that we construct the 2D potentials by splitting them into 1D slices and combine them to produce the full 2D potential. To ensure that our minimum rotation method produces 1D slices which are consistent with each other, we use the previously generated 1D slice for each consecutive 1D slice to define an initial quasi-eigenvector and eigenvalue pair.

1. *Two Frequency Potential*

Two-dimensional RF potentials generated using one frequency have already been demonstrated to study rotating BECs in annular geometries [6]. One of the simplest ways to create a more involved structure using two frequencies is shown in Fig. 5 (a) where we consider a 2D IP trap and constant a RF field vector which contains a B_π component only ($\alpha = 0$). One can see that the geometry one can create consists of an outer ring and an inner harmonic potential, which is actually simply the result from the one-dimensional model of Sec. VI rotated around the axis along z=0.

However, by controlling ω_1 and ω_2 one can easily change the depth and radius of the inner harmonic well and the outer ring, as well as the size and height of the barrier between them. Performing such a change in a time-dependent way one can easily engineer a situation where the tunnel coupling between the ring and inner harmonic can be increased or decreased with high accuracy.

Furthermore, having control over the orientation of the RF fields allows one to break the rotational symmetry and create potentials that are no longer isotropic. In Fig. 5 (b) and (c) we show two examples of a 2D potential generated by using constant RF field vectors for (b) $\alpha = 10\mu$T, $\theta = 0$, $B_\pi = 2\mu$T and (c) $\alpha = 10\mu$T, $\theta = \pi$, $B_\pi = 2\mu$T. The resulting potentials display two minima and two maxima on the rings of resonance, which can be understood by considering that the orientation of the $B_{n_x}\hat{\mathbf{e}}_x$ and $B_{n_y}\hat{\mathbf{e}}_y$ components of the RF field with respect to the static field is not constant in space, which leads to the variable coupling. Furthermore, by controlling the angle θ, RF fields pointing in any direction allow the creation of minima and maxima at any position and they can even be rotated in a time dependent fashion.

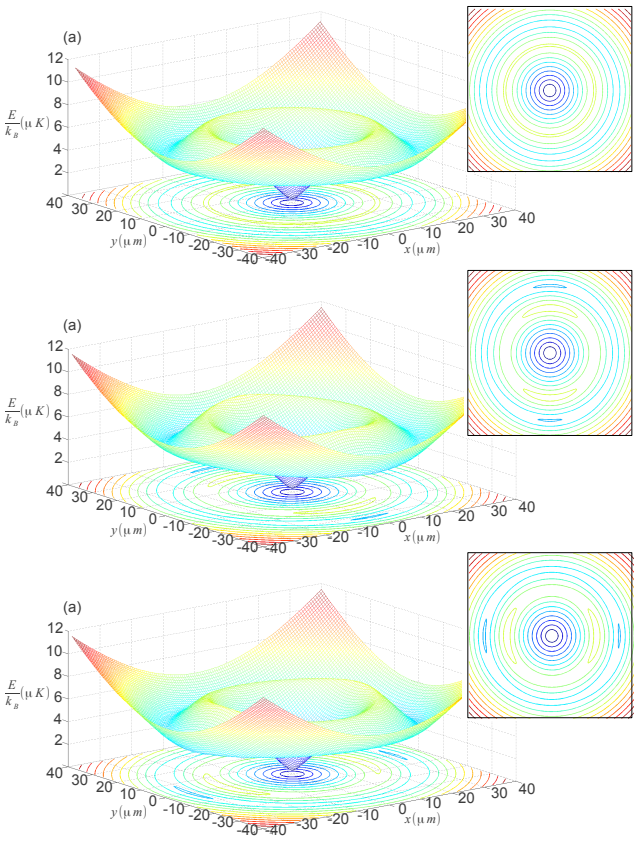

FIG. 5. The adiabatic potential of an atom trapped in an IP trap irradiated by two RF fields with frequencies of $\omega_1 = 3 \times 10^5$Hz and $\omega_2 = 4.5 \times 10^5$Hz for (a) $\alpha = 0$, $B_\pi = 8\mu$T (b) $\alpha = 10\mu$T, $\theta = 0$, $B_\pi = 2\mu$T and (c) $\alpha = 10\mu$T, $\theta = \pi$, $B_\pi = 2\mu$T. In all cases $m_F = \frac{1}{2}$ and $g_F = 1$.

2. *Ring Vortex Solitons*

As an example of how useful the time-dependent control of the tunnelling interaction between the outer ring and the inner harmonic trap can be, we demonstrate in this section how a potential as discussed above can be used to create so-called ring vortex solitions (RVSs) in gaseous Bose-Einstein condensates. These states consist of multiple concentric density-wave rings with a non-zero winding number and they were recently extensively studied by Li *et al.* [20]. To create them in a laboratory, one can consider starting out with a single-frequency RF field in a two-dimensional setting, and creating a condensate carrying a persistent current in the resulting annular potential. Adding the second frequency would allow one to create the central harmonic potential and by adjusting all frequencies and intensities appropriately, the current would start to tunnel into the inner harmonic potential.

To simulate the creation of RVSs in such a way, the potential must allow large tunnelling strength and therefore the model must be able to deal with situations where two frequencies come close. This makes the Floquet approach

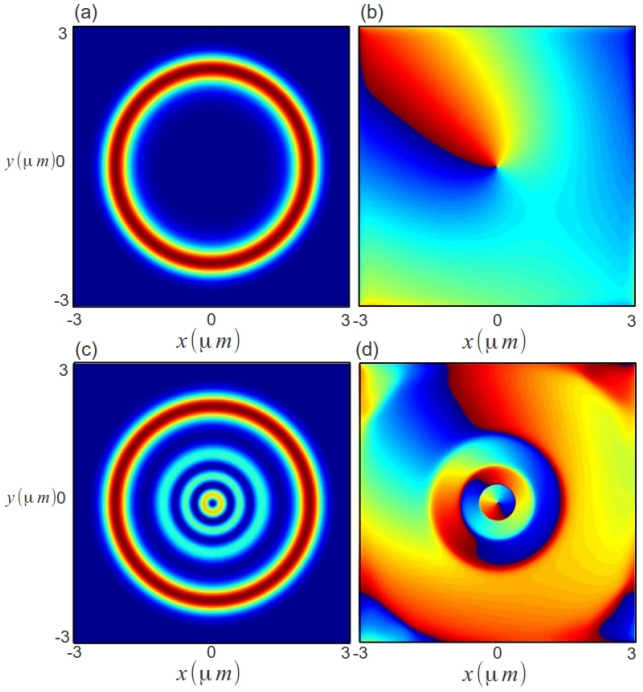

FIG. 6. The creation of a RVS in our adiabatic RF potential. The adiabatic RF potential is created by irradiating an IP trap with two RF fields of frequency $\omega_1 = 27 \times 10^3$Hz and $\omega_2 = 33 \times 10^3$Hz with $B_\pi = 0.4219\mu$T for both fields. (a) Shows the density of the BEC of winding number n=1 initially confined to the outer ring and (b) is its corresponding phase plot. (c) Shows the density of the BEC at $t = 800\mu s$ and (d) is corresponding phase plot.

the most suitable option.

In Fig. 6 we show a simulations of this tunnelling process using a Gross-Pitaevskii model for the condensate and a potential calculated using the Floquet approach outlined above. The density and phase distribution for the BEC initially confined to the outer ring with $n = 1$ can be seen in Figs. 6 (a) and (b), and the density and phase after transfer into the harmonic trap is shown in Figs. 6 (c) and (d). Clearly the resulting state can be identified as a ring vortex soliton.

3. Concentric Ring Potentials

While we have explicitly shown a 2D adiabatic RF potential generated using two frequencies, this can easily be extended to include more frequencies to create potentials that consist of multiple concentric rings. As in the previous example of just two frequencies, control over the frequency spacing would allow one to adjust the tunnelling coupling between the individual rings and can be accurately determined by using a Floquet approach. Such systems are highly desirable as they offer experimentally realistic systems in which one could observe rotational fluxons (Josephson vortices) [21] or study the Kibble-Zurek mechanism in BECs [22].

VII. CONCLUSION

We have shown that using a non-perturbative Floquet approach to calculate radio-frequency potentials for atoms on atom chips leads to good results for multi-frequency situations in one and two dimensions. This approach offers significant corrections to a piecewise-resonant model and can be used to accurately describe situations where two frequencies come close (for example when trying to engineer large tunnel couplings). We have also shown that a Floquet approach can deal with higher dimensions and RF fields of arbitrary field orientation. We have demonstrated the flexibility of the Floquet approach by considering the creation of ring vortex solitons in a 2D adiabatic RF potential which requires that the tunnelling dynamics be determined accurately. Such potentials can be used in a variety of ways, and for example, allow the creation of rotational fluxons and non standard trapping potentials that can connect different topological geometries. This will be the focus of future work.

VIII. ACKNOWLEDGEMENTS

The authors would like to thank Igor Lesanovsky for valuable discussions. This work was supported by the European Science Foundation (ESF) within the framework of the common perspectives for cold atoms, semiconductor polaritons and nanoscience activity and Science Foundation Ireland under project numbers 05/IN/I852 and 10/IN.1/I2979.

[1] R. Folman, P. Krüger, J. Schmiedmayer, J. Denschlag and C. Henkel, Adv. At. Mol. Opt. Phys. **48**, 263 (2002)
[2] J. Fortágh and C. Zimmermann Rev. Mod. Phys. **79**, 235 (2007)
[3] T. Schumm, S. Hofferberth, L.M. Andersson, S. Wildermuth, S. Groth, I. Bar-Joseph, J. Schmiedmayer and P. Krüger, Nature Physics **1**, 57 (2005)
[4] I. Lesanovsky, T. Schumm, S. Hofferberth, L. M. Andersson, P. Krüger, and J. Schmiedmayer. Phys. Rev. A. **73**, 033619 (2006)
[5] T. Fernholz, R. Gerritsma, P. Krüger, R.J.C. Spreeuw, Phys. Rev. A **75**, 063406 (2007)
[6] O. Morizot, Y. Colombe, V. Lorent, H. Perrin, and B. Garraway, Phys. Rev. A **74**, 023617 (2006)

[7] S. Hofferberth, B. Fischer, T. Schumm, J. Schmiedmayer, and I. Lesanovsky, Phys. Rev. A **76**, 013401 (2007)
[8] G. Sinuco-León and B. M. Garraway, New J. Phys. **14** 123008 (2012)
[9] Ph.W. Courteille, B. Deh, J. Fortágh, A. Günther, S. Kraft, C. Marzok, S. Slama, C. Zimmermann, J. Phys. B: At. Mol. Opt. Phys. **39**, 1055 (2006)
[10] F. Bloch and A. J. F. Siegert, Phys. Rev. **57**, 522 (1940).
[11] T .Morgan, B. OSullivan, and Th. Busch, Phys. Rev. A **83**, 053620 (2011)
[12] J. H. Shirley, Phys. Rev. **138**, B979 (1965)
[13] T. S. Ho, S. I. Chu, and J. V. Tietz, Chem. Phys. Lett. **96**, 464471 (1983)
[14] T. S. Ho and S. I. Chu, J. Phys. B: At. Mol. Phys. **17**, 21012128 (1984)
[15] K. Drese and M. Holthaus Eur. Phys. J. D **5**, 119134 (1999)
[16] S. K. Son and S. I. Chu, Phys. Rev. A **77**, 063406 (2008)
[17] S. I. Chu, D. A. Telnovc, Physics Reports, **390**, 1-131 (2004)
[18] C. Cohen-Tannoudji, J. Dupont-Roc, and G. Grynberg, *Atom-Photon Interactions* (Wiley, New York, 1992).
[19] D. T. Pegg, J. Phys. B **6** 241 (1974)
[20] J. Li, D. Wang, Z. Wu, Y. Yu and W. Liu, Phys. Rev. A **86** 023628 (2012)
[21] J. Brand, T. J. Haigh and U. Zülicke, Phys. Rev. A **80** 011602 (2009)
[22] Shih-Wei Su, Shih-Chuan Gou, A. Bradley, O. Fialko and J. Brand, Phys. Rev. L **110** 215302 (2013)

Chapter 6

Stability and Dynamics of Cross Solitons in Harmonically Confined Bose-Einstein Condensates

Non-linear systems allow for a specific class of excitation known as solitons that are characterised by their localisation properties. A soliton is a self-reinforcing wave, i.e. a localised wavepacket that has the property of being able to propagate without dispersion due to a balance between non-linear and dispersive effects. They can also emerge from collisions with other solitons unchanged (except for a phase change). Solitons have been studied extensively in classical fluids [111] and non-linear optics [34] but can also exist in BECs due to the non-linear interaction between the condensed neutral atoms. These are generally referred to as matter wave solitons.

While there has been considerable theoretical work done on the stability of both bright and dark matter wave solitons [40, 112–118] and possible methods for their creation [119–121], it was not until 1999 that the first experimental creation of dark matter wave solitons was simultaneously carried out at the University of Hannover [122] and at NIST in Gaithersburg [123]. Since then there have been a number of other notable experiments including studies of soliton decay mechanisms such as vortex rings [67] and the snake instability [124], the formation of bright solitons [125] and the observation of compound structures comprising solitons and vortex rings [126].

More recent theoretical work on solitons in BECs has focused on solitons and soliton-soliton collisions [127–130], soliton-sound interactions [131], interferometry [36], exact

solutions to the Bogoliubov-de Gennes equations for gray-solitons [41], quantum entanglement [37] and quantum information processing [38].

Until now, the majority of theoretical studies of matter wave solitons have been restricted to one dimension [40, 41, 113, 132–134], as matter wave solitons embedded in 2D and 3D systems are known to suffer from instabilities [66–69]. In the manuscript presented in this Chapter, we extend the discussion of matter wave solitons to truly 2D systems. In this higher dimensionality, we show that one can create arrangements in which several solitons overlay and intersect each other at different angles [68, 135]. These multidimensional solitons exhibit interesting stability and dynamical properties and we analyse these instabilities using direct integration of the Gross-Pitaevskii equation and Bogoliubov-de Gennes theory.

6.1 Stability and Dynamics of Cross Solitons in Harmonically Confined Bose-Einstein Condensates

Manuscript Information

Manuscript Title: Stability and Dynamics of Cross Solitons in Harmonically Confined Bose-Einstein Condensates.

Journal Information: (Preprint) Accepted for publication in Physical Review A on the 15^{th} of November 2013.

Authors: Tadhg Morgan and Thomas Busch.

Pages: 7.

Figures: 7.

Stability and Dynamics of Cross Solitons in Harmonically Confined Bose-Einstein Condensates

Tadhg Morgan*
Quantum Systems Unit, OIST Graduate University, Okinawa, Japan and University College Cork, Cork, Ireland

Thomas Busch
Quantum Systems Unit, OIST Graduate University, Okinawa, Japan

We examine the stability and dynamics of a family of crossed dark solitons in a harmonically confined Bose-Einstein condensate in two dimensions. Working in a regime where the fundamental *snake instability* is suppressed we show the existence of an instability which leads to an interesting collapse and revival of the initial state for the fundamental case of two-crossed solitons. The instability originates from the singular point where the solitons cross and we characterise it by examining the Bogoliubov spectrum. Finally, we extend the treatment to systems of higher symmetry.

I. INTRODUCTION

Bose-Einstein condensates (BECs) of weakly interacting, ultra-cold atomic gases provide highly controllable systems in which one can explore non-linear properties of matter waves [1]. One effect stemming from the balance between non-linear and dispersive effects is the existence of solitary matter waves, or solitons, and these have in recent years been subject to extensive theoretical [2–5] and experimental investigation [6–13]. Solitons can be both, bright and dark, depending on the type of nonlinearity in the system and their primary attribute is propagation without dispersion.

Single solitons and soliton-soliton collisions in weakly interacting condensates in harmonic traps have been thoroughly examined in recent years [5, 14]. However, due to the known instabilities in higher dimensions [15, 16], most work has concentrated on 1D and quasi 1D (ring) geometries [2–5, 17, 18]. At the same time there have been a number of studies of higher dimensional solitons in dipolar condensates [19] and periodic potentials [20, 21], where different stability properties can be found. Here we extend the discussion of solitonic solutions in weakly interacting BECs to multidimensional setups and discuss the appearance of a new type of instability.

The two-dimensional soliton states which we examine in this work are part of a family of so-called dark solitons, which are characterised by a phase profile where each area of distinct phase differs from all other neighbouring areas by a difference of π. Such a profile produces a density dip across each phase jump, which is stable as long as the phase difference is maintained. The configurations which we consider here are comprised of several dark soliton lines in two-dimensions, which overlay and intersect with each other at different angles. In particular, we focus on the arrangements shown in Fig. 1, which represent the most fundamental and symmetric geometries [22, 23].

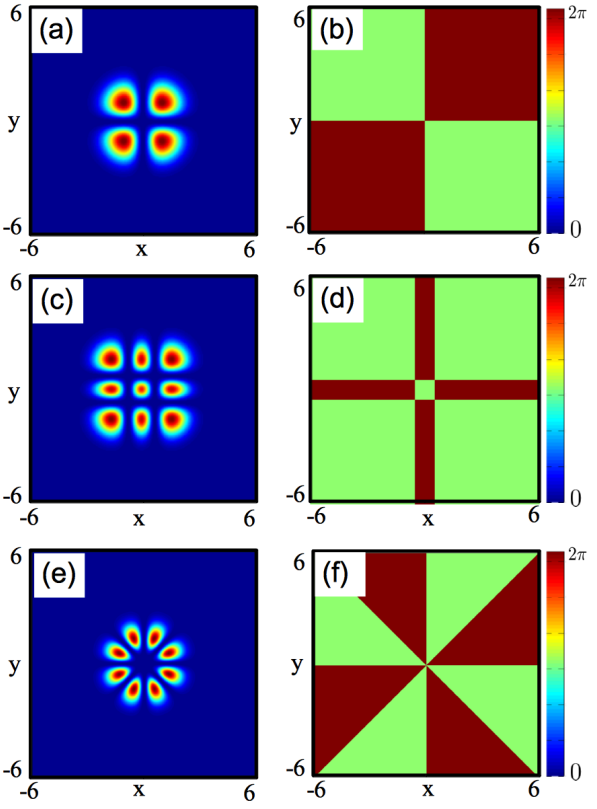

FIG. 1. (Color online) Density (left column) and phase (right column) of the cross soliton [(a) and (b)], the double cross soliton [(c) and (d)] and a star soliton [(e) and (f)]. For all cases the interaction strength $\tilde{g} = 11$ (see eq. 2).

The basic instability of a single dark soliton in two dimensions is to eventually decay into a number of quantized vortices through what is called the *snake instability* [15, 16]. This instability is due to the extension of the soliton into the direction orthogonal to the phase jump

* tmorgan@phys.ucc.ie; http://groups.oist.jp/qsu

and causes it to bend (or *snake*) until the curvature is large enough to lead to a break up into vortex-antivortex pairs. In inhomogeneous systems, however, the snake instability can be suppressed by reducing the width of the trap until the lowest mode of the snake instability is no longer allowed [15].

This is the regime we work in here, as it will allow us to clearly identify and describe possible new instabilities originating from the singular points where the solitons cross (see Figs. 1 (b), (d) and (f)). For this we numerically integrate the Gross-Pitaevskii equation of the system and find an instability corresponding to distinct areas of equal phase connecting across the singular points. Due to the finite size of our system, we also observe a disconnection and almost perfect revival of the initial state, after which the process happens again. To further understand the nature of the instability we make use of the well known Bogoliubov-de Gennes equations to obtain the linear excitation spectrum of the system.

The layout of this paper is as follows. In Section II we outline the nature and creation of the initial states of the solitons shown in Fig. 1. In Section III we numerically time evolve the initial state of the cross soliton to study the dynamics arising from its instability and calculate the Bogoliubov spectrum and the associated eigenfunctions. We show that the Bogoliubov spectrum contains a complex eigenfrequency, which can be connected to the observed dynamical instability. In Section IV we discuss the stability and dynamics of higher order solitons such as the double cross soliton (see Figs. 1 (c) and (d)) and the star soliton (see Figs. 1 (e) and (f)). Finally, in Section V we conclude.

II. INITIAL STATES

In this section we briefly introduce and discuss the initial states of the solitonic systems we wish to study. As we consider inhomogeneous Bose-Einstein condensates of neutral, atomic gases, the condensate wave function, ψ, will be described at any point in time by the time dependent Gross Pitaevskii equation [1]. For numerical tractability we restrict ourselves to a 2D BEC of N atoms of mass m confined to a isotropic harmonic oscillator with trapping frequency ω_T and re-scale our co-ordinates to make them dimensionless via [24]

$$\tilde{t} = \omega_T t, \quad \tilde{x} = \frac{x}{a_0}, \quad \tilde{y} = \frac{y}{a_0}, \tag{1}$$

where $a_0 = \sqrt{\hbar/\omega_T m}$ is the length of the harmonic oscillator ground state and all energies are in units of $\hbar\omega_T$. For ease of notation, we will in the following drop the tilde again. The dimensionless Gross-Pitaevskii equation can then be written as

$$i\frac{\partial\psi}{\partial t} = \left[-\frac{1}{2}\nabla^2 + \frac{1}{2}(x^2+y^2) + \tilde{g}|\psi|^2\right]\psi, \tag{2}$$

where the non-linear interaction strength is given by $\tilde{g} = \frac{4\pi a_s N}{a_0}\sqrt{\frac{\gamma_z}{2\pi}}$. Here a_s is the s-wave scattering length of the atomic species and $\gamma_z = \omega_z/\omega_T$ with ω_z the trapping frequency in the z-direction. To numerically generate the initial states shown in Fig. 1, we evolve an initial wave function in imaginary time using the fft/split operator method [25] under the condition that the desired phase pattern is maintained. The fft/split operator method is also used for real time evolution of the Gross-Pitaevskii equation (2).

The fundamental example of a two-dimensional soliton structure is given by the cross soliton, shown in Figs. 1 (a) and (b). It consists four symmetric lobes separated by a density dip and the phases between neighbouring lobes are arranged to differ by the required factor of π. While the angle between the solitons can in principle take any value, we concentrate here on the perpendicular setting as it allows to clearly identify the nature of the instability. Note that the dark soliton lines in this state are in the radial direction and therefore are not subject to the well known oscillation instability [3].

A higher order state of the family of crossed solitons is the so-called double cross soliton, which is shown in Figs. 1 (c) and (d). It consists of two pairs of perpendicularly crossed density dips, leading to nine separated density areas with appropriate phases between them. Due to the presence of the external, harmonic potential, not all areas are equally populated and the dark soliton lines are no longer radial lines. This leads to small oscillations of the solitons in the potential [3], but we find them to not influence the newly forming instabilities.

The final system we will investigate is the so-called star soliton, shown in Figs. 1 (e) and (f). It is an extension of the cross soliton described above, but instead of four lobes the condensate is split into eight with appropriate phases between them. All soliton lines connect in the centre, which means that they are radial lines and no extra oscillations are to be expected. Again, while in principle all angles between the intersecting solitons can be considered, we focus here on the symmetric setting where all angles are chosen to be $\pi/4$.

III. DYNAMICAL INSTABILITY AND BOGOLIUBOV ANALYSIS

In order to determine the stability of the states described above, we will carry out a fully two-dimensional integration of the Gross-Pitaevskii equation and examine the eigenspectrum obtained from a Bogoliubov analysis. For the latter one has to solve the Bogoliubov-de Gennes equations [1, 26]

$$L\mathbf{u_j} - \tilde{g}\psi^2\mathbf{v_j} = \omega_j\mathbf{u_j}, \tag{3}$$

$$L\mathbf{v_j} - \tilde{g}\psi^{*2}\mathbf{u_j} = -\omega_j\mathbf{v_j}, \tag{4}$$

where $L = -\frac{1}{2}\nabla^2 + \frac{1}{2}(x^2+y^2) + 2\tilde{g}|\psi|^2 - \mu$ and μ is the chemical potential. Examining the spectrum of eigenfrequencies ω_j and corresponding eigenvectors $\mathbf{u_j}$ and $\mathbf{v_j}$

provides information about the stability properties of the state ψ. A small positive ω_j with a positive norm $n_j = \int(|\mathbf{u_j}|^2 - |\mathbf{v_j}|^2)d\mathbf{r}$ corresponds to small oscillations about the state and indicates stability. A mode with negative ω_j with a positive norm n_j is called an anomalous mode and indicates that the initial state will continuously transform into a lower energy state. Finally, complex and purely imaginary eigenfrequencies ω_j with $n_j = 0$ indicate the presence of a dynamical instability [1].

To be able to identify potential instabilities cleanly, we must work in a regime where the snake instability for line-solitons is suppressed. As shown by Brand *et al.* [15], this can be achieved by reducing the transverse width of the soliton and for a condensate consisting of a large number of repulsively interacting atoms the condensate width can be determined in the Thomas-Fermi approximation as [24]

$$R = \frac{1}{\sqrt{2}}\left(\frac{15\tilde{g}\gamma_z}{4\pi}\right)^{1/5}. \tag{5}$$

One can see that the size of the condensate, and hence the transversal width of an embedded soliton, can be reduced by decreasing the non-linear interaction constant, $\tilde{g}$.

Calculating the Bogoliubov spectrum for a single dark soliton we find that it becomes completely real and positive once $\tilde{g} \leq 19$, which corresponds to the point beyond which the snake instability is suppressed [27]. We have confirmed this by direct numerical time evolution and also checked that around this value the decay into vortices is absent in the multi-soliton systems shown in Fig. 1. To ensure that we are far from the snake instability regime for all cases we therefore choose $\tilde{g} = 11$ in all numerical simulations.

Although the snake instability is suppressed, real time evolution of the cross soliton in this regime reveals the existence of another dynamic instability. After a period where the initial state is stationary, a series of repeating collapse and revival events sets in, which are driven by one of the pairs of lobes of equal phase connecting and collapsing to the centre of the trap with the other pair of lobes surrounding it (see Figs. 2 (a) and (b)) [28]. The density and phase of the fully collapsed cross soliton are shown in Figs. 2 (c) and (d) and the state has the form of two curved line-solitons. In fact, by examining the low density areas it can be seen that the two outer parts connect to form a highly non-symmetric ring soliton. This collapsed state is relatively short lived and evolves, due to the finite size of the system, back into the initial state seen before the collapse [29]. If we further evolve the state in time we see another collapse and revival but this time the other pair of lobes connects and collapses to the centre.

In Fig. 3 we show the imaginary frequencies of the Bogoliubov spectrum for the cross soliton as a function of the interaction strength $\tilde{g}$. These correspond to the instability identified above (blue circle line) and the snake instability (red diamond line). One can see that the snake instability only sets in once the repulsive interaction has

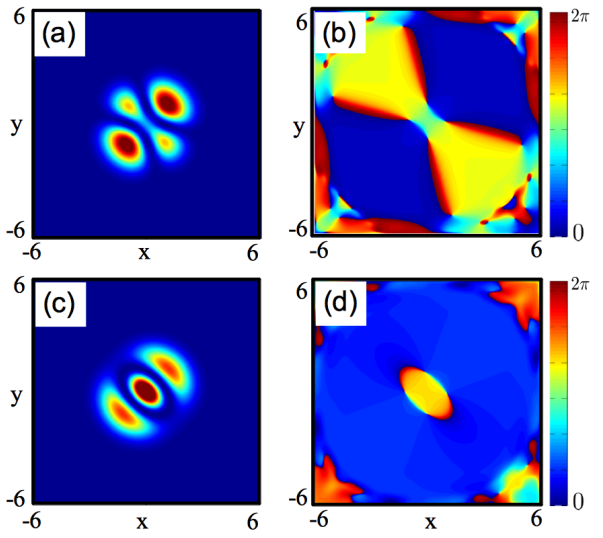

FIG. 2. (Color online) The densities (left column) and phases (right column) of the cross soliton as it begins to collapse at $t = 128$ (upper row) and after full collapse at $t = 138$ (lower row).

increased the size of the condensate beyond the critical width and a finite region exists in which the instability discussed above sets in before the snake instability. Note that the line corresponding to the snake instability is actually doubly degenerate, corresponding to an instability in each of the crossed solitons.

For reference we have also included the sole imaginary Bogoliubov mode of the single dark soliton, which corresponds to the snake instability (green dashed line). The shift between this line and the one for the crossed soliton indicates that the crossing point leads to a certain increase in stability against *snaking*.

At the value of $\tilde{g} = 11$ considered in our numerical simulations, only one imaginary frequency mode with $\omega_1 = 0.2673i$ exists, the density and phase of which are shown in Figs. 4 (a) and (b) respectively. To show that this mode is indeed the mode responsible for the instability we observe, we examine the density and phase of a state that is created by linearly combining the initial cross soliton state, ψ, and the unstable mode,

$$\Psi = \psi + \alpha\mathbf{u_j}. \tag{6}$$

As the form of the Bogoliubov modes is given by $\mathbf{u_j}e^{-i\omega_j t}$, over a short period of time, an imaginary frequency will cause the amplitude of the mode to increase exponentially before, due to interference from waves reflected on the boundary of our system, it reduces again. By using a non-zero α parameter in (6), we can therefore approximate the influence of the mode on the initial state and, as can be seen in Figs. 4 (c) and (d), for $\alpha = 25$, the density and phase of Ψ is very close to the one obtained numerically at $t = 132$ (Figs. 2 (a) and (b)).

The time for the onset of the instability can be predicted from the eigenfrequency of the unstable mode as

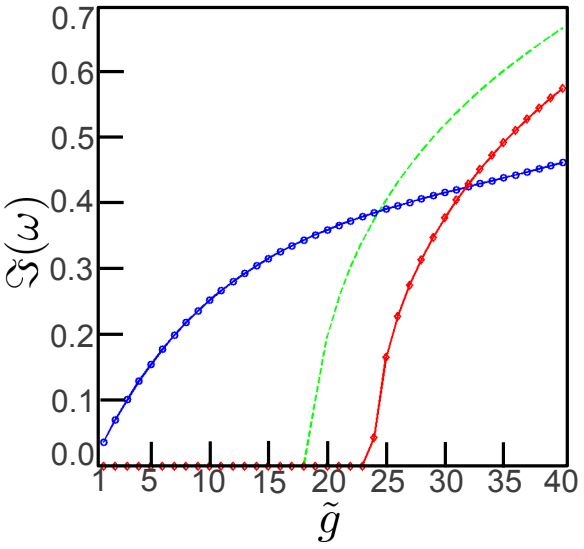

FIG. 3. (Color online) The imaginary modes of the Bogoliubov spectrum of the cross soliton. The red diamond line corresponds to the snake instability and the blue circle line to the new cross soliton instability. The green dashed line is included for reference and corresponds to the snake mode of a single dark line soliton.

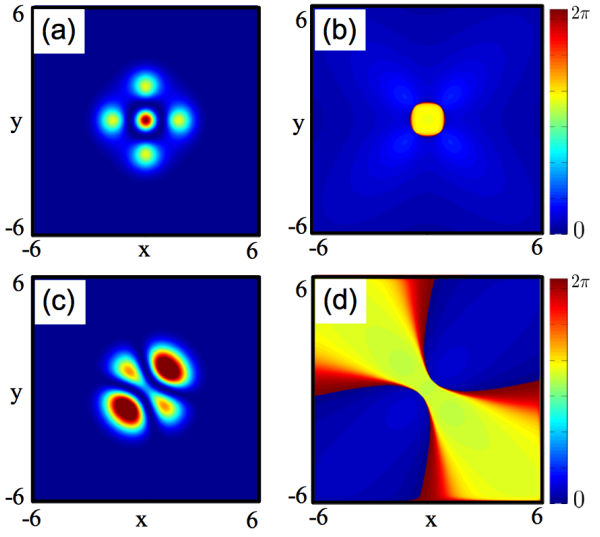

FIG. 4. (Color online) The density (a) and phase (b) of the unstable Bogoliubov mode with eigenfrequency $\omega_1 = 0.2673$ for the cross soliton. The density (c) and phase (d) of Ψ for $\alpha = 25$. Note that the color scale of (a) and (b) are not equal.

$T \approx \frac{2\pi}{\Im(\omega_1)}$. This can be seen in Fig. 5 (a) where we show the density at the centre of the trap (the point of the singularity) as a function of time. Initially the system performs small oscillations which, around the predicted time of the instability T, turn into an exponential increase in the density. This ultimately leads to the complete collapse of the cross soliton.

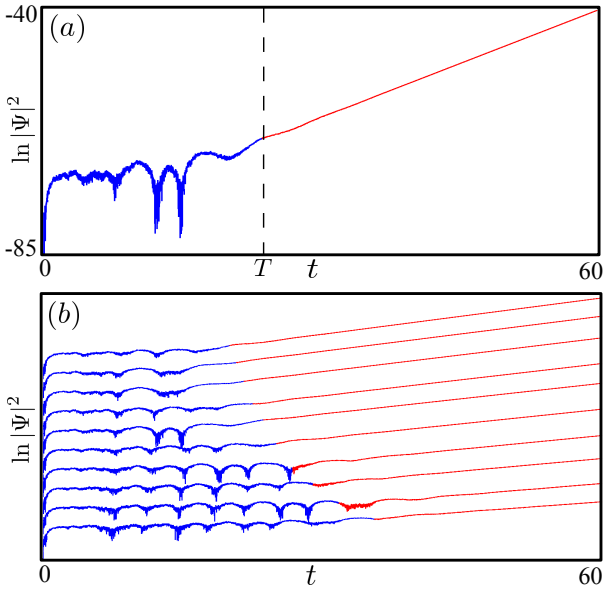

FIG. 5. (Color online) (a) Density at the trap centre as a function of time for a condensate with $\tilde{g} = 11$. The time for the onset of the instability predicted by the Bogoliubov analysis is indicated by the dashed line and by the change of colour of the graph from blue to red. (b) Same as in (a) for different non-linearities ranging from $\tilde{g} = 6$ to $\tilde{g} = 15$ in steps of 1 from below. The individual curves are offset for clarity.

In Fig. 5 (b) we repeat this analysis over a wide range of values for $\tilde{g}$. The time for the instability, T, is represented by the change of the line colour from blue to red and one can see that the effect is consistent over the whole range. Furthermore, this data also shows that increasing the strength of interaction leads to an earlier onset of instability in the system.

IV. HIGHER ORDER SYMMETRY

In this section we will extend the discussion of stability presented for the cross soliton to the higher order structures shown in Fig. 1. However, before we can do so, we briefly need to address the stability of our numerical approach. One cause for concern for the validity of the presented Bogoliubov analysis is the influence of the square numerical grid used in the generation of the initial state. Any dark soliton line not on axis with the grid can only be approximated and will suffer from spatial aliasing, which in turn leads to a numerical effect on the instability time-scales. We have investigated this issue thoroughly and found that this problem is absent for a dark soliton line at an angle of $\pi/4$ to the numerical grid, by comparing the results obtained for a cross soliton at an angle of $\pi/4$ with the ones obtained for the structure lying along the grid axes.

Therefore, the first higher order soliton we study is the double cross soliton whose composite dark soliton lines are on axis with the numerical grid. The second soliton structure is the star soliton which contains two dark soliton lines that are on axis with the numerical grid and two at an angle of $\pi/4$ to the numerical grid.

A. Double Cross Soliton

For the double cross soliton, the density and phase are shown in Fig 1 (c) and (d). Time evolution of this state reveals that it is, much like the cross soliton, quasi-stable for a certain period before the instability sets in. In this period of quasi-stability however, the soliton lines are subject to the oscillation instability in inhomogeneous potentials [3], but the amplitudes gained are only small and do not affect the onset of the collapse instability.

The nature of the collapse of the double cross soliton is similar to that of the cross soliton, but of a higher order. Like the cross soliton, lobes of equal phase connect and fall into the centre as shown in Figs. 6 (a) and (b). The density and phase distribution of the fully collapsed double cross soliton is shown in Figs. 6 (c) and (d) and one can see, that the result of the collapse leads to four curved soliton lines. When taking the low density regions into account and by looking at the phase distribution, one can see that these lines connect to form two concentric, non-symmetric ring solitons. Unlike the cross soliton however, we do not observe a revival of the initial state on the timescales we are able to simulate.

The Bogoliubov analysis of the double cross soliton reveals one unstable mode with a purely imaginary eigenfrequency $\omega_1 = 0.2591i$, which is responsible for the observed instability. As for the single soliton, we use the linear combination of the initial state and the unstable mode (see eqn. (6)), to confirm that this mode corresponds to the observed instability and Figs. 6 (e) and (f) show a good agreement with the state of the double cross soliton at $t = 119$ for $\alpha = 30$.

B. Star Soliton

Unlike the two previous cases, the Bogoliubov spectrum for the star soliton (see Figs. 1 (e) and (f)), reveals two unstable modes with frequencies $\omega_1 = 0.1211i$ and $\omega_2 = 0.0886i$. However, due to the increased complexity of the star soliton, producing accurate modes using the Bogoliubov-de Gennes equations is difficult. Therefore, to obtain information about the properties of these instabilities we study the time evolution of the star soliton by numerically integrating the Gross-Pitaevskii equation.

As indicated by its larger frequency, the influence of the first mode is seen before the second mode during time evolution, and corresponds to oscillations originating from lobes of equal phase connecting in the centre (see Figs. 7 (a) and (b)). This is mode is similar to the

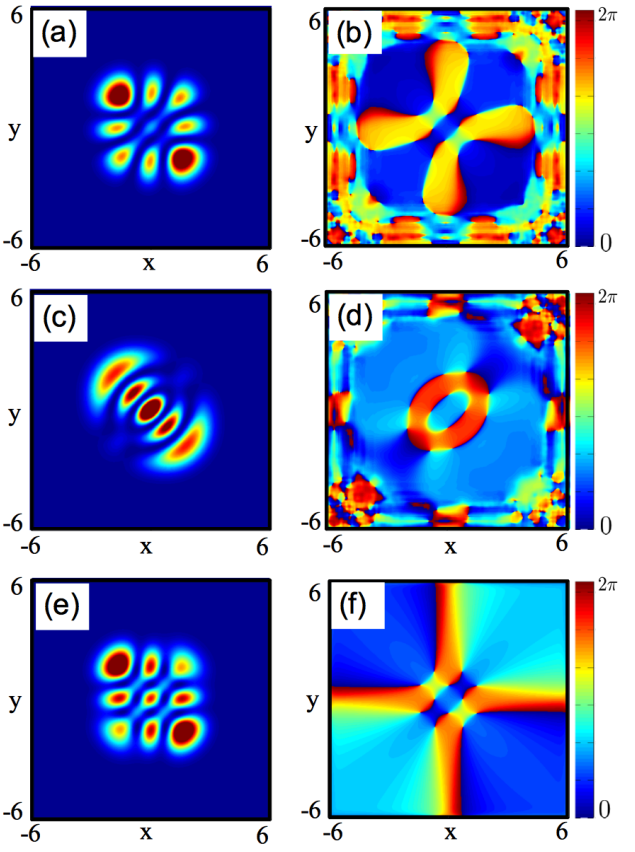

FIG. 6. (Color online) The density (a) and phase (b) of the double cross soliton in the early stages of the collapse at $t = 119$ and for the fully collapsed state at $t = 132$, (c) and (d) respectively. Panels (e) and (f) show the density and phase of Ψ for $\alpha = 30$.

one found for the cross soliton and generalises it to the higher order of the star soliton. In contrast, however, we find that the amplitude here is small and the overall star pattern is maintained. Therefore, it is possible for the second unstable mode to set in at a later time and after the first instability has undergone a couple of oscillatory cycles.

The second mode induces a transformation into a very structured state that is reminiscent of the double cross soliton, as can be seen in Figs. 7 (c) and (d). This state, in turn, then decays in the same manner as discussed in Subsec. IV A. The fact that this decay channel is found here, suggests that even higher order structures might possess even more complicated and interesting stability properties.

V. CONCLUSION

We have presented an investigation into a new family of two-dimensional solitons consisting of overlapping dark soliton lines. In the regime where the snake instability

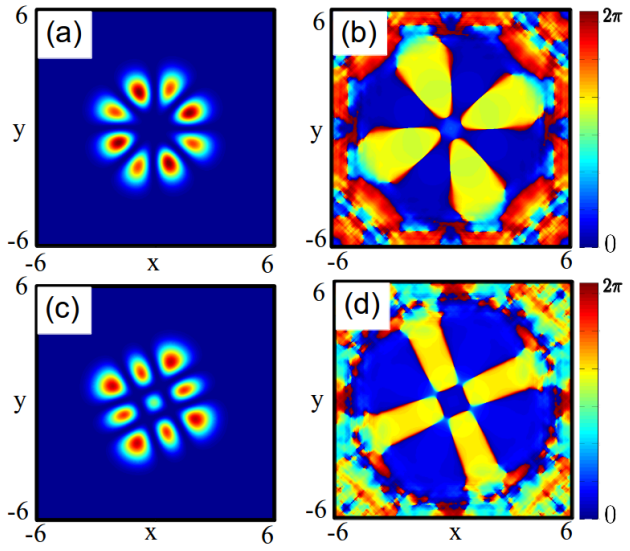

FIG. 7. (Color online) The density (left colum) and phase (right column) of the star soliton during time evolution. Panels (a) and (b) correspond to $t = 15$, where the first unstable mode of frequency $\omega_1 = 0.1211i$ causes slight oscillations in the density distribution between the lobes of the star soliton. Panels (c) and (d) correspond to $t = 35$, where the influence of the second unstable mode of frequency $\omega_2 = 0.0886i$ can be seen.

is absent a new instability stemming from the singular point where the solitons cross can be identified and we have discussed its behaviour for three fundamental structures: the cross soliton, the double cross soliton and the star soliton. For the cross soliton this instability (combined with the small system size) led to a collapse and revival of the initial state where distinct areas of identical phase connect and disconnect. The associated Bogoliubov analysis showed that this mode was well described by linear perturbation theory and that the time of its onset depends on the strength of the system's non-linearity. The higher order double cross soliton and the star soliton were shown to also decay in a structured manner.

Our work shows that even though these two-dimensional soliton structures are inherently unstable, their decay process is highly structured and interesting. An obvious extension of the presented work is the generalisation to three dimensional systems, where instabilities of a different nature could appear.

VI. ACKNOWLEDGMENTS

The authors would like to thank Jim McCann for informative discussions on the above work.

[1] L. Pitaevskii and S. Stringari, *Bose-Einstein Condensation*, Oxford University Press (2003).
[2] W. Reinhardt and C. Clark J. Phys. B: At. Mol. Opt. Phys. **30**, L785 (1997).
[3] Th. Busch and J. R. Anglin, Phys. Rev. Lett. **84**, 2298 (2000).
[4] S. L. Cornish, N. G. Parker, A. M. Martin, T. E. Judd, R. G. Scott, T. M. Fromhold and C. S. Adams, Physica D **238**, 1299 (2009).
[5] A. D. Martin, C. S. Adams, and S. A. Gardiner, Phys. Rev. Lett. **98**, 020402 (2007).
[6] K. E. Strecker, G. B. Partridge, A. G. Truscott and R. G. Hulet, Nature **417**, 150 (2002).
[7] C. Becker, S. Stellmer, P. Soltan-Panahi, S. Dörscher, M. Baumert, E. Richter, J. Kronjäger, K. Bongs and K. Sengstock, Nature Physics **4**, 496 (2008).
[8] Tarik Yefsah, Ariel T. Sommer, Mark J. H. Ku, Lawrence W. Cheuk, Wenjie Ji, Waseem S. Bakr & Martin W. Zwierlein, Nature **499**, 426 (2013).
[9] B. P. Anderson, P. C. Haljan, C. A. Regal, D. L. Feder, L. A. Collins, C. W. Clark, and E. A. Cornell, Phys. Rev. Lett. **86**, 2926 (2001).
[10] L. Khaykovich, F. Schreck, G. Ferrari, T. Bourdel, J. Cubizolles, L. D. Carr, Y. Castin, C. Salomon, Science **296** 1290 (2002) .
[11] S. Burger, K. Bongs, S. Dettmer, W. Ertmer, K. Sengstock, A. Sanpera, G. V. Shlyapnikov, and M. Lewenstein, Phys. Rev. Lett. **83**, 5198 (1999).
[12] J. Denschlag, J. E. Simsarian, D. L. Feder, C. W. Clark, L. A. Collins, J. Cubizolles, L. Deng, E. W. Hagley, K. Helmerson, W. P. Reinhardt, S. L. Rolston, B. I. Schneider, W. D. Phillips, Science **287**, 97 (2000).
[13] Z. Dutton, M. Budde, C. Slowe and L. V. Hau, Science **293**, 663 (2001).
[14] S. Stellmer, C. Becker, P. Soltan-Panahi, E. M. Richter, S. Dörscher, M. Baumert, J. Kronjäger, K. Bongs, and K. Sengstock, Phys. Rev. Lett. **101**, 120406 (2008).
[15] J. Brand and W. P. Reinhardt, Phys. Rev. A **65**, 043612 (2002).
[16] L. A. Toikka and K. A. Suominen, Phys. Rev. A **87**, 043601 (2013).
[17] Z. X. Liang, Z. D. Zhang, and W. M. Liu, Phys. Rev. Lett. **94**, 050402 (2005).
[18] P. B. Walczak and J. R. Anglin, Phys. Rev. A **84**, 013611 (2011).
[19] P. Pedri and L. Santos, Phys. Rev. Lett. **95**, 200404 (2005).
[20] B. B. Baizakov, B. A. Malomed and M. Salerno, Europhys. Lett. **63** 642 (2003).
[21] B. B. Baizakov, B. A. Malomed, and M. Salerno, Phys. Rev. A 70, 053613 (2004).
[22] Xuesong Zhao, Lu Li, and Zhiyong Xu, Phys. Rev. A **79**, 043827 (2009).
[23] D. L. Feder, M. S. Pindzola, L. A. Collins, B. I. Schneider, and C. W. Clark, Phys. Rev. A **62**, 053606 (2000).
[24] W. Bao, D. Jaksch and P. Markowich, J. Comp. Phys **187**, 318 (2003).

[25] J. A. Fleck, J. R. Morris and M. D. Feit, App. Phys. **10** 129 (1976).
[26] N. N. Bogoliubov, J. Phys. (USSR) **11**, 23 (1947)
[27] The Bogoliubov-de Gennes equations are numerically solved by transforming them to an eigenvalue problem using a finite-difference method. The eigenvalues and eigenfunctions are then found through standard Lanczos diagonalisation.
[28] Even though all potential unstable modes are initially unpopulated, the numerical noise introduced during time evolution of the initial state is sufficient to populate them.
[29] N. G. Parker, N. P. Proukakis, M. Leadbeater, and C. S. Adams, Phys. Rev. Lett. **90**, 220401 (2003).

Chapter 7

Conclusions and Outlook

In this thesis I have focused on two topics: the first dealt with developing realistic techniques for engineering quantum states of ultracold atoms and the second described the stability properties of a novel family of solitonic states. For the first topic, I presented a comprehensive theoretical study of atom chip and adiabatic radio frequency potentials and the second topic consisted of numerical integration of the Gross Pitaevskii equation and an associated linear stability analysis using Bogoliubov theory. For completeness, I briefly summarise the major results of each Chapter in the following and outline ideas and directions for future work.

7.0.1 Coherent Tunnelling by Adiabatic Passage on Atomchips

In the first manuscript presented in Chapter 3, I presented 2D simulations of the coherent tunnelling by adiabatic passage (CTAP) process between the magnetic waveguides created with a counter-intuitive arrangement of wires on an atom chip. This was first done with a model using idealised potentials (tanh shape), which closely approximated the waveguides created by the current carrying wires of the atom chip. This allowed me to determine the parameters which play an important role in the fidelity of the population transferred.

I then simulated the CTAP process for the transport of a single atom using realistic magnetic waveguides above current-carrying wires on atom chips, and showed that by reducing the current of the central wire, an approximate resonance between the waveguides can be achieved such that it allows for the successful implementation of CTAP. The results of these 2D simulations clearly showed that adiabatic transfer in the counter-intuitive setup can lead to high fidelity and can be clearly distinguished from direct tunnelling in the intuitive setup through the absence of Rabi oscillations.

In the second manuscript presented in Chapter 3, I extended this work to performing 3D simulations of the CTAP process in an atom chip system. These simulations took the complete spatial dynamics in all three dimensions into account, which is a numerically intensive task. By using GPU computing, I was able to show that the performance of numerically simulating the time-dependent Schrödinger equation can be significantly increased, making the problem numerically tractable on a standard desktop computer.

While the three-dimensional setup involves solving a number of other problems as well, I was again able to show that by reducing the current of the central wire a regime can be found in which the high fidelity populations transfer due to CTAP is observable in an experimentally realistic system. I also found that a range of values for the current of the middle wire exists, for which both counter-intuitive and intuitive arrangement of the wires produce high fidelity transfer to the target state. Considering that the energy of the middle waveguide is shifted through the process, I conjectured that this was due to Stark chirped rapid adiabatic passage (SCRAP).

Investigating the possibility to use the SCRAP process in an atom chip system to achieve population transfer would be a fruitful road for a future investigation. I expect that the transversal eigenspectrum of the atom chip system would contain a rich structure which, for example, shows pairs of avoided crossings that allow the SCRAP process to occur.

7.0.2 Coherent Adiabatic Transport of Atoms in Radio-Frequency Traps

In Chapter 4 I discussed the possibility for observing the CTAP process in an adiabatic rf potential. To create the three spatially distinct trapped states required for CTAP, it was necessary to use six separate frequencies. The position of the traps could then be controlled by simply changing the pairs of frequencies associated with each trap. I found that neighbouring rf trapping potentials can be overlapped without significantly altering their geometry. This is important, as one of the requirements of CTAP is that a resonance between the trapped states exists at any point during the process. As such, my simulations showed that a complete transfer between the left and right traps, by utilizing the dark state, produces the expected high fidelity with an absence of unwanted Rabi oscillations.

As the geometry of each trap is given by the frequency separation of the two frequencies closest to resonance, one can control the depth of each trap independently from its position. I showed that this ability allowed the use of the CTAP technique to transport a cloud of weakly interacting atoms. By dynamically detuning the traps over the duration of the process, I showed that one can compensate for the added interaction energy so as to keep the traps in approximate resonance.

Interesting future work on this topic would be to use the ability to independently detune the traps to implement other adiabatic techniques such as SCRAP, which could be done with either two or three rf traps. Extending the CTAP technique to higher dimensions would also be of interest, where the orientation or polarisation of the rf field could possibly be used to control the tunnel coupling rather than the frequency separation.

7.0.3 Floquet Theory for Modelling Adiabatic Radio Frequency Potentials

In Chapter 5 I focused on using Floquet theory to model adiabatic radio frequency potentials. This was motivated by the shortcomings of the piecewise resonance model used in Chapter 4 which, while appropriate for the system I was studying, breaks down when the frequencies are very close and for large Rabi frequencies. By mapping the time-dependent Hamiltonian to an infinite Floquet matrix, I showed that a Floquet approach can produce adiabatic rf potentials even in the extreme situations mentioned above.

I then extended this Flouqet approach to consider 2D rf fields of arbitrary field orientation. I showed that by controlling the orientation of the rf field, the geometry of the potentials could be modified and that this could be done in a time-dependent fashion. As a demonstration of the utility of such 2D potentials, I simulated a 2D potential in which an outer ring is separated from an inner harmonic well. I showed that ring vortex solitons can be created in such a potential and that they therefore offer an experimentally realistic system to study complex rotational states.

There are many possibilities for future research in this area. One can easily envision many different types of 2D adiabatic rf potentials that could be created. In particular, studying anisotropic static fields with rf coupling would be of interest. There are also many future applications of Floquet theory, such as describing rotational states of BECs confined to rf traps as a super position of Floquet states. The simulations of tunnelling in such systems could also be extended by including spin-orbital coupling.

7.0.4 Stability and Dynamics of Cross Solitons in a Harmonically Confined Bose-Einstein Condensate

In Chapter 6 I studied the dynamical and stability properties of a novel family of solitonic states. These structures consisted of several dark solitons which overlayed and intersected each other at different angles.

I showed that these multi-dimensional solitons exhibited interesting dynamical instabilities, where a periodic collapse and revival of the initial state was seen during time evolution. Using the Bogoliubov-de Gennes equations, I showed that these instabilities could not be attributed to the normal snake instability associated with dark soliton decay in 2D. Through an investigation of the Bogoliubov spectrum, I showed which multi-dimensional unstable modes were responsible for the observed dynamic instability for each of the solitonic states and also predicted the time scales in which they occur.

For future research into these solitonic states, I suggest that moving to higher dimensions would reveal many more interesting properties. It is known that in three dimensions, dark solitons decay into ring vortices. With this decay mechanism, the observed dynamic instability could be significantly different in 3D. I also suggest moving to anisotropic harmonic traps, where one could allow the snake instability to only exist along one transversal degree of freedom. In this regime, it would be interesting to see what effect the snake instability would have on the instabilities we have observed.

Bibliography

[1] M. H. Anderson, J. R. Ensher, M. R. Matthews, C. E. Wieman, E. A. Cornell, Science, **269**, 198 (1995)

[2] J. F. Sherson, C. Weitenberg, M. Endres, M. Cheneau, I. Bloch and S. Kuhr, Nature **467**, 68 (2010)

[3] C. Weitenberg, M. Endres, J. F. Sherson, M. Cheneau, P. Schauß, T. Fukuhara, I. Bloch and S. Kuhr, Nature **471**, 319 (2011)

[4] W. S. Bakr, J. I. Gillen, A. Peng, S. Fölling and M. Greiner, Nature **462**, 74 (2009)

[5] D. Leibfried, R. Blatt, C. Monroe, D. Wineland, Rev. Mod. Phys. **75**, 281 (2003)

[6] G. Moore, Electronics Magazine, Volume 38, Number 8 (1965)

[7] Yasuhisa Naitoh, Masayo Horikawa and Tetsuo Shimizu, MRS Proceedings Volume 997 (2007)

[8] M. Fuechsle, J. A. Miwa, S. Mahapatra, H. Ryu, S. Lee, O. Warschkow, L. C. L. Hollenberg, G. Klimeck and M. Y. Simmons, Nature Nanotechnology **7**, 242 (2012)

[9] J. I. Cirac and P. Zoller, Phys. Rev. Lett. **74**, 4091 (1995)

[10] ID Quantique, http://www.idquantique.com/

[11] MagiQ Technologies Inc, http://www.magiqtech.com/

[12] D-Wave Systems Inc, http://www.dwavesys.com/

[13] C. Guerlin, J. Bernu, S. Deléglise, C. Sayrin, S. Gleyzes, S. Kuhr, M. Brune, J. Raimond and S. Haroche, Nature **448**, 889 (2007)

[14] S. Gleyzes, S. Kuhr, C. Guerlin, J. Bernu, S. Deléglise, U. B. Hoff, M. Brune, J. Raimond1 and S. Haroche, Nature **446**, 297 (2007)

[15] C. Monroe, D. M. Meekhof, B. E. King, W. M. Itano, and D. J. Wineland, Phys. Rev. Lett. **75**, 4714 (1995)

[16] W. Demtröder, *Laser Spectroscopy: Basic Concepts and Instrumentation*, Springer (2003)

[17] M.A. Nielsen, and I.L. Chuang, *Quantum Computation and Quantum Information*, Cambridge University Press,Cambridge (2000).

[18] J. Mompart, K. Eckert, W. Ertmer, G. Birkl, and M. Lewenstein Phys. Rev. Lett. **90**, 147901 (2003)

[19] C. Weitenberg, S. Kuhr, K. Mølmer, and J. F. Sherson, Phys. Rev. A **84**, 032322 (2011)

[20] K. Eckert, M. Lewenstein, R. Corbalán, G. Birkl, W. Ertmer, and J. Mompart, Phys. Rev. A **70**, 023606 (2004)

[21] K. Eckert, J. Mompart, R. Corbalán, M. Lewenstein, and G. Birkl, Opt. Comm. **264**, 264 (2006)

[22] K. Bergmann, H. Theuer, and B.W. Shore, Rev. Mod. Phys. **70**, 1003 (1998)

[23] A. D. Greentree, J. H. Cole, A. R. Hamilton, and L. C. L. Hollenberg, Phys. Rev. B **70**, 235317 (2004)

[24] M. Rab, J. H. Cole, N. G. Parker, A. D. Greentree, L. C. L. Hollenberg, and A.M. Martin, Phys. Rev. A **77**, 061602 (2008)

[25] R. Folman, P. Krüger, J. Schmiedmayer, J. Denschlag and C. Henkel, Advances In Atomic, Molecular, and Optical Physics **48**, 263 (2002)

[26] I. Lesanovsky, T. Schumm, S. Hofferberth, L. M. Andersson, P. Krüger, and J. Schmiedmayer, Phys. Rev. A. **73**, 033619 (2006)

[27] O. Zobay, B.M. Garraway, Phys. Rev. Lett. **86**, 1195 (2001)

[28] T. Schumm, S. Hofferberth, L. M. Andersson, S. Wildermuth, S. Groth, I. Bar-Joseph, J. Schmiedmayer and P. Krüger, Nature Physics **1**, 57 (2005)

[29] Ph. W. Courteille, B. Deh, J. Fortágh, A. Günther, S. Kraft, C. Marzok, S. Slama, C. Zimmermann, J. Phys. B: At. Mol. Opt. Phys. **39**, 1055 (2006)

[30] G. Floquet, Annales de l'École Normale Supérieure **12** 47 (1883)

[31] J. H. Shirley, Phys. Rev. **138**, B979 (1965)

[32] J. Li, D. Wang, Z. Wu, Y. Yu and W. Liu, Phys. Rev. A **86** 023628 (2012)

[33] M. Remoissenet, *Waves Called Solitons: Concepts and Experiments*, Springer Verlag, Berlin (1996)

[34] Y. S. Kivshar, G. Agrawal ,*Optical Solitons: From Fibers to Photonic Crystals*, Academic Press (2003)

[35] Ryogo Hirota, Phys. Rev. Lett. **27** 1192 (1971)

[36] J. L. Helm, T. P. Billam, and S. A. Gardiner, Phys. Rev. A **85**, 053621 (2012)

[37] B. Gertjerenken, T. P. Billam, C. L. Blackley, C. Ruth Le Sueur, L. Khaykovich, S. L. Cornish, and C. Weiss, Phys. Rev. Lett. **111**, 100406 (2013)

[38] V. Ahufinger, A Mebrahtu, R. Corbalán and A. Sanpera, N. J. Phys. **9** 4 (2007)

[39] S. Stellmer, C. Becker, P. Soltan-Panahi, E. M. Richter, S. Dörscher, M. Baumert, J. Kronjäger, K. Bongs, and K. Sengstock, Phys. Rev. Lett. **101**, 120406 (2008)

[40] Th. Busch and J. R. Anglin, Phys. Rev. Lett. **84**, 2298 (2000)

[41] P. B. Walczak and J. R. Anglin, Phys. Rev. A **84**, 013611 (2011)

[42] C. J. Pethick and H. Smith, *Bose-Einstein Condensation in Dilute Gases*, Cambridge (2002)

[43] L. Pitaevskii and S. Stringari, *Bose-Einstein Condensation*, Clarendon Press, Oxford (2003)

[44] C. J. Foot, Atomic Physics, Oxford University Press (2011)

[45] H. Feshbach, Ann. Phys. (N.Y.) **5**, 357 (1958)

[46] H. Feshbach, Ann. Phys. (N.Y.) **19**, 287 (1962)

[47] S. Earnshaw, Trans. Camb. Phil. Soc. **7**, 97 (1842)

[48] J. Denschlag, D. Cassettari, and J. Schmiedmayer, Phys. Rev. Lett. **82**, 2014 (1999)

[49] A. Kasper, S. Schneider, Ch. vom Hagen , M. Bartenstein, B. Engeser, T. Schumm, I. Bar-Joseph, R. Folman, L. Feenstra, and J. Schmiedmayer, J. Opt. B: Quantum Semiclass. Opt. **5** S143 (2003)

[50] M. Trinker et al, Appl. Phys. Lett. **92**, 254102 (2008)

[51] P. Quinto-Su, M. Tscherneck, M. Holmes, and N. Bigelow, Opt. Express, **12**, 5098 (2004)

[52] J. Schmiedmayer, R. Folman and T. Calarco, J. Mod. Optics, **49**, 1375 (2002)

[53] DW. Wang, M. D. Lukin, and E. Demler, Phys. Rev. Lett. **92**, 076802 (2004)

[54] M. F. Riedel, P. Böhi, Y. Li, T. W. Hänsch, A. Sinatra and P. Treutlein, Nature **464**, 1170 (2010)

[55] E. Majorana, Il Nuovo Cimento **9**, 43 (1932)

[56] D. E. Pritchard, Phys. Rev. Lett. **51** 1336 (1983)

[57] M. Fewell, B. W. Shore, and K. Bergmann, Aust. J. Phys. **50**, 281 (1997)

[58] D. T. Pegg, J. Phys. B **6** 241 (1974)

[59] S. Hofferberth, B. Fischer, T. Schumm, J. Schmiedmayer, and I. Lesanovsky, Phys. Rev. A **76**, 013401 (2007)

[60] F. Bloch and A. Siegert, Phys. Rev. **57**, 522 (1940)

[61] S. I. Chu, D. A. Telnovc, Physics Reports, **390**, 1-131 (2004)

[62] T. S. Ho, S. I. Chu, and J. V. Tietz, Chem. Phys. Lett. **96**, 464471 (1983)

[63] S. A. Morgan, R. J. Ballagh, and K. Burnett, Phys. Rev. A **55**, 4338 (1997)

[64] T. Hong, Y. Z. Wang, and Y. S. Huo, Phys. Rev. A **58**, 3128 (1998)

[65] V. E. Zakharov and A. B. Shabat, Sov. Phys. JETP **34**, 62 (1972)

[66] J. Brand and W. Reinhardt, Phys. Rev. A **65**, 043612 (2002)

[67] B. P. Anderson, P. C. Haljan, C. A. Regal, D. L. Feder, L. A. Collins, C. W. Clark and E. A. Cornell, Phys. Rev. Lett. **86**, 2926 (2001)

[68] D. L. Feder, M. S. Pindzola, L. A. Collins, B. I. Schneider, and C. W. Clark, Phys. Rev. A **62**, 053606 (2000)

[69] L. A. Toikka and K. A. Suominen, Phys. Rev. A **87**, 043601 (2013)

[70] Yu. Loiko, V. Ahufinger, R. Corbalán, G. Birkl, and J. Mompart, Phys. Rev. A **83**, 033629 (2011)

[71] S. Longhi, G. Della Valle, M. Ornigotti, and P. Laporta, Phys. Rev. B **76** 201101R (2007)

[72] A. Benseny, S. Fernández-Vidal, J. Bagudà, R. Corbalán, A. Picón, L. Roso, G. Birkl, and J. Mompart, Phys. Rev. A **82**, 013604 (2010)

[73] D. Petrosyan and P. Lambropoulos, Optics Communications **264**, 419 (2006)

[74] B. Chen, W. Fan, and Y. Xu, Phys. Rev. A **83**, 014301 (2011)

[75] J. Huneke, G. Platero, and S. Kohler, Phys. Rev. Lett. **110**, 036802 (2013)

[76] J. P. Kestner and S. Das Sarma, Phys. Rev. A **84**, 012315 (2011)

[77] R. Rahman, S. H. Park, J. H. Cole, A. D. Greentree, R. P. Muller, G. Klimeck, and L. C. L. Hollenberg, Phys. Rev. B **80**, 035302 (2009)

[78] R. Menchon-Enrich, A. Llobera, V. J. Cadarso, J. Mompart, and V. Ahufinger, Light: Science & Applications **2**, e90 (2013)

[79] A. Negretti, A. Benseny, J. Mompart, T. Calarco, Quantum Information Processing **12**, 1439 (2013)

[80] M. Rab, A. L. C. Hayward, J. H. Cole, A. D. Greentree, and A. M. Martin, Phys. Rev. A **86**, 063605 (2012)

[81] N. H. Dekker, C. S. Lee, V. Lorent, J. H. Thywissen, S. P. Smith, M. Drndić, R. M. Westervelt, and M. Prentiss, Phys. Rev. Lett. **84** 1124 (2000)

[82] P. Böhi, M. F. Riedel, J. Hoffrogge, J. Reichel, T. W. Hänsch and P. Treutlein, Nature Physics **5**, 592 (2009)

[83] J. Petrovic, I. Herrera, P. Lombardi, F. Schäfer and F. S. Cataliotti, New J. Phys. **15** 043002 (2013)

[84] T. Langen, R. Geiger, M. Kuhnert, B. Rauer and J. Schmiedmayer, Nature Physics 2739 (Advanced Online Publication) (2013)

[85] M. A. Cirone, A. Negretti, T. Calarco, P. Krüger, J. Schmiedmayer, Eur. Phys. J. D **35**, 165 (2005)

[86] E. Charron, M. A. Cirone, A. Negretti, J. Schmiedmayer and T. Calarco, Phys. Rev. A **74**, 012308 (2006)

[87] P. Treutlein, T. Hänsch, J. Reichel, A. Negretti, M. A. Cirone, and T. Calarco, Phys. Rev. A **74**, 022312 (2006)

[88] J. B. Trebbia, C. L. Garrido Alzar, R. Cornelussen, C. I. Westbrook, and I. Bouchoule Phys. Rev. Lett. **98**, 263201 (2007)

[89] S. Hofferberth, I. Lesanovsky, B. Fischer, J. Verdu and J. Schmiedmayer, Nature Physics **2**, 710 (2006)

[90] M. Kohnen, M. Succo, P. G. Petrov, R. A. Nyman, M. Trupke and E. Hinds, Nature Photonics **5** 35 (2011)

[91] C. Ó Broin, L. A. A. Nikolopoulos, Computer Physics Communications **183**, 2071 (2012)

[92] H. Bauke, C. H. Keitel, Comp. Phys. Comm. **10**, 4655 (2011)

[93] R. M. Caplan, Computer Physics Communications **184** 1250 (2013)

[94] A. Frezzotti, G. P. Ghiroldi, L. Gibelli, Computer Physics Communications **182**,2445 (2011)

[95] T. Kramer, V. Krueckl, E. Heller and R. Parrott, Phys. Rev. B **81**, 205306 (2010)

[96] M. Weigel, Computer Physics Communications **182** 1833 (2011)

[97] E. Muskat, D. Dubbers and O. Schärpf, Phys. Rev. Lett. **58**, 2047 (1987)

[98] O. Morizot, C. L. Garrido Alzar, P-E. Pottie, V. Lorent and H. Perrin, J. Phys. B **40** 4013 (2007)

[99] W. H. Heathcote, E. Nugent, B. T. Sheard and C. J. Foot, New J. Phys. **10** 043012 (2008)

[100] T. Fernholz, R. Gerritsma, P. Krüger, R. J. C. Spreeuw, Phys. Rev. A **75**, 063406 (2007)

[101] P. Zhang and L. You, Phys. Rev. A **76**, 033615 (2007)

[102] M. Shotter, D. Trypogeorgos and C. Foot, Phys. Rev. A **78**, 051602(R) (2008)

[103] O. Morizot, Y. Colombe, V. Lorent, H. Perrin, and B. Garraway, Phys. Rev. A **74**, 023617 (2006)

[104] J. Brand, T. J. Haigh and U. Zülicke, Phys. Rev. A **80** 011602 (2009)

[105] SW. Su, SC, Gou, A. Bradley, O. Fialko and J. Brand, Phys. Rev. Lett. **110** 215302 (2013)

[106] T. S. Ho and S. I. Chu, J. Phys. B: At. Mol. Phys. **17**, 21012128 (1984)

[107] A. Schmidt and S. Vega, J. Chem. Phys. **96**, 2655 (1992)

[108] T. O. Levante, M. Baldus, B. H. Meier, and R. R. Ernst, Molecular Physics **86** 1195 (1995)

[109] K. Drese and M. Holthaus, Eur. Phys. J. D **5**, 119134 (1999)

[110] S. K. Son and S. I. Chu, Phys. Rev. A **77**, 063406 (2008)

[111] R. H. J. Grimshaw, *Solitary waves in fluids*, WIT Press, (2007)

[112] W. Zhang, D. F. Walls, and B. C. Sanders, Phys. Rev. Lett. 72, **60** (1994)

[113] W. P. Reinhardt and C. W. Clark, J. Phys. B **30**, L785 (1997)

[114] A. D. Jackson, G. M. Kavoulakis, and C. J. Pethick, Phys. Rev. A **58**, 2417 (1998)

[115] A. E. Muryshev, H. B. van Linden van den Heuvell, and G. V. Shlyapnikov, Phys. Rev. A **60**, R2665 (1999)

[116] P. O. Fedichev, A. E. Muryshev, and G. V. Shlyapnikov, Phys. Rev. A **60**, 3220 (1999)

[117] V. M. Pérez-García, H. Michinel, H. Herrero, Phys. Rev. A **57**, 3837 (1998)

[118] L. D. Carr, M. A. Leung, W. P. Reinhardt, J. Phys. B **33**, 3983 (2000)

[119] R. Dum, J. I. Cirac, M. Lewenstein, and P. Zoller, Phys. Rev. Lett. **80**, 2972 (1998)

[120] T. F. Scott, R. J. Ballagh, and K. Burnett, J. Phys. B **31**, L329 (1998)

[121] Ł. Dobrek, M. Gajda, M. Lewenstein, K. Sengstock, G. Birkl, and W. Ertmer, Phys. Rev. A **60**, R3381 (1999)

[122] S. Burger, K. Bongs, S. Dettmer, W. Ertmer, K. Sengstock, A. Sanpera, G. V. Shlyapnikov, M. Lewenstein, Phys. Rev. Lett. **83**, 5198 (1999)

[123] J. Denschlag, J. E. Simsarian, D. L. Feder, C. W. Clark, L. A. Collins, J. Cubizolles, L. Deng, E. W. Hagley, K. Helmerson, W. P. Reinhardt, S. L. Rolston, B. I. Schneider, W. D. Phillips, Science **287**, 97 (2000)

[124] Z. Dutton, M. Budde, C. Slowe, L. V. Hau, Science **293**, 663 (2001)

[125] L. Khaykovich, F. Schreck, G. Ferrari, T. Bourdel, J. Cubizolles, L. D. Carr, Y. Castin, C. Salomon, Science **296** 1290 (2002)

[126] N. S. Ginsberg, J. Brand, L. V. Hau, Phys. Rev. Lett. **94**, 040403 (2005)

[127] A. D. Martin, C. S. Adams, and S. A. Gardiner, Phys. Rev. Lett. **98**, 020402 (2007)

[128] T. P. Billam, S. L. Cornish, and S. A. Gardiner, Phys. Rev. A **83**, 041602(R) (2011)

[129] A. D. Martin, C. S. Adams, and S. A. Gardiner, Phys. Rev. A **77**, 013620 (2008)

[130] N. G. Parker, A. M. Martin, S. L. Cornish and C. S. Adams, J. Phys. B: At. Mol. Opt. Phys. **41** 045303 (2008)

[131] N. G. Parker, N. P. Proukakis, M. Leadbeater, and C. S. Adams, Phys. Rev. Lett. **90**, 220401 (2003)

[132] S. L. Cornish, N. G. Parker, A. M. Martin, T. E. Judd, R. G. Scott, T. M. Fromhold and C. S. Adams, Physica D **238**, 1299 (2009)

[133] A. D. Martin, C. S. Adams, and S. A. Gardiner, Phys. Rev. Lett. **98**, 020402 (2007)

[134] Z. X. Liang, Z. D. Zhang, and W. M. Liu, Phys. Rev. Lett. **94**, 050402 (2005)

[135] X. Zhao, L. Li, and Z. Xu, Phys. Rev. A **79**, 043827 (2009)